Stress corrosion cracking of AISI 321 SS welds in solar thermal power plants: Failure analysis and appropriate surface engineering measures

Dissertation submitted in partial fulfillment of the requirements for the degree of

Doctor of Philosophy

in

Materials Engineering

by

Kamal Mankari

(10ETMM12)

Under the guidance of

Dr. Swati Ghosh Acharyya



SCHOOL OF ENGINEERING SCIENCES AND TECHNOLOGY UNIVERSITY OF HYDERABAD HYDERABAD-500046 INDIA

DECEMBER 2017

DECLARATION

I, hereby declare that the thesis entitled "Stress corrosion cracking of AISI 321 SS welds in solar thermal power plant: Failure analysis and appropriate surface engineering measures" submitted to University of Hyderabad for the award of Doctor of Philosophy in Materials Engineering is original and was carried out by me during my tenure as a Ph.D. scholar under the supervision of **Dr. Swati Ghosh Acharyya**. I also declare that this thesis has not been submitted previously in part or in full to this University or any other University or Institution for the award of any degree or diploma.

KAMAL MANKARI

Reg. no.: 10ETMM12

School of Engineering Sciences and Technology,

University of Hyderabad.



CERTIFICATE

This is to certify that the thesis work entitled "Stress corrosion cracking of AISI 321 SS welds in solar thermal power plant: Failure analysis and appropriate surface engineering measures", submitted by Kamal Mankari bearing Reg. No. 10ETMM12 in partial fulfillment of the requirements for the award of the degree of Doctor of Philosophy in Materials Engineering is a bonafide record of the work that has been carried out by him under my supervision. This thesis has not been submitted previously in part or in full to this or any other University or Institution for the award of any degree or diploma.

Thesis Supervisor

Dr. Swati Ghosh Acharyya

Assistant professor,

School of Engineering Sciences and Technology,

University of Hyderabad

Approved by

Prof. M. Ghanashyam Krishna

Dean,

School of Engineering Sciences and Technology,

University of Hyderabad



CERTIFICATE

This is to certify that the thesis entitled "Stress corrosion cracking of AISI 321 SS welds in solar thermal power plant: Failure analysis and appropriate surface engineering measures" submitted by KAMAL MANKARI bearing registration number 10ETMM12 in partial fulfillment of the requirements for award of Doctor of Philosophy (in Materials Engineering) in the School of Engineering Sciences and Technology (SEST) is a bonafide work carried out by him under my supervision and guidance.

This thesis is free from plagiarism and has not been submitted previously in part or in full to this or any other University or Institution for the award of any degree or diploma.

Part of this thesis has been published in

- 1. Kamal Mankari et al., Applied Surface Science. (doi.org/10.1016/j.apsusc.2017.07.223)
- **2. Kamal Mankari** *et al.*, *Engineering Failure Analysis*. (doi.org/10.1016/j.engfailanal.2017.12.020) and was exempted from doing coursework (recommended by Doctoral Committee) on the basis of the following courses passed during his M.Tech. (Int. M.Tech./Ph.D) and the M.Tech. Degree was awarded:

Course	Title of the Course	Credits	Pass/Fail
No.			
MT401	Phase Transformations and Thermodynamics	4	Pass
MT402	Concepts of Materials Science	4	Pass
MT403	Metal Forming: Science and Technology	4	Pass
MT404	Characterization of Materials	4	Pass
MT405	Seminar	2	Pass
MT406	Design and Selection of Engineering Materials	4	Pass
MT 407	Materials Processing and Characterization Laboratory	4	Pass
MT451	Materials & Technologies for Energy Systems	4	Pass
MT452	Diffusion and Kinetics	4	Pass
MT453	Modeling and Simulation	4	Pass
MT454	Powder Metallurgy and Ceramics	4	Pass
MT455	Surface Engineering & Advanced Nanofabrication	4	Pass
W11433	Technologies	_	1 455
MT456	Polymer Science and Technology	2	Pass
MT457	Laboratory	4	Pass
MT458	Seminar	2	Pass
MT680	Dissertation	18	Pass
MT601	Research Methodology	4	Pass

Supervisor Dean of School

ACKNOWLEDGEMENTS

First and foremost, I express my deep gratitude and respect to my research supervisor *Dr. Swati Ghosh Acharyya*, Assistant Professor, for her keen interest, valuable guidance, strong motivation and constant encouragement during my research work.

My doctoral review committee members *Dr. Raj Kishora Dash* and *Dr. Pradip Paik* have also been helpful and supportive over the last several years. I am also thankful to the Dean of School of Engineering Sciences and Technology, *Prof. M. Ghanashyam Krishna* and all other faculties in the department for providing me the facilities and the guidance to carry out my research work.

I would also like to thank the technicians and non-teaching staff of SEST *Mr. Mallesh, Mr. Venkatramana, Mrs. Kranthi kumari, Mrs. Malathi*, and TEM technician *Mr. Durga Prasad and Mr. Pankaj*.

I would like to thank, *Rahul Roxy*, *Koushi Kumar.U*, *Abhijit*, *pandu*, *Johny Varghese*, and *Pardhu Yella* helped me with innumerable tricky problem sets and became some of my best friends.

Lastly, I thank my family for always supporting me and my interest. I would probably be somewhere else if it were not for my family's invincible and contagious optimism

KAMAL MANKARI

CONTENTS

List of tables	vii
List of figures	viii
List of publications/Conferences	xii
Abbreviations	xiii
Abstract	
Chapter 1:	
1.0 Introduction	1
1.1 Background	1
1.2 Objectives of the thesis	2
1.3 Thesis Layout	2
CHAPTER 2:	
2.0 Literature review	3
2.1 Austenitic stainless steels	3
2.1.1 Un-stabilized grades of austenitic stainless steels like AISI 304	
and AISI 316	4
2.1.2 Stabilized grades like AISI 321 and AISI 347	5
2.2 Corrosion issues in austenitic stainless steels	6
2.2.1 Pitting corrosion	6
2.2.1.1 Effect of microstructure	7
2.2.1.2 Inclusions	7
2.2.1.3 Alloy composition	8
2.2.2 Intergranular corrosion (IGC)	9
2.2.3 Hot cracking	9
2.2.4 Stress corrosion cracking (SCC)	11
2.2.4.1 Tensile stresses	11
2.2.4.2 Environment factors	11
2.2.4.3 Susceptible material	15

2.3 Stress corrosion cracking (SCC) of austenitic stainless steel welds	17
2.4 Welding of austenitic stainless steels	18
2.4.1 LASER welding	19
2.4.2 LASER hybrid arc welding	19
2.4.3 Metal inert gas welding (MIG)	20
2.4.4 Spot Welding (SW)	21
2.5 Residual stresses generated by different techniques	22
2.5.1 Residual stress generated during welding	23
2.5.2 Residual stress generated during surface finishing	23
2.6 Solar thermal power plants	23
2.6.1 Solar thermal collectors for solar industrial process heat applications	24
2.6.2 Solar collector	25
2.6.2.1 Non-concentrating type solar collectors	25
2.6.2.1.1 Flat plate solar water collector	26
2.6.2.1.2 Evacuated tube collector	27
2.6.2.1.3 Direct flow evacuated tube collector	28
2.6.2.1.4 Heat pipe evacuated tube collector	28
2.6.2.2 Concentrating type solar collectors	29
2.6.2.2.1 Compound parabolic concentrator (CPC)	30
2.6.2.2.2 Central receiver (or) solar tower	30
2.6.2.2.3 Parabolic dish collector	31
2.6.2.2.4 Parabolic trough collector	31
2.6.3 Various materials used in solar thermal power plants	32
2.6.4 Thermionic fluids properties and various degradation mechanisms	33
Chapter 3:	
3.0 Experimental	35
3.1 Materials 2.2 Non-destructive evaluation	35
3.2 Non-destructive evaluation	36
3.3 Heat treatment	37
3.4 Surface roughness measurement	37

3.5 Microstructural characterization	37
3.5.1 Sample preparation	37
3.5.2 Microstructural evaluation	38
3.5.2.1 Optical Microscope (OM)	38
3.5.2.2 Field Emission Scanning Electron Microscope (FESEM)	38
3.6 X-ray diffraction	38
3.7 Buffing operation	38
3.8 Mechanical characterization techniques	39
3.8.1 Hardness testing	39
3.8.2 Residual stress measurement	39
3.8.3 Determination of stress corrosion cracking (SCC) susceptibility	41
CHAPTER 4:	
4.0 RESULTS AND DISCUSSION	42
4.1 PART-I: Failure analysis of AISI 321 stainless steel (SS) welded tubes	
in solar-Thermal power plant	42
4.1.1 Visual Examination and Dye Penetrant Testing	42
4.1.2 X-ray diffraction of all welded AISI 321 SS tubes	45
4.1.3 Micro hardness measurement	46
4.1.4 Microstructural characterization of the base material of AISI 321	
stainless steel	47
4.1.5 Microstructural characterization of the differently welded region	
of AISI 321SS Tubes	52
4.1.5.1 Spot welded region of the tubes	52
4.1.5.2 Laser beam welded tubes	54
4.1.5.3 Metal inert gas welded tubes	56
Summary of Part I	58
4.2 PART-II: Stress corrosion cracking (SCC) susceptibility of LBW,	
MIG and base metal of AISI 321 SS tubes	59
4.2.1 Micro structural characterization of LBW specimen after MgCl ₂ test	
for 5 h, 10 h, and 72h	59

4.2.1.1 Micrographs of LBW region after MgCl ₂ test for 5 h	59
4.2.1.2 LBW specimen after MgCl ₂ test for 10 h	59
4.2.1.3 LBW specimen after MgCl ₂ test for 72h	60
4.2.2 Microstructural characterization of base material after MgCl ₂ test	
for 5h, 10h, and 72h	61
4.2.2.1 Base material micrograph after MgCl ₂ test for 5h	61
4.2.2.2 Base material micrograph after MgCl ₂ test for 10h	62
4.2.2.3 Base material micrograph after MgCl ₂ test for 72h	62
4.2.3Micro structural characterization of MIG weld specimen after	
MgCl ₂ test for 5 h, 10 h and72h	63
4.2.3.1 Micrographs of MIG welded region after MgCl ₂ test for 5h	63
4.2.3.2 Micrographs of MIG weld samples after MgCl ₂ test for 10h	63
4.2.3.3 Micrographs of MIG welded samples after MgCl ₂ test for 72h	64
4.2.4 Micro structural characterization of Spot welded region of the	
tubes after MgCl ₂ test for 5 h, 10 h, and 72 h	65
4.2.4.1 Spot welded region of the tubes after MgCl ₂ test for 5 h	65
4.2.4.2 Spot welded region of the tubes after MgCl ₂ test for 10h	66
4.2.4.3 Spot welded region of the tubes after MgCl ₂ test for 72 h	66
4.2.5 After post weld heat treatment micro structural characterization of	
LBW, MIG, base metal specimens after 5 h MgCl ₂ test	67
Summary of Part-II	68
4.3 PART-III: Surface engineering of welded tubes of AISI 321 SS for	
preventing chloride induced SCC	69
4.3.1 X-ray diffraction	69
4.3.2 Surface roughness	71
4.3.3 Microhardness	72
4.3.4 SCC susceptibility studies on LBW, MIG, spot weld and base metal of	
AISI 321 SS tubes after buffing	72
Summary of part-III	77
4.4 PART-IV: Mechanistic understanding of the improvement in SCC resistance	e of

buffed AISI 321 SS welded tubes	
CHAPTER 5:	
5.0 Conclusions	82
Scope of future work	83
REFERENCES	84

List of Tables

Table No.	Title	Page No
Table 3.1	Chemical compositions of base metal AISI 321 stainless steel (wt. %)	36
Table 4.1	The chemical composition of σ phase and δ -ferrite obtained from EDS	50
Table 4.2	The grain size of the AISI 321 SS tubes	58
Table 4.3	Full width at half maximum (FWHM) values in buffed and un-buffed 321 SS	70
Table 4.4	Average surface roughness of un-buffed surfaces of 321 SS for LBW, MIG welded and base material	71
Table 4.5	Average surface roughness of buffed surfaces of 321 SS for LBW, MIG welded and base material	71
Table 4.6	Residual stress measurements on the surface of AISI 321 SS tube weld after buffing.	81

List of figures

Figure No	Title	Page No
Figure 2.1	Flow chart showing different grades of austenitic stainless steels	4
Figure 2.2	Phase diagram of solubility of carbon with respect to M ₂₃ C ₆ carbides (M = Cr, Fe, Mo, Ni) in austenitic stainless steel	5
Figure 2.3	Pitting attack at grain boundaries in austenitic SS	7
Figure 2.4	Nitrogen content vs. pitting potential	8
Figure 2.5	The effect of solidification rate on solidification mode	10
Figure 2.6	Effect of temperature on stress corrosion cracking of type 304 stainless steel in MgCl ₂	12
Figure 2.7	Susceptibility to SCC of types 304 and 316 stainless steel in oxygen saturated and nitrogen-saturated MgCl2 solution (U-bend test)	13
Figure 2.8	Effect of MgCl ₂ concentration on time to failure	14
Figure 2.9	Effect of chloride content and temperature on type of corrosion in (a) sodium chloride solutions: initial pH 2, (b) sodium chloride solution: initial pH 7, (c) sodium chloride solution: initial pH 12, (d) magnesium chloride solutions: initial pH 7, (e) calcium chloride solutions: initial pH 7, (f) zinc chloride solutions: initial pH 7	15
Figure 2.10	Stress corrosion cracking susceptibility in boiling MgCl2 as a function of nickel content.	16
Figure 2.11	Comparison of stress corrosion cracking resistance of some austenitic stainless steels, Drop evaporation method testing with loading to 0.9 x Rp0.2	17
Figure 2.12	Different types of welding processes used for welding stainless steels	18
Figure 2.13	Schematic of LASER Hybrid arc welding	20
Figure 2.14	Schematic of Electrical Resistance Spot Welding Technique	21
Figure 2.15	Threshold stresses for chloride stress corrosion cracking under severe evaporative conditions	22
Figure 2.16	Schematic of the concentrated solar thermal power plant (Parabolic trough reflectors)	24
Figure 2.17	Different types of solar collectors	25
Figure 2.18	Schematic diagram of a flat-plate collector	26
Figure 2.19	Schematic diagram of an evacuated tube collector	28
Figure 2.20	Schematic of heat pipe evacuated tube collector	29
Figure 3.1	Shows the FESEM microstructure of the AISI 321 stainless steel	35
Figure 3.2	AISI 321 SS heat exchanger tube indicating the location of seam weld	36

	and spot weld	
Figure 3.3	Dye penetrate test (DPT) images of AISI 321 stainless steel tubes.	37
	Boiling magnesium chloride test setup [ASTM G36-94] for	
Figure 3.4	evaluating SCC resistance of metals and alloys in a boiling MgCl ₂	41
	solution, (1) Erlenmeyer flask, (2) condenser, (3) water inlet and outlet,	41
	(4) thermometer, (5) heater.	
Figure 4.1	shows the schematic of solar thermal power plant	43
Figure 4.2	(a) shows the actual plant AISI 321 SS tube (b) shows the	43
Figure 4.2	schematic of AISI 321 stainless steel tube heat exchanger	43
Figure 4.3	shows the heat exchanger tube and location of the spot weld	44
	(a) Shows the cracks on the outer surface of the tube near the spot weld	
Figure 4.4	and (b) shows the cracks detected on the inner surface of the tube near	44
	the spot weld by dye penetration test	
Figure 4.5	X-ray diffraction spectra of the different weld regions on AISI 321 SS	45
Figure 4.6	Micro hardness profiles of the differently welded AISI 321 SS tubes	46
Figure 4.7	FESEM micrograph of the AISI 321 stainless steel base material	47
	FESEM microstructure of AISI 321 SS tube showing different	
Figure 4.8	precipitates at different regions, (a) Ti_2N , (b) σ and δ -ferrite (10N KOH	48
	solution), (c) Ti (C, N), and (d) δ -ferrite	
Figure 4.9	EDS spectra of Ti ₂ N (EDS spot 1) and Ti (C, N) (EDS spot 2)	49
Figure 4.10	FESEM electron image and EDS spectrum of sigma (σ)	51
Figure 4.11	Electron image and EDS spectrum of delta (δ-ferrite)	52
Figure 4.12	The optical micrographs of cracks in the spot welded region of AISI 321	53
Figure 4.12	SS tube	33
Figure 4.13	The magnified view of the cracked region	53
Figure 4.14	FESEM micrograph of Laser beam weld (LBW)	54
Figure 4 15	FESEM micrograph of the interface of the fusion zone and base metal of	55
Figure 4.15	laser beam weld	33
Figure 4.16	FESEM micrograph of LBW 321 SS tube showing the interface of	55
Figure 4.10	fusion zone and base material	33
Figure 4.17	FESEM micrograph of LBW 321 SS tube showing slip bands and flow	56
riguic 4.17	lines in the base material region away from the weld zone	30
Figure 4.18	FESEM micrographs of the different regions of MIG welded AISI 321	
	stainless steel (a) polygonal grains in the base metal (b) dendritic	57
	structure in the fusion zone	
Figure 4.19	FESEM cross sectional micrographs of a) MIG welded AISI 321	
	stainless steel tube near the weld interface and b) distribution of σ phase	57
	(etched using 10N KOH solution) and δ ferrite near the interface of	

	fusion zone and base metal.	
	(a) FESEM micrographs of LBW welded tubes surface after boiling	
Figure 4.20	magnesium chloride test for 5h and (b) optical micrograph of cross	59
	section near LBW welded zone after 5h test	
Figure 4.21	FESEM micrographs of LBW welded tubes after boiling magnesium	60
	chloride test for 10h; (a) surface and (b) cross section	00
Eignes 4 22	FESEM cross section micrographs of LBW weld sample after MgCl ₂	60
Figure 4.22	test for 10 h	60
Figure 4.22	Optical micrographs of LBW weld after MgCl ₂ test for 72 h. (a) surface	61
Figure 4.23	and (b) cross section	01
Eigene 4 24	Optical micrographs of base material after boiling MgCl ₂ test for 5h; (a)	<i>c</i> 1
Figure 4.24	surface and (b) cross section	61
Ei 4 25	Optical micrographs of base material after boiling MgCl ₂ test for 10h;	(2)
Figure 4.25	(a) surface and (b) cross section	62
Eigen 4 26	Optical micrographs of base material cross section after boiling MgCl ₂	62
Figure 4.26	test for 72h	62
	(a) FESEM micrographs of MIG welded tube surface and (b) optical	
Figure 4.27	micrograph of MIG welded tube cross section after exposing it to MgCl ₂	63
	test for 5h	
	(a) FESEM micrographs of MIG welded tube surface and (b) optical	
Figure 4.28	micrograph of MIG welded tube cross section after boiling MgCl ₂ test	63
	for 10h	
Figure 4.20	FESEM micrographs of MIG weld Cross section after MgCl ₂ test for	64
Figure 4.29	10h	04
Figure 4.20	(a) and (b) are the optical micrograph of MIG weld cross section after	64
Figure 4.30	MgCl ₂ test for 72h.	04
	(a) FESEM micrograph of the spot welded region surface and (b) Optical	
Figure 4.31	micrograph spot welded region cross section of the tube after MgCl ₂ test	65
	for 5 h	
	(a) FESEM micrograph of Spot welded region surface and (b) optical	
Figure 4.32	micrograph Spot welded region cross section of the tubes after MgCl ₂	66
	test for	
Eigen 4 22	Optical micrograph spot welded region of the tubes after MgCl ₂ test for	67
Figure 4.33	72 h	07
Figure 4.34	FESEM Surface micrographs of a) LBW, b) Base metal and c) MIG and	
	(d, e, f) shows the cross sectional micrographs of LBW, Base metal and	68
	MIG respectively After 5 h MgCl ₂ test	
Figure 4.35	XRD pattern of LBW, MIG welded and base material of AISI 321 SS	70

	tubes in buffed and un-buffed condition.	
Figure 4.36	Hardness profiles of the different weld joints of AISI 321 SS tubes after buffing operation	72
Figure 4.37	FESEM micrographs of the surface of LBW 321 SS in buffed and unbuffed condition after SCC tests (a) un-buffed; 5 h exposure (b) buffed; 5 h exposure, (c) un-buffed; 10 h exposure and (d) buffed; 10 h exposure	74
Figure 4.38	FESEM micrographs of the surface of MIG 321 SS in buffed and unbuffed condition after SCC tests (a) un-buffed; 5 h exposure (b) buffed; 5 h exposure, (c) un-buffed; 10 h exposure and (d) buffed; 10 h exposure	75
Figure 4.39	FESEM micrographs of the surface of spot weld 321 SS in buffed and un-buffed condition after SCC tests (a) un-buffed; 5 h exposure (b) buffed; 5 h exposure, (c) un-buffed; 10 h exposure and (d) buffed; 10 h exposure	76
Figure 4.40	FESEM micrographs of the surface of base material 321 SS in buffed and un-buffed condition after SCC tests (a) un-buffed; 5 h exposure (b) buffed; 5 h exposure, (c) un-buffed; 10 h exposure and (d) buffed; 10 h exposure	77
Figure 4.41	Schematic showing the factors responsible in causing SCC	78
Figure 4.42	Schematic showing factors responsible in causing reducing SCC	79
Figure 4.43	Schematic of the buffing operation	80
Figure 4.44	Schematic of the buffing operation for inner surface of the tube	80

LIST OF PUBLICATIONS/CONFERENCES

Journal Publications

- Kamal Mankari, Swati Ghosh Acharyya, "Development of stress corrosion cracking resistant welds of 321 stainless steel by simple surface engineering", Applied Surface Science, Volume 426, 2017, Pages 944-950.
 (https://doi.org/10.1016/j.apsusc.2017.07.223)
- Kamal Mankari and Swati Ghosh Acharyya, "Failure of AISI 321 stainless steel welded pipes in solar thermal power plants", in Engineering Failure Analysis, Volume 86, April 2018, Pages 33–43

(https://doi.rg/10.1016/j.engfailanal.2017.12.020).

Conference Proceedings

- 1. **Kamal Mankari**, Swati Ghosh Acharyya, "Cracking of AISI 321 stainless steel welds in solar thermal power plant: Root cause analysis", Conference Proceeding in NIGIS, CORCON 2017, 17-20 September, Mumbai, India.
- Kamal Mankari, Pandu Sunil Kumar, Swati Ghosh Acharyya "Distinguishing effect of buffing on residual stress distribution and susceptibility of austenitic stainless steel to stress corrosion cracking" Materials Research Proceedings 6 (2018) 139-144 (http://dx.doi.org/10.21741/9781945291890-22).

International Conferences attended

- 1. "SCC of AISI 321 Stainless steel welds in solar power plants", The International Institute of Welding- 6th Welding Research and Collaboration Colloquium, 7-9 April, 2016 at Hyderabad.
- "Cracking of AISI 321 Stainless steel welds in solar thermal power plant: Root cause Analysis", International Conference: CORCON, held during 17-19 September, 2017 at Mumbai.

LIST OF ABBREVIATIONS

SS Stainless steel

AISI American iron and steel institute

Nb Niobium
Ti Titanium

LBW Laser beam welding

MIG Metal inert gas welding

SCC Stress corrosion cracking

XRD X-ray diffraction

ASTM American Society for testing and materials

MgCl₂ Magnesium chloride

TIG Gas tungsten arc welding

FCC Face-centered cubic

Cr Chromium Al Aluminum

Cu Copper

Mo Molybdenum

BCC Body-centered-cubic

BCT Body centered tetragonal

TEM Transmission electron microscopy

HAZ Heat affected zone

KLA Knife line attack

 δ Delta ferrite

 σ Sigma phase

LSND Low stress non-distortion welding

LPHSW Last pass heat sink welding

LSP Laser shock processing

LPB Low plasticity burnishing

IHSI Induction heating stress improvement

LPB Low plasticity burnishing

MSIP Mechanical stress improvement procedures

IG Intergranular

DPT Dye penetrant test

LPT Liquid penetrant test

FESEM Field emission scanning electron microscopy

EDAX Energy dispersive analysis of X-rays

SFPM Surface feet per minute Rpm Revolutions per minute

v Poisson's ratio

γ Austenitic phase

JCPDS Joint committee on powder diffraction standards

ETCs Evacuated tube collectors

DSG Direct steam generation

FPC Flat plate collectors

CPC Compound parabolic concentrator

CSP concentrated solar power

CPC Compound parabolic concentrator

PTC parabolic trough collector

ABSTRACT

Failure of AISI 321 SS tubes used for transport of hot thermic fluid in solar thermal power plants has been studied here with two primary objectives a) to understand the mechanism behind the failure b) to provide a solution to prevent such failures. The AISI 321 stainless steels tubes were seam welded either by laser beam welding (LBW) or by metal inert gas welding (MIG) together with spot welds at selected locations on the surface. The cracks were identified using dye penetration tests followed by microstructural characterization using optical microscopy (OM), field emission scanning electron microscopy (FESEM) and phase determination using X-ray diffraction (XRD). The surface roughness was measured using optical surface profilometer. Stress corrosion cracking (SCC) tests as per ASTM G36 tests were carried out on the tubes for 5 h, 10 h, and 72 h to check whether the tensile residual stress levels were above or below the threshold level. Detailed investigation revealed that leakage in each case occurred near spot welded joints due to high tensile residual stresses and chloride-induced SCC of AISI 321 SS. SCC susceptibility tests of the welds showed that both the seam welds and the spot welds had tensile residual stresses beyond the threshold limit due to improper post weld heat treatment. The spot welded region experienced early nucleation and propagation of cracks in presence of chloride ions leading to leakage. The application of post weld heat treatment is often difficult for large industrial components hence alternately surface buffing treatment has been proposed and proved to be a simple and innovative approach to enhance the SCC resistance of AISI 321 SS. The outer and inner surfaces of each of the welded tubes were subjected to buffing operation followed by determination of residual stress distribution and surface roughness by XRD and surface profilometer measurements respectively. The buffed surfaces were exposed to SCC tests under similar conditions as per ASTM G36. The results showed that the buffed surfaces were resistant to SCC whereas the un-buffed surfaces underwent severe SCC for the same exposure. Buffing imparted high magnitude of compressive residual stresses on the SS surface, without inducing any additional plastic strain, unlike shot peening and laser peening operations which led to increase in SCC resistance of the welds in presence of chloride ions.

CHAPTER 1

1.0 Introduction

1.1 Background

Austenitic stainless steels find numerous applications in different industrial sectors due to its high strength, good weldability, and good corrosion resistance. However, these steels are susceptible to localized corrosion, like pitting, crevice corrosion and stress corrosion cracking (SCC) which can lead to failure in chemical, petrochemical industries, power plants, and civil structures etc. [1-7]. SCC is a phenomenon wherein cracking takes place under the synergistic action of tensile stresses, aggressive environment, and a susceptible material, failure occurs without any warning. The stresses present in the material may either be in-service stresses or residual stresses. Tensile residual stresses arise in the material due to different steps involved in component fabrication like bulk deformation, surface finishing techniques like grinding, turning, and welding etc. [8-9]. Welding generally results in the development of a high magnitude of tensile residual stresses due to the constrained weld geometry. The thermal expansion and contraction of the alloy during welding gets restricted due to the constraint geometry resulting in the development of a high magnitude of tensile residual stresses. The magnitude and nature of residual stress distribution in the component depends on the nature of welding and the welding parameters such as welding speed, heat input, time for cooling etc. [10]. Compressive residual stresses are beneficial to reduce the susceptibility towards SCC [11-16]. Some of the techniques which induce compressive residual stresses on the surface are shot peening, LASER shock peening, ultrasonic peening, water jet peening, and burnishing which induces compressive residual stresses on the surfaces induces high surface strain and result in increased surface roughness [17-22]. Surface buffing, on the other hand, has many advantages like reduced surface roughness, minimum plastic strain together with the generation of compressive residual stresses [12]. The present study deals with SCC resistance of AISI 321 SS tubes which are used in solar thermal power plants for transport of thermic fluid containing chloride ions. Several of these SS tubes fail while in service after very short exposure to service conditions leading to leakage of the thermic fluid. The study has been initiated by root cause analysis followed by a mechanistic understanding of the cause and finally an innovative approach has been applied to scientifically solve the issue.

1.2 Objectives of the thesis

The four primary objectives of the thesis are listed as follows:

- To establish the root cause and mechanism of failure of AISI 321 SS tubes in a solar thermal power plant.
- To determine whether residual stress levels in a) LASER welded, b) MIG welded, c) spot welded AISI 321 stainless steel tubes are above the threshold level for chloride induced SCC.
- To enhance the SCC resistant of 321 SS tubes by surface engineering.
- Delineating the mechanism behind enhanced resistance of 304L SS against chloride induced SCC.

1.3 Thesis Layout

Chapter 1 gives a background to the study. Chapter 2 gives the review of the corrosion issues in stainless steel components used in solar thermal power plant. Chapter 3 gives the scheme of experiments carried out for the study together with experimental details. Chapter 4 gives the results and discussion and is sub divided into three sections which are as follows:

- **Part1:** Root cause analysis of failure of AISI 321 SS welded tubes in the solar thermal power plant
- Part 2: Determination of stress corrosion cracking (SCC) susceptibility of LBW, MIG and spot welded AISI 321 SS tubes
- **Part 3:** Prevention of chloride induced SCC in welded tubes of AISI 321 SS by simple surface buffing operation
- Part 4: Mechanistic understanding of the effect of buffing operation on the SCC resistance of AISI 321 SS

Chapter 5 presents the conclusions followed by future directions of research and references.

CHAPTER 2

2.0 Literature review

2.1 Austenitic stainless steels

Generally austenitic stainless steels contain 18-25 wt % of Cr, 8-20 wt % of Ni and carbon content is > 0.08 wt %. Austenitic stainless steels also have some other alloying elements such as Mo, N, Nb or Ti. A composition of some austenitic stainless steels is as shown in Figure 2.1.Austenitic stainless steels are non-heat treatable. Addition of Nitrogen (N) to the austenitic stainless steels gives higher strength [32], toughness, corrosion resistance, non-ferromagnetic behavior, and higher creep resistance [23]. Ferrite stabilizers such as Mo and Nb or Ti leads to the formation of alpha (α) and sigma (σ) phase in austenitic stainless steels [33]. Presence of both austenite and ferrite phase in stainless steel was observed when the Mo is increased to 2 wt %. Further, Mo forms as an intermetallic sigma phase, which causes room temperature embrittlement [33]. The other alloying elements also play an important role in accordance with the austenite or ferrite-forming elements. These alloying elements may increase or decrease the tendency towards the formation of delta-ferrite at solution-treatment temperature. Further, the austenitic stainless steels have been classified into un-stabilized and stabilized grades [32, 34].

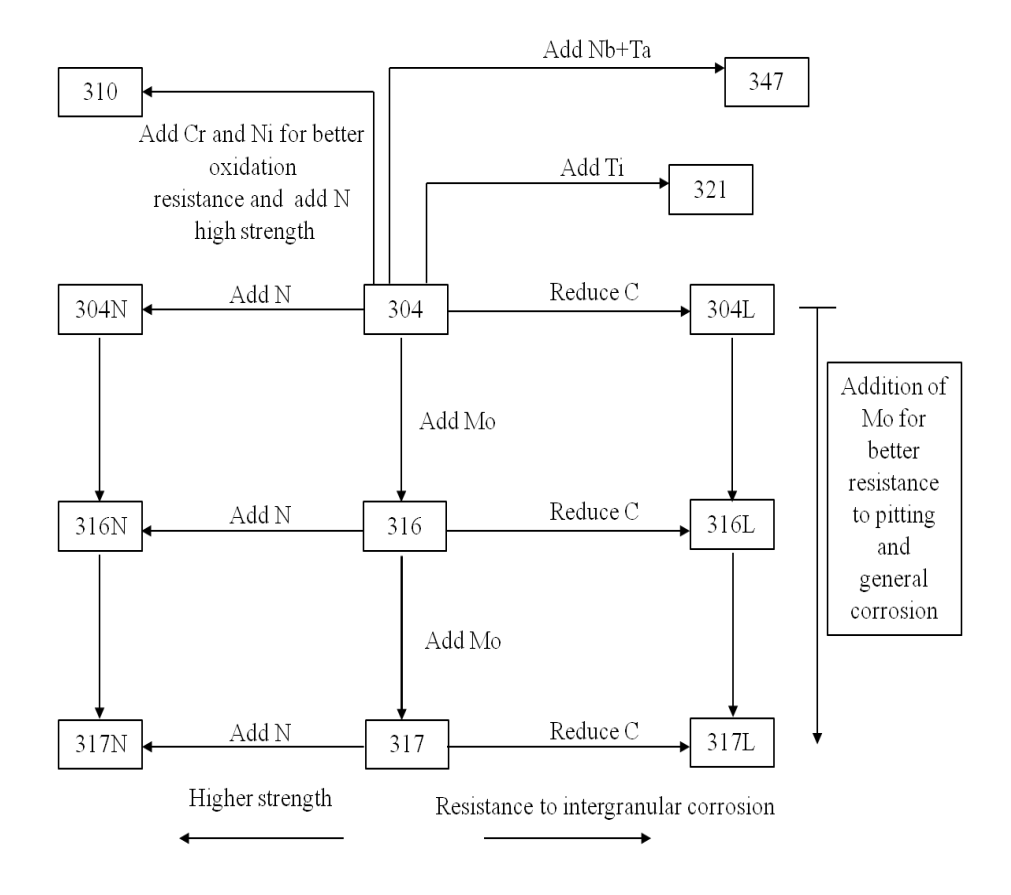


Figure 2.1 Flow chart showing different grades of austenitic stainless steels

2.1.1 Un-stabilized grades of austenitic stainless steels like AISI 304 and AISI 316

The carbon content in austenitic stainless steels (un-stabilized grade) is up to 0.15 wt % above the austenitizing temperature (1100°C) which is followed by rapid cooling which results in the retainment of carbon in solid solution. Where the alloy is exposed to a temperature between 450° C and 850° C followed by slow cooling, carbon leads to the formation of the Cr–carbides ($M_{23}C_6$) at the grain boundaries. Figure 2.2 shows the phase diagram of solubility of carbon with respect to $M_{23}C_6$ carbides. Presence of Mo decreases the solubility of carbon in austenite and accelerates the Cr-carbide precipitation. [32].

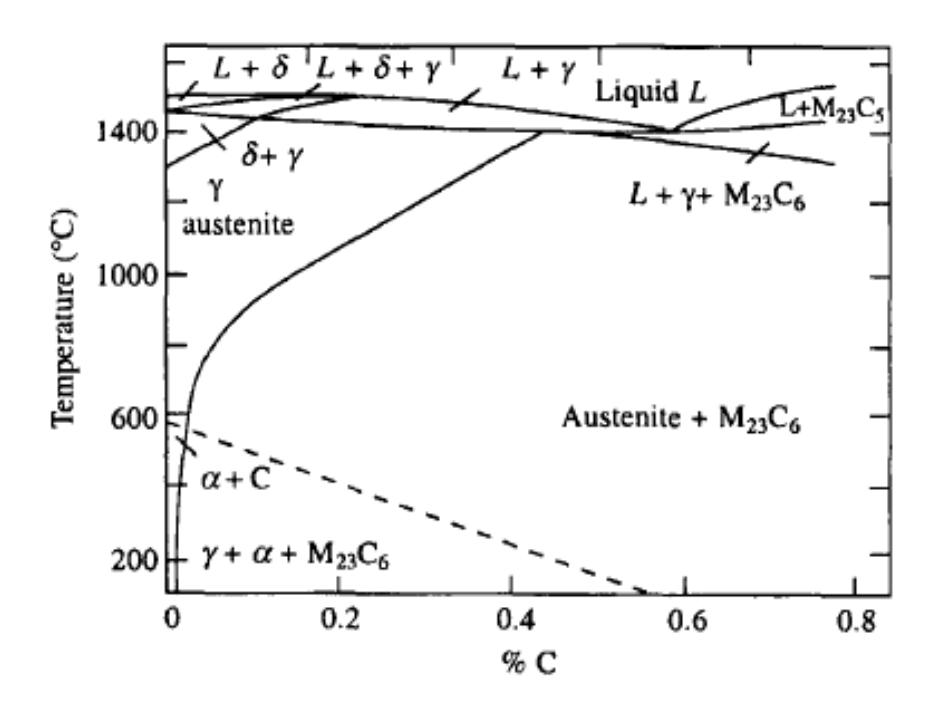


Figure 2.2 Phase diagram of solubility of carbon with respect to $M_{23}C_6$ carbides (M = Cr, Fe, Mo, Ni) in austenitic stainless steel [32]

2.1.2 Stabilized grades like AISI 321 and AISI 347

Sensitization of austenitic stainless steel is prevented by the addition of stabilizers like Ti and Nb. Ti and Nb when added to austenitic stainless steels (stabilized grade) results in the formation of titanium carbides, titanium nitrides in AISI 321 stainless steels and niobium carbides and niobium nitrides in AISI 347 stainless steels before the formation of chromium carbide, hence protecting the steel from getting sensitized. The extent of precipitation of Titanium or Niobium rich carbides depends on its solubility in the austenitic matrix. The higher the solubility, lower the precipitation. The following relation gives the solubility of titanium and niobium carbides in 18Cr-12Ni steel [21], as given in the equation (equation 2.1 and 2.2).

In correspondence to the general equation which is given as in equation (equation 2.3)

where; M wt. % of the element to be added as stabilizer

X wt. % of carbon

A constant,

H is the heat of dissolution,

R is the perfect gas constant and

T is the absolute temperature. [32]

2.2 Corrosion issues in austenitic stainless steels

The formation of a passive film at the surface of stainless steel is the key to its high corrosion resistance. However, the passive film forms only when the percentage of chromium is greater than 12 wt %. This passive film consists of mixed oxides of Cr and Fe, which gives excellent corrosion resistance in different types of chemical environments [36]. This film has the ability to rebuild itself by oxidation of the underlying metal when it has been damaged. However, when the passive layer is broken down locally, it leads to localized corrosion of 321 SS. Different types of localized corrosion in austenitic stainless steel welds are as follows

- 1. Pitting corrosion
- 2. Intergranular corrosion
- 3. Hot cracking
- 4. Stress corrosion cracking

2.2.1 Pitting corrosion

Pitting corrosion is a localized form of corrosion by which cavities or holes are produced in the material. Pitting is considered to be more dangerous than uniform corrosion damage because it is more difficult to detect and predict. Pitting corrosion occurs where chloride ions cause a local breakdown of the passive layer. Major metallurgical variables on pitting corrosion of austenitic stainless steels are given below.

2.2.1.1 Effect of microstructure

Pitting corrosion causes a severe reduction in performance in engineering components either by directly damaging the structure or by providing sites of the pit for the stress corrosion cracks to initiate and propagate [37]. The pitting generally starts at the grain boundaries, inclusions, mechanical scratches, slips, second phase precipitates and other heterogeneities existing on the surface. Figure 2.3 shows the pitting attack at the grain boundaries in the austenitic SS [38]. Pitting primarily starts at the grain boundaries because during carbide precipitation the Cr and other alloying elements depletion occurs at this region [39].

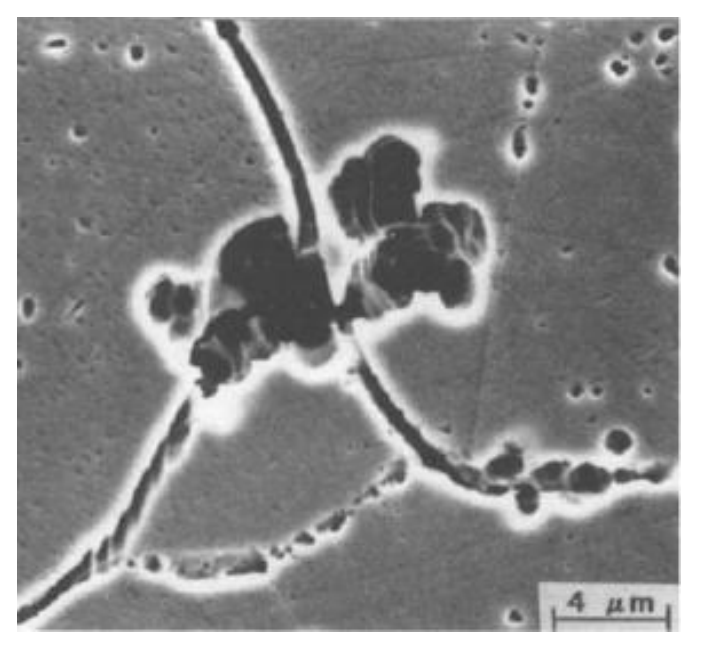


Figure 2.3 Pitting attack at grain boundaries in austenitic SS [39]

2.2.1.2 Inclusions

Pitting attacks at the inclusion can occur in three different stages, they are as follows:

- Inclusion dissolution and initiation of micro-cavities,
- Agglomerating of chloride ions at micro-cavities and
- Initiation and growth of pits at such sites.

Inclusions such as sulphide inclusions like (MnS) have high conductivity compared to the surrounding oxide film [38]. Under chlorides environments, these ions are adsorbed on the surface, wherein the adsorbed chloride ions facilitate the anodic dissolution of sulphide inclusions. The corrosion potential of a passive stainless steel surface in a chloride solution is generally in between 0

to + 200mV. Moreover, this potential range makes the sulphide thermodynamically unstable and tends to dissolve as per the potential-pH diagram of MnS-H₂O-Cl system [39]. When the sulphide dissolves, a part of the metal surface is exposed to the environment and pits continue to grow there with time.

2.2.1.3 Alloy Composition

The chemical composition of the alloy also plays a major role in the pitting resistance. In stainless steels, Cr, Mo, Ni is the main alloying elements which decrease the pitting. Increase in the chromium content enhances the stability of the passive film, while the increase in the nickel content delayed the decrease in pH during pit growth by neutralizing the solution in the pit. Mo is specifically added to improve the localized corrosion resistance and mechanical properties at elevated temperatures. Mo containing steel showed a slower pit growth than of the Mo-free steel [40], the exact mechanism by which Mo improves the pitting resistance is still not clear. Small additions of Ti are beneficial in improving the pitting resistance [38, 40-43]. But the effect is minimal at a higher percentage of Ti (1.8 wt %), which is due to the formation of new phases which are susceptible to pitting attack [43]. Addition of N as an alloying element to austenitic SS promotes the passivity. This addition of N widens the passive range in which probability of pitting is negligible [44-48] the addition of N has been reported to improve the pitting corrosion resistance of austenitic stainless steels as shown in Figure 2.4 [49].

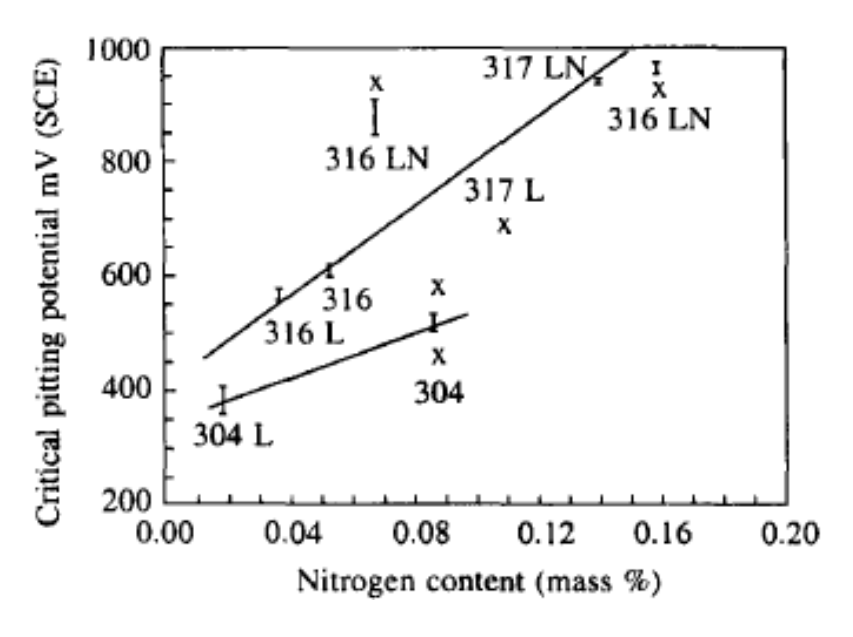


Figure 2.4 Nitrogen content vs. pitting potential [49]

The surface finish also plays a major role in increasing the pitting resistance of stainless steels. The resistance to pitting changes with the degree of mechanical polishing, a higher degree of mechanical polishing leads the resistance towards pitting, as mechanical polishing covers grain boundaries and inclusions with the flowed metal.

2.2.2 Intergranular corrosion (IGC)

The austenitic stainless steels are resistant to general corrosion, but during welding, these steels are susceptible to IGC due to sensitization, Sensitization of the heat affected zone (HAZ) takes place due to which the corrosion resistance of the welds is decreased [38]. This phenomenon generally occurs when the steel is held for a long time in the temperature range of 450-850°C. Precipitation of Cr-rich carbides along grain boundaries takes place at this temperature range leading to the formation of chromium depleted zone near the grain boundaries. Sensitization of the welds can be prevented by a) reducing the wt% of C in the steel or b) by addition of stabilizing elements like Ti and Nb which form carbides earlier than Cr [29].

However, stabilized grades of austenitic SS are also observed to undergo 'knife line attack' (KLA) due to the improper post weld heat treatments [38]. Knife line attack is a localized form of intergranular corrosion that occurs adjacent to the weld pool in type 321 and 347 austenitic stainless steels. The region near the weld pool experiences very high temperatures leading to the dissolution of carbides of Ti or Nb in stainless steel. Subsequently, stress relief annealing treatment results in the chromium carbide precipitation just adjacent of the weld pool leading to sensitization in a very narrow zone [27]. This type of corrosion is called KLA.

2.2.3 Hot cracking

Hot cracking or solidification cracking resistance of austenitic SS welds has been considered based on the solidification modes and the nickel/chromium equivalents in welding processes, where the cooling rates are high. Kujanpää *et al.* [50] reported that the austenitic, stainless steels usually solidify as single-phase ferritic mode. This forms an essential part of microstructure transforming to austenite (100 %) during cooling at room temperature without any ferrite, showing an essential effect on stress corrosion cracking. The solidification mode is strongly dependent on the composition. From Figure 2.5 it is evident that the solidification modes can be calculated by chromium/nickel equivalents [50]. If the ratio of chromium/nickel equivalents is below 1.5,

solidification results are fully austenitic or austenitic-ferritic structure and when it ranges between (1.5-2.0) it is ferritic – austenitic [51].

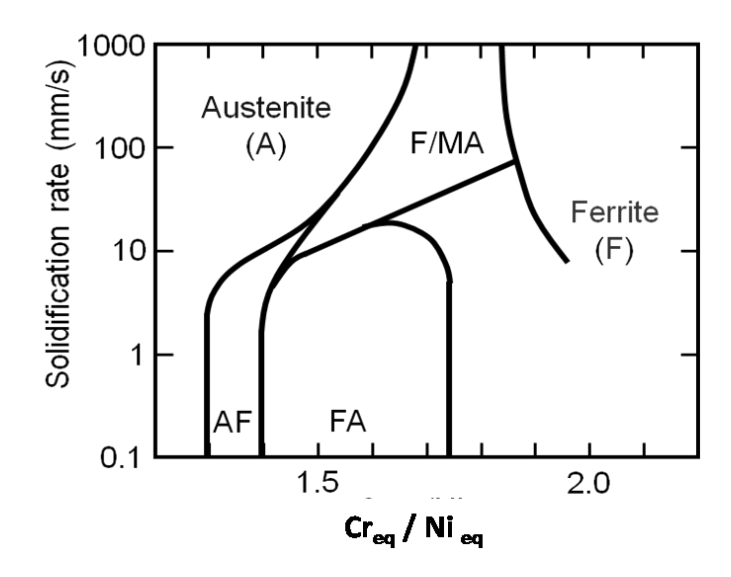


Figure 2.5 The effect of solidification rate on solidification mode [50]

The formation of hot cracking could depend on weld design and composition of filler metal. However, a lower hot cracking susceptibility was observed when the weld pool was wider and of the primarily ferritic structure. Presence of a minimum amount of δ -ferrite helped to prevent hot cracking in welds [38] due to the synergistic effect of the following reasons.

- (1) The impurity elements are highly soluble in the δ -ferrite which results in a decrease in interdendritic segregation.
- (2) The austenite-ferrite interface followed an asymmetric path which prevented crack generation.
- (3) γ – δ boundary has lesser surface energy and also has decreased wet ability characteristics to eutectic films when compared to γ – γ or δ – δ interfaces.
- (4) The ferrite formation resulted in a larger interfacial region because of its solid state transformation to austenite which is initiated immediately after solidification.
- (5) Ferrite is found to be more ductile at elevated temperatures when compared to austenite which results in relaxation of thermal stresses.
- (6) Ferrite has a lesser coefficient of thermal expansion when compared to austenite which leads to lower contraction stresses.

- (7) The welds of primary ferrite have a lower solidification temperature range than the solidification range of primary austenite. As a result, they provide a lower critical temperature range for cracking.
- (8) Delta ferrite helps in grain size refinement during solidification of the metal, leading to superior mechanical properties and better resistance to cracking.

2.2.4 Stress corrosion cracking (SCC)

SCC of austenitic stainless steel welds is a major issue widespread in the industrial sector. SCC occurs as a synergistic effect of a) tensile stresses, b) susceptible material and c) aggressive environment.

2.2.4.1 Tensile Stresses:

Tensile stresses are generated in the material in the form of applied load or residual stress during service or welding make a material susceptible to SCC. The threshold limit of residual stress of material for SCC initiation depends on microstructure and the aggressiveness of the service environment. For e.g. in hot chloride condition, the stresses required to induce SCC is as low as 20 % yield stress [22].

2.2.4.2 Environment factors:

Materials become susceptible to SCC only in the presence of a specific environment. Temperature, pH, a concentration of ions, a conductivity of the environment determines its aggressiveness. Hot concentrated hydroxides have been identified to be the cause of failure in boilers and other steam generating equipment's.

• Temperature effect

At higher temperature, the time to failure is shorter. The crack initiation time and crack propagation time are not that easy to distinguish experimentally. The total time to failure is mostly reported. Kowaka *et.al* [52] showed the apparent activation energy to be between 54 and 96 kJ/mol (Figure 2.6).

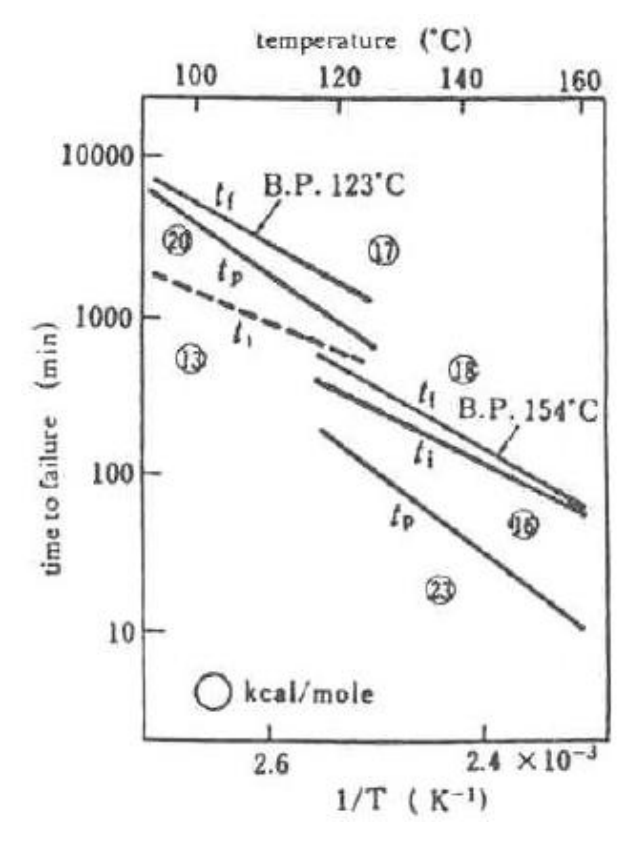


Figure 2.6 Effect of temperature on stress corrosion cracking of type 304

stainless steel in MgCl₂ [52]

pH effect

Uniform corrosion can be predominate if the pH level is below 2, but recent reports show that chloride induced stress corrosion cracking does occur at a low pH level at room temperature [53]. In general, the time to failure is longer at higher pH levels [54].

Dissolved Oxygen

The time to failure in an oxygenated environment is shorter, as shown in Figure 2.7 which compares cracking in oxygenated and nitrogen purged in chloride solutions. The greater severity of cracking in the oxygenated solution supports the role of anodic dissolution in crack growth.

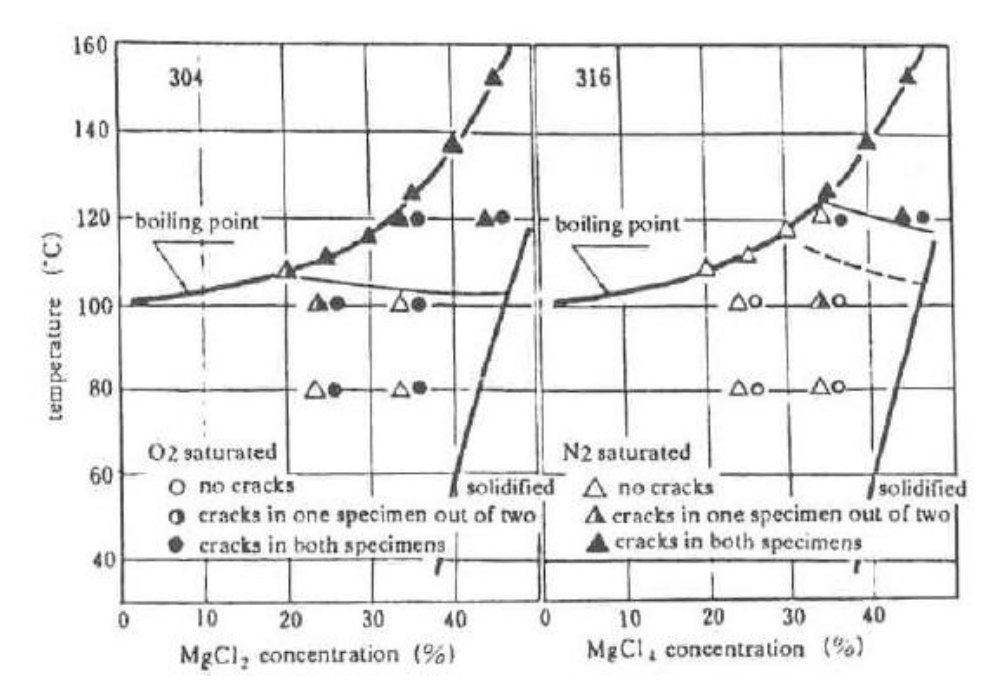


Figure 2.7 Susceptibility to SCC of types 304 and 316 stainless steel in oxygen saturated and nitrogen-saturated MgCl2 solution (U-bend test) [52]

• The Effect of Chloride Ion Concentration

The effect of increasing the chloride concentration is to accelerate [54] the cracking. Edeleanu *et.al* data also include a temperature effect of MgCl₂, concentration on the cracking type 304 and 321 type stainless steels [34] as shown in Figure 2.8. Truman conducts the different solutions used those are chlorides of sodium, magnesium, calcium or zinc in de-mineralized water. The standard pH was 7 with values of 2 and 12 also being used in the case of sodium chloride adjustments of pH were made by additions of hydrochloric acid or of sodium hydroxide on type 304 SS. Temperatures were maintained at 20, 40, 60, 80°C or boiling point by immersion of the flasks in thermostatically controlled baths or on hot plates shown Figure 2.9.

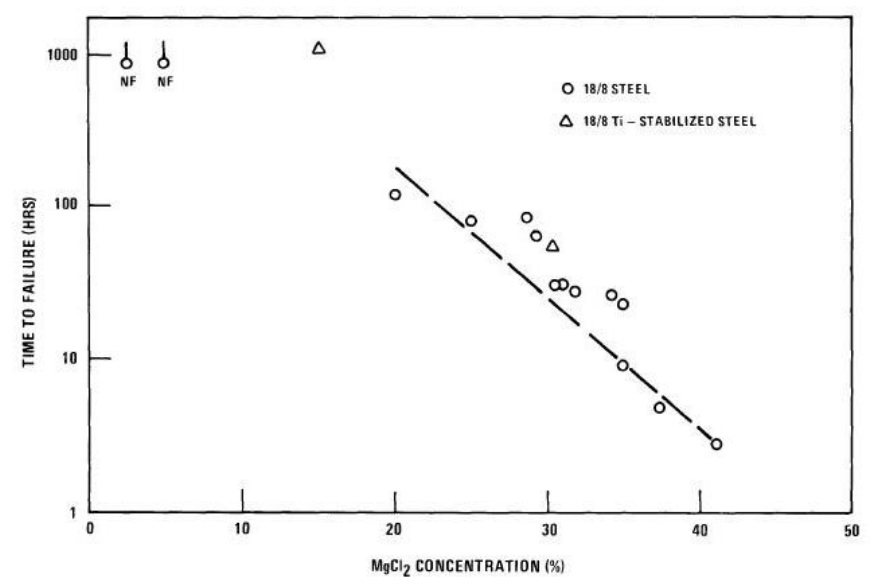


Figure 2.8 Effect of MgCl₂ concentration on time to failure [34].

In only one instance was cracking noted at a temperature below 80° C (in a sodium chloride solution of pH 2 at 60° C) and thus the results are in line with service experience where failure at temperatures below 80° C is rare, and also note that SCC, can occur at lower temperatures under specific, strongly acid conditions or when the steel is coated with moist chloride deposits a but such conditions rarely apply in practice. Chloride concentration in the range 5×10^2 - 10^5 ppm had little effect on the incidence of SCC, although there was some indication of increasing time to initiation with decreasing chloride content. [55] SCC incidence was lower at 10^2 ppm chloride and presumably would be even less with smaller chloride contents. Some slight effect of cation species may be inferred from the results with the apparent order of severity being Na > Mg >Ca> Zn. These trends appear to apply both to the incidence of SCC and time to initiation. There were no significant differences between changes of pH during the test with the various salts. Temperature is a very important feature and in this series of tests no SCC was observed for tests carried out at temperatures below 60° C.

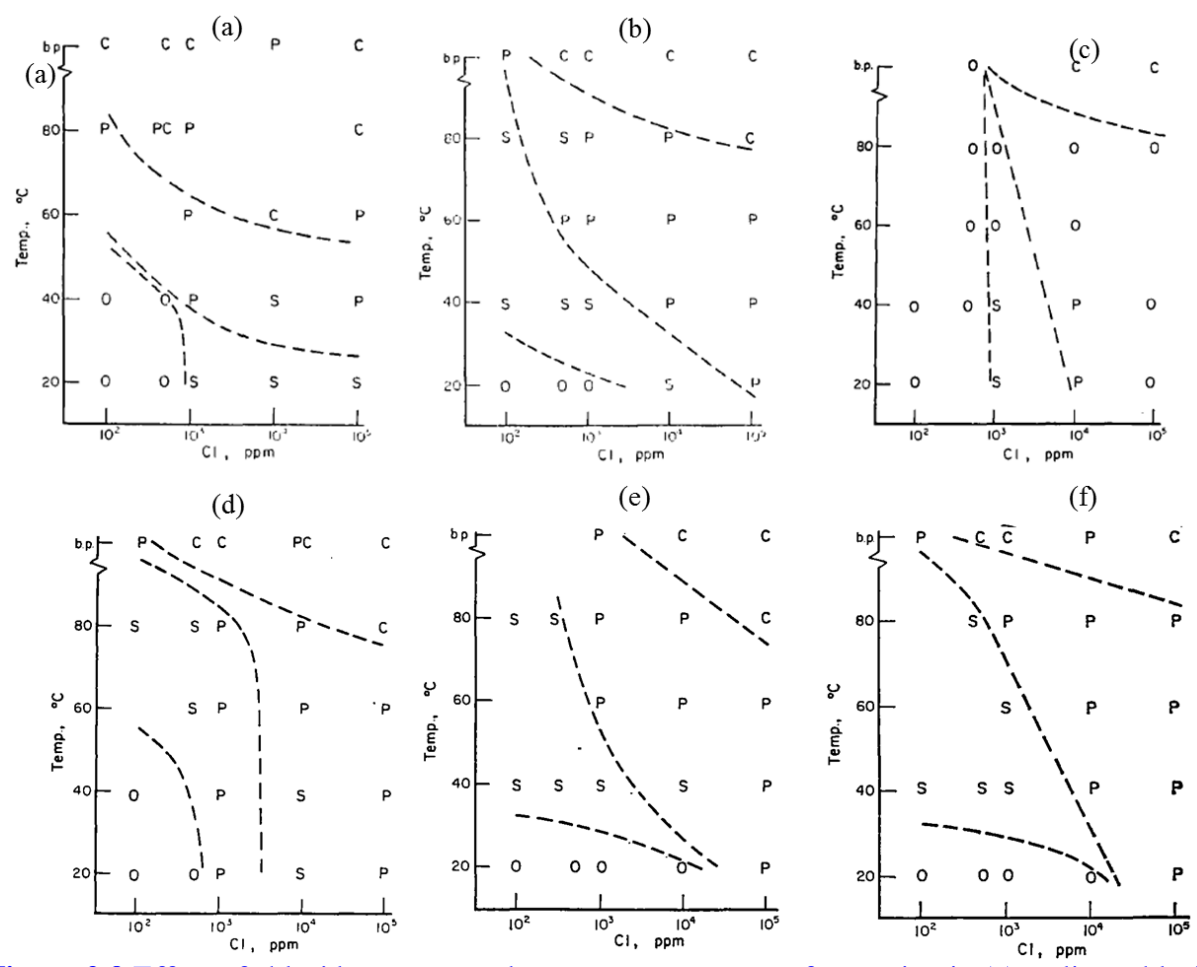


Figure 2.9 Effect of chloride content and temperature on type of corrosion in (a) sodium chloride solutions: initial pH 2, (b) sodium chloride solution: initial pH 7, (c) sodium chloride solution: initial pH 12, (d) magnesium chloride solutions: initial pH 7, (e) calcium chloride solutions: initial pH 7, (f) zinc chloride solutions: initial pH 7[55].

O = Unaffected.

C = Cracked.

P = Pitted.

S = Stained with no visible corrosion.

2.2.4.3 Susceptible material

The material properties such as surface roughness, stacking fault energy, microstructure plays a major role in determining its susceptibility to stress corrosion cracking. Homogenous microstructure, high stacking fault energy, and low surface roughness are desirable for achieving greater resistance to SCC. Alloy composition including the concentration of impurity and the

presence of trace elements influences the SCC properties of metals and alloys. [56] Cracking may also occur in high strength stainless steels, such as martensitic or precipitation hardening steels. This type of cracking is almost always due to hydrogen embrittlement and can occur in both environments containing sulphides and environments free of sulphides. The risk for stress corrosion cracking (SCC) is strongly affected by both the nickel content and the microstructure. The effect of nickel content is apparent in Figure 2.10. Both high and low nickel contents give better resistance to stress corrosion cracking. In the case of the low nickel contents, this is due to the structure being either ferritic or ferritic-austenitic. The ferrite phase in stainless steels with low nickel content is very resistant to stress corrosion cracking.

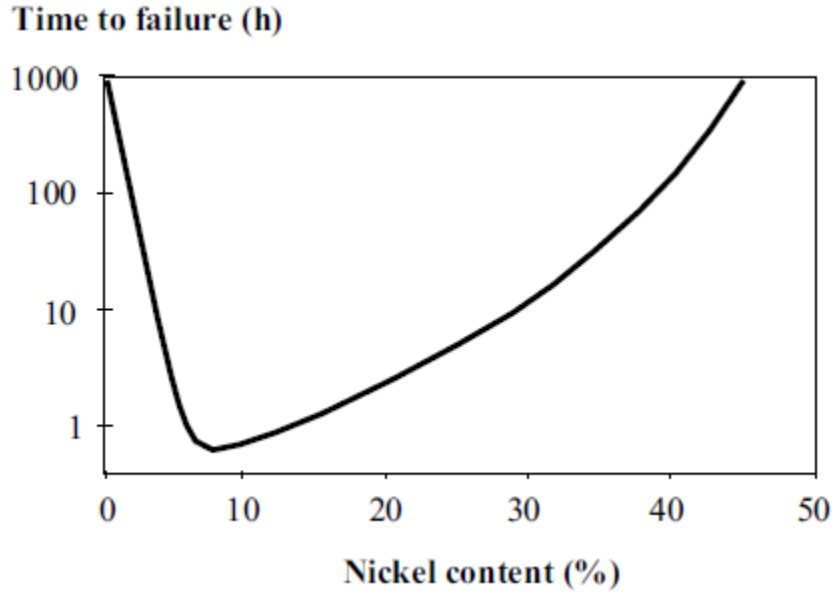


Figure 2.10 Stress corrosion cracking susceptibility in boiling MgCl2 as a function of nickel content [56].

In applications in which there is a considerable danger of stress corrosion cracking, steels that either has low or high nickel content should be selected. The choice could be either a ferritic or ferritic-austenitic steel or a high alloyed austenitic steel or nickel-base alloy. Although about 40% nickel is necessary to achieve immunity to chloride-induced stress corrosion cracking, the 20-30% nickel in steel grades such as 654 SMO, 254 SMO, 904L and A 28 (commonly known by the Sandviktrade name SANICRO 28) is often sufficient in practice. In this context, it should, however, be noted that nickel content is not the only factor that governs resistance to stress corrosion cracking the entire composition of the alloy is important. Molybdenum has been found to have a considerable effect on

resistance to stress corrosion cracking. However, more than 4% molybdenum is required to obtain a significant effect, as is apparent from a comparison of 904L and 254 SMO in Figure 2. 11. Selecting stainless steel for service in an environment that can cause stress corrosion cracking cannot just be done on the basis of nickel content. High alloy austenitic stainless steels have a very high resistance to chloride stress corrosion cracking in contrast to the lower alloyed grades of this category. For 654 SMO 100% of Rp0.2 was the highest stress level tested. The threshold stress is above that level in this test [56].

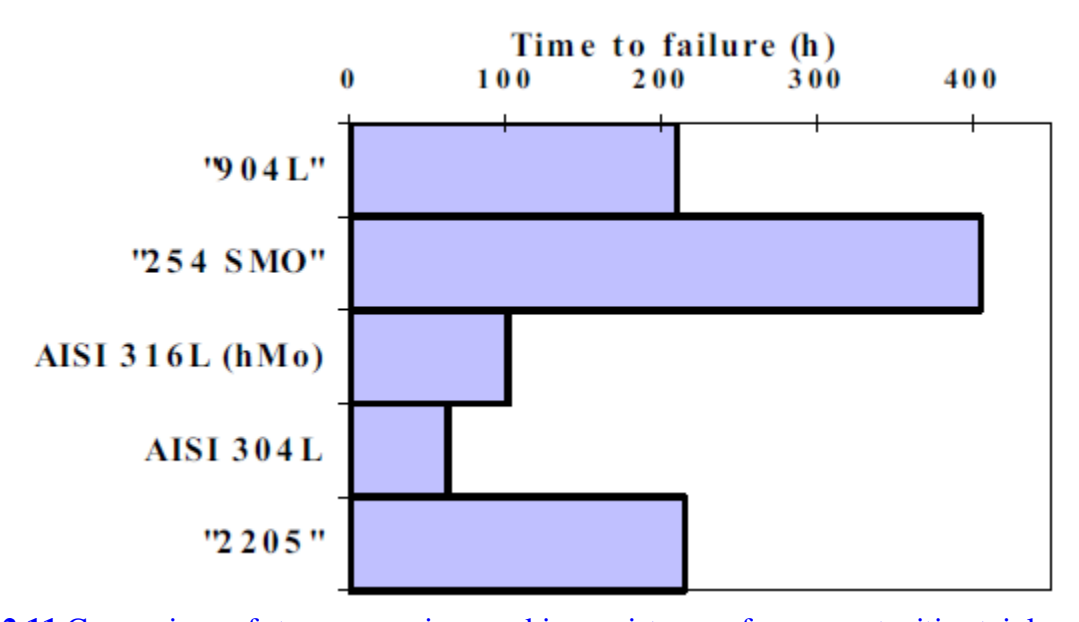


Figure 2.11 Comparison of stress corrosion cracking resistance of some austenitic stainless steels, Drop evaporation method testing with loading to 0.9 x Rp0.2.[56]

2.3 Stress corrosion cracking (SCC) of austenitic stainless steel welds

Austenitic SS are widely used in industries, primarily due to its strength, ease of welding and forming. However, welding also results in inhomogeneous microstructures and high magnitude of tensile residual stresses [23]. Viswanathan *et al.*[57] reported the effects of delta ferrite, carbon content and post weld heat treatment on the stress corrosion susceptibility of AISI Types 308, 309 and 316 stainless steel surface welds in high-temperature water. Kumar *et al.* [58] reported the stress corrosion cracking susceptibility of super 304H parent metal and gas tungsten arc (GTA) welded joints. The welded joints were studied by constant load tests in 45 % boiling MgCl₂ solution. Stress corrosion cracking resistance of super 304H stainless steel was shown to deteriorate by gas tungsten arc welding (GTA) welding due to the formation of susceptible microstructure in the HAZ of the weld joint and the residual stresses. Rapid thermal cycling induced residual stresses in austenitic SS

during welding. The SCC resistance of the welds depends on the δ -ferrite content, its distribution and its morphology were reported by Singh *et al.* [59]. A continuous network of δ -ferrite leads to SCC of SS welds as it forms a continuous path for crack propagation. It was also found that Mo improves the stress corrosion cracking resistance of welds as it strengthens the oxide film and provides enhanced resistance for pitting corrosion [38].

2.4 Welding of austenitic stainless steels

The two basic methods for welding stainless steels are fusion welding and resistance welding. In fusion welding, the heat is produce between the carbon or metal electrode and the weld material. One end of the power supply connection is given to the electrode and other end is given to the weld material. In resistance weld, the joining takes place due to heat and pressure [28]. Heat is produced by the resistance to the flow of electrical current, which passes through the parts to be welded and pressure is applied through the electrodes. Figure 2.12 shows the different types of welding processes.

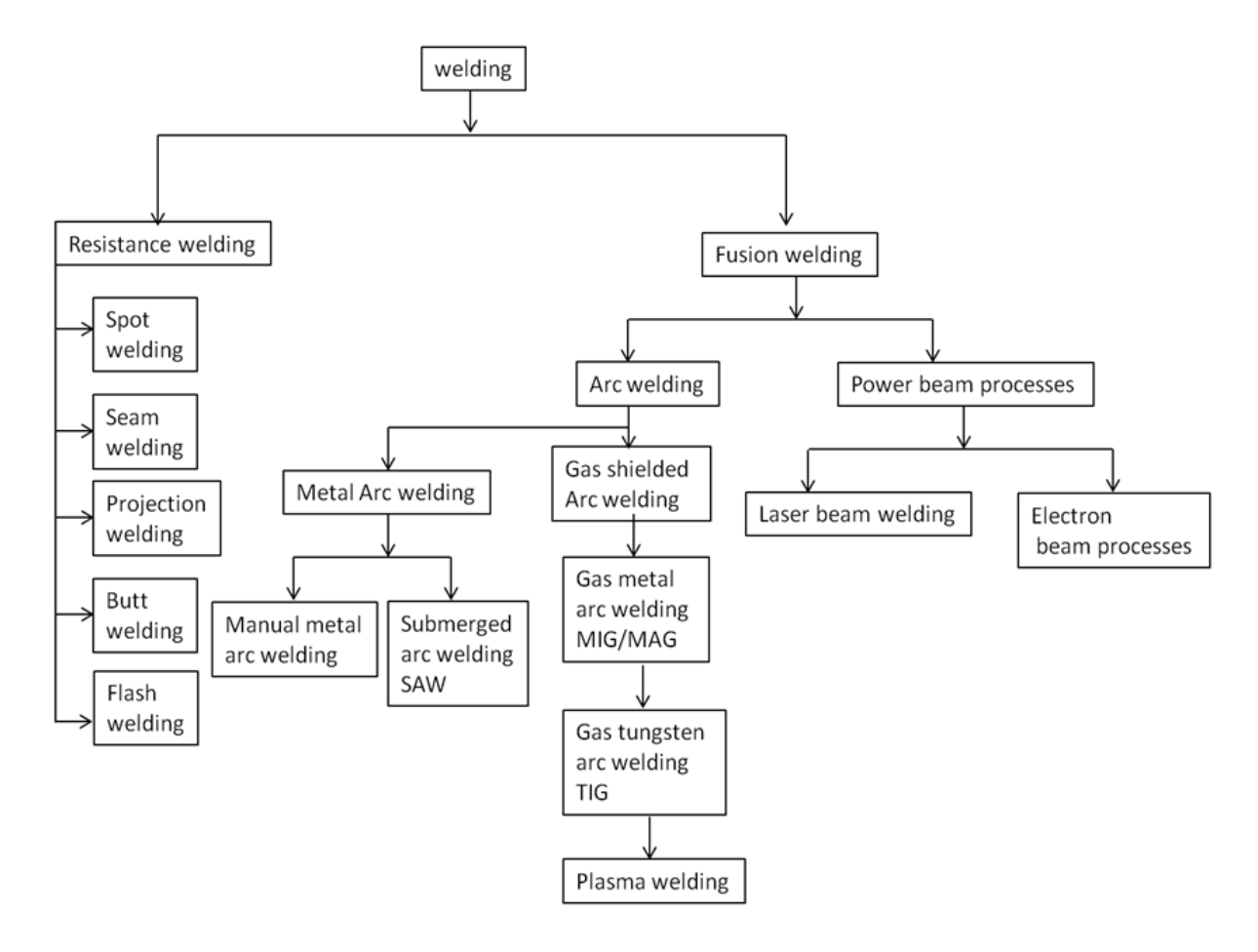


Figure 2.12: Different types of welding processes used for welding stainless steels

2.4.1 LASER welding

Laser beam welding (LBW) is used to join multiple pieces of metal through the use of a laser. Laser welding has several advantages compared to conventional arc welding processes. The major advantages are high welding speed and low heat-affected zone. LBW has a wide range of applications in various industrial sectors including aerospace, microelectronics, medical, automotive, optoelectronics, Microsystems etc. In laser welding, the cooling rate is very high, around 1000-10,000 °C/s [60]. Fast cooling rate results prevent the occurrence of sensitization in the weld zone, and also brittle phase like sigma phases do not exist which are the cause of decreases in ductility. High cooling rate also influences to attain very fine-grained microstructure of the weld. Batahgy et al. [60] reported the variable involved in the laser beam welding including laser power, welding speed, and type of shielding gas, either of which may have important effects on the weld pool. The penetration depth increased drastically with increase in the laser power. Further, laser power has a less influence on both the weld profile and HAZ width. A lower welding speed results in bigger fusion zone and consequently a decrease in depth/width ratio leading to unacceptable weld profile. The depth/width ratio increases sharply with the increase in the welding speed. However, at a high welding speed, attenuation of beam energy by plasma is less significant [61]. Moreover, a high welding speed gives rise to high magnitude of tensile residual stresses in the weld due to the fast rate of cooling.

2.4.2 LASER hybrid arc welding

LASER Hybrid arc welding was first developed by Eboo and Steen in the late 1970s [62,64]. Figure 2.13 shows the schematic of hybrid laser-arc welding. Hybrid laser-arc welding is a combined process of gas metal arc welding and laser beam welding. However, this has limited research work on the process, because of the cost and availability of high-power welding lasers. Research work by Matsuda *et al.* [63] showed that the use of laser hybrid process can increase welding speeds with minimum surface defects and improved penetration [61]. Tadamall *et al* [65] have studied the effect of process variables and the performance of variables such as pulse overlap, duty cycle, bead diameter, and energy density. Experiments were conducted on different welding speeds in the range from 2 to 10 mm/s on 304 L stainless steel sheet with a laser power of 300–3500 W. It was concluded that laser power had the maximum influence on weld pool geometry than the other parameters of laser welding.

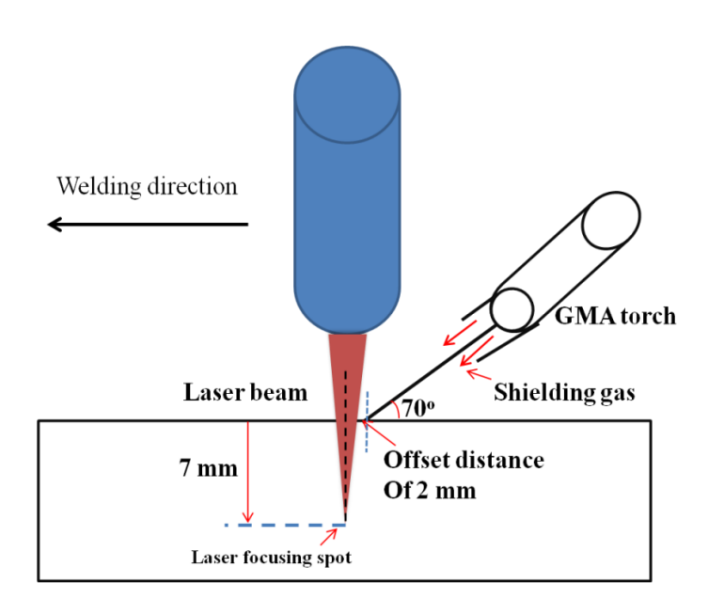


Figure 2.13 Schematic of LASER Hybrid arc welding

2.4.3 Metal inert gas welding (MIG)

The basic principle of the MIG welding process is when an electrical arc is established and maintained between a base material and a continuous feed wire electrode [28]. Both the arc and the weld pool are protected from atmospheric contamination by using an inert gas. Gas Metal Arc Welding is widely used in industries because it gives high production rates, easiness of automation and ability to obtain high-quality welds with many metals. In arc welding process parameters such as current, voltage, polarity, electrode diameter, shielding gas composition and flow rate have a great influence to perform successful welds. Argon gas is used as the basic shielding gas, but Helium can be added to increase penetration and fluidity of the weld pool. Also, small additions of oxygen or carbon dioxide are usually needed to stabilize the arc, improve fluidity and bead quality. Towards the welding of austenitic stainless steels, the addition of small amounts of hydrogen gas also gives similar results. Moreover, much stronger effects are observed when the helium gas is used instead. Adding of 2-5 % of hydrogen to argon gas allows to obtain welding speeds comparable to pure argon. The AISI 304 and 316 sheets have shown good weldability utilizing the electric arc under different compositions of the shielding gas (pure Ar or Ar plus He, H₂, CO₂ or O₂) [66]. Good

penetration, right weld bead profile, and absence of macroscopic defects are the characteristic features of this technique.

2.4.4 Spot Welding (SW)

Spot welding is a process of joining, in which two or more metal sheets are joined together through fusion at a certain point [67]. The schematic of electrical resistance spot welding technique is shown in Figure 2.14. In spot welding, coalescence is produced by the heat obtained from resistance to the flow of electric current through the work-piece held together under pressure by electrodes. The size and shape of the welds are limited primarily by the size and contour of the electrodes. In this process, two electrodes are used which are made of copper alloys, and they are generally water cooled. The electrodes are brought together with the work-piece held between the electrodes by a mechanical force which is supplied by foot, air, hydraulic, or a motor operated. All the stainless steels that are non-hardenable are readily spot welded.

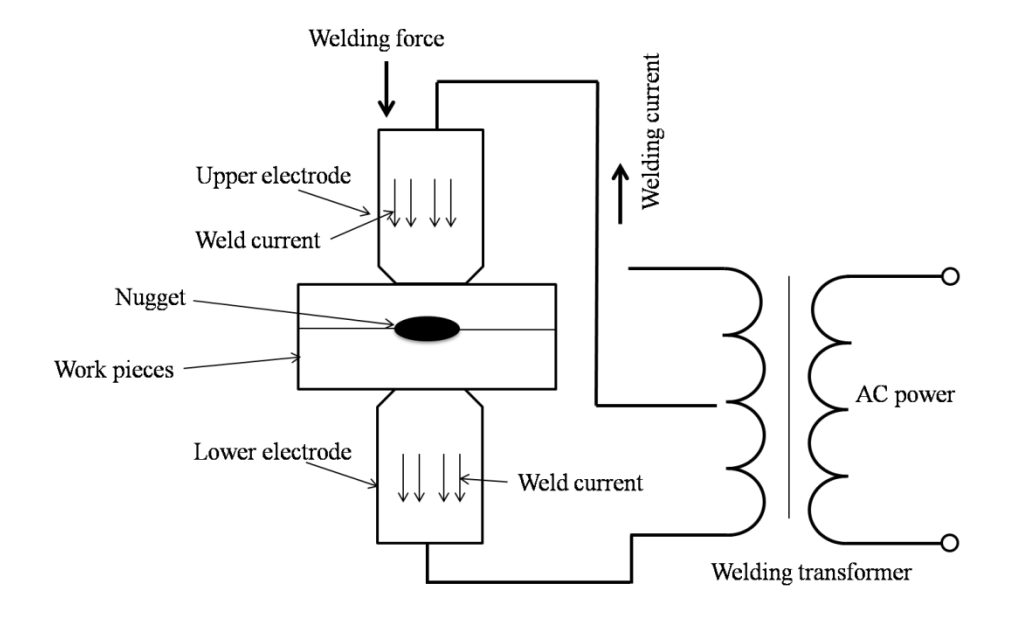


Figure 2.14 Schematic of Electrical Resistance Spot Welding Technique

The hardness of spot welded zone being greater than that of the un-welded zone was reported by Charde *et al.*[68] Studies by Jamaludin *et al.*[69] showed that with an increase in the weld current increases the nugget size without affecting the hardness value. Somervuori *et al.* [70] reported the formation of colored oxide films with heat tints around the spot welds reduces the pitting corrosion

resistance of the SS. The Cr depletion takes place in this region which causes the lower pitting corrosion and also showed that the weld is prone to SCC because there are high residual tensile stresses in the radial direction around the spot welds [71]. These residual stresses are high enough to cause stress corrosion cracking in aggressive chloride containing environments to austenitic SS without any external load. Also, the pitting corrosion susceptibility may be affected by the high residual stresses around the spot welds.

2.5 Residual stresses generated by different techniques

The residual stresses generated in the material would be of either tensile or compressive in nature based on the fabrication techniques and or surface finishing. Fabrication techniques like welding will generate tensile residual stress to components. The welded structures heated rapidly up to the melting temperature and followed by rapid cooling that causes microstructural and property alteration which leads to residual stress. While surface treatments such as machining, grinding and turning operations can lead to the generation of tensile residual stress to components and shot peening, laser shot peening (LSP) give the compressive residual stress [16-22]. Stress corrosion cracking can only occur in the presence of tensile stresses. The stress to which stainless steel may be subjected without cracking is different for different steel grades. [56] An example of the threshold stresses for different steel grades under severe evaporative conditions is given in Figure 2.15.

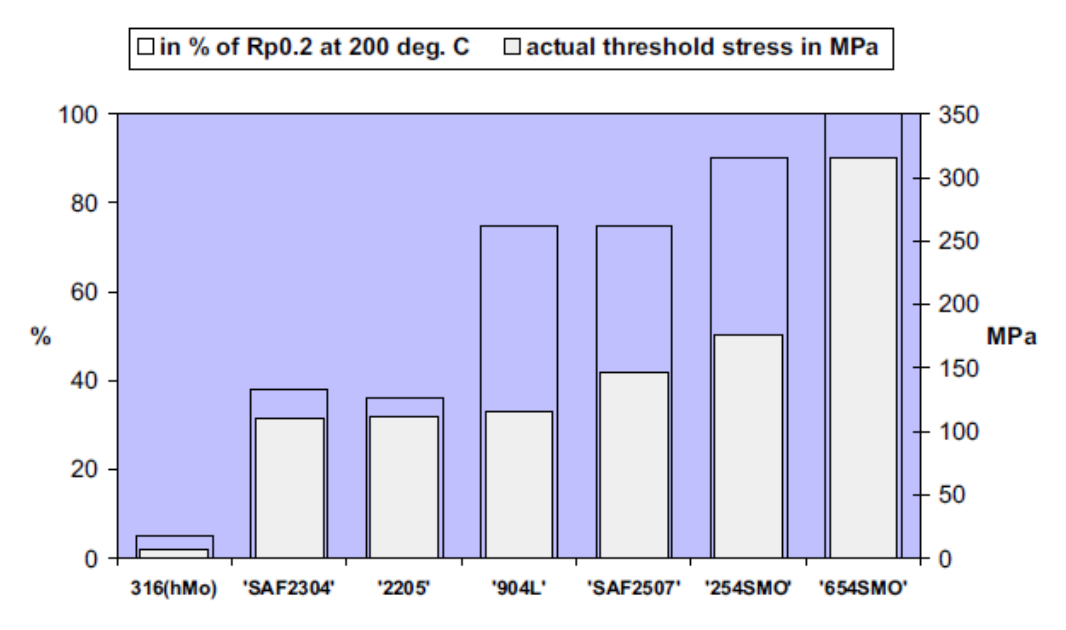


Figure 2.15 Threshold stresses for chloride stress corrosion cracking under severe evaporative conditions. [56]

2.5.1 Residual stress generated during welding

Residual stress generated during welding was tensile in nature because of its thermal expansion and contraction at HAZ in welded structures. Residual stresses are minimized by appropriate selection of materials, welding process/parameters, structural geometry, and fabrication sequences. Residual stresses are reduced by various special welding techniques which include low-stress non-distortion welding (LSND), last pass heat sink welding (LPHSW) and inter-run peening.

2.5.2 Residual stress generated during surface finishing

The surface finishing techniques like machining, grinding and turning induces the tensile residual stress in the material. Zhang *et al* [72] reported the presence of tensile residual stresses due to the machining process. The surface after machining has a great influence on the initiation of SCC microcracks. Larger residual stresses can result in higher crack initiation and micro-crack density. Microcracks are initiated only when the residual stress levels are above the critical level. The critical stress of 316 austenite stainless steel is 190 MPa. Milling, grinding, and turning also induces high magnitude of tensile residual stresses in 304L SS as reported by Ghosh *et.al.* [73]. Laser shock peening (LSP) [11], low plasticity burnishing (LPB), shot peening and shot blasting, etc. are used to induce compressive stresses on the surface. However, these have some shortcomings such as the development of high plastic strain on the surface by shot peening, cost effectiveness of Laser peening etc. Sunil *et.al* [22] showed that buffing operation can be applied to induce a high magnitude of compressive residual stresses on the surface of 304L SS. However, the application of buffing operation to improve the SCC resistance of welds has not been reported in the literature.

2.6 Solar thermal power plants

Solar thermal power plants involve technology for harnessing solar energy to generate electrical or thermal energy for commercial and residential usage [74]. Configuration of concentrated solar power (CSP) plant can be divided into three different designs which are given as follows:

- Parabolic trough reflectors,
- Power towers, and
- Dish-Stirling systems.

A solar thermal power plant which produces the solar energy with the help of parabolic reflector mirrors have a tracking system throughout the day to focus the sun's rays and the receivers/

collectors which collect the heat energy that heats the thermionic fluid flowing through the tubes. This heat energy is sent through heat exchangers tubes to boil water in a steam turbine generator to produce electricity. Operating temperatures is ~ 400° C because of the parabolic troughs can focus the sunlight from 30 to 100 times to its normal intensity on the receiver tube, wherein, the parabolic trough reflectors and power tower designs are most widely used. Schematic of the parabolic trough design is shown in Figure 2.16. Parabolic trough collectors which have three main functional units 1) concentrator 2) parabolic shaped mirror and 3) a tracking device. In the absorber tube, the concentrated solar radiation is transformed into solar energy. If the angle of incidence is equal to the angle of reflections the parabolic collectors can collect the vertically incident rays to the optical axis which is concentrated on the focal point and a concentrator which has a tracking device which continuously tracks the path of the sunlight in order to prevent scattering of rays.

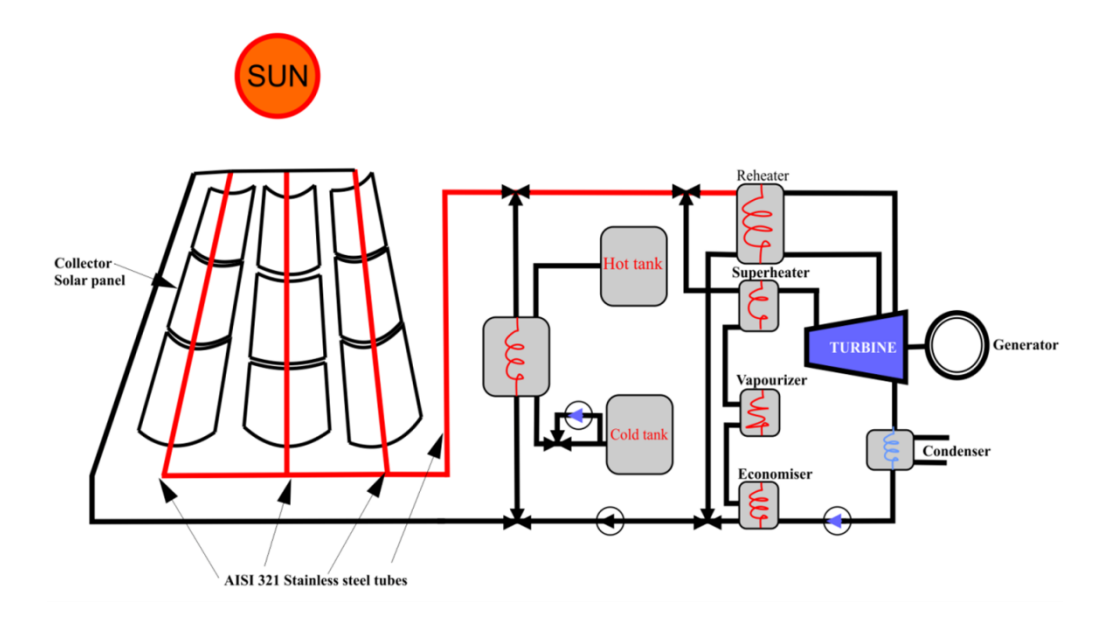


Figure 2.16 Schematic of the concentrated solar thermal power plant (Parabolic trough reflectors)

2.6.1 Solar thermal collectors for solar industrial process heat applications

There are different types of solar collectors shown in Figure 2.17, but all of them are constructed with the same basic premise in mind. In general, there is some material that is used to collect and focus energy from the Sun and use it to heat water. The simplest of these devices uses a black material surrounding pipes that water flows through. [75] The black material absorbs the solar radiation very

well, and as the material heats up the water it surrounds. This is a very simple design, but collectors can get very complex. Absorber plates can be used if a high temperature increase isn't necessary, but generally devices that use reflective materials to focus sunlight result in a greater temperature increase.

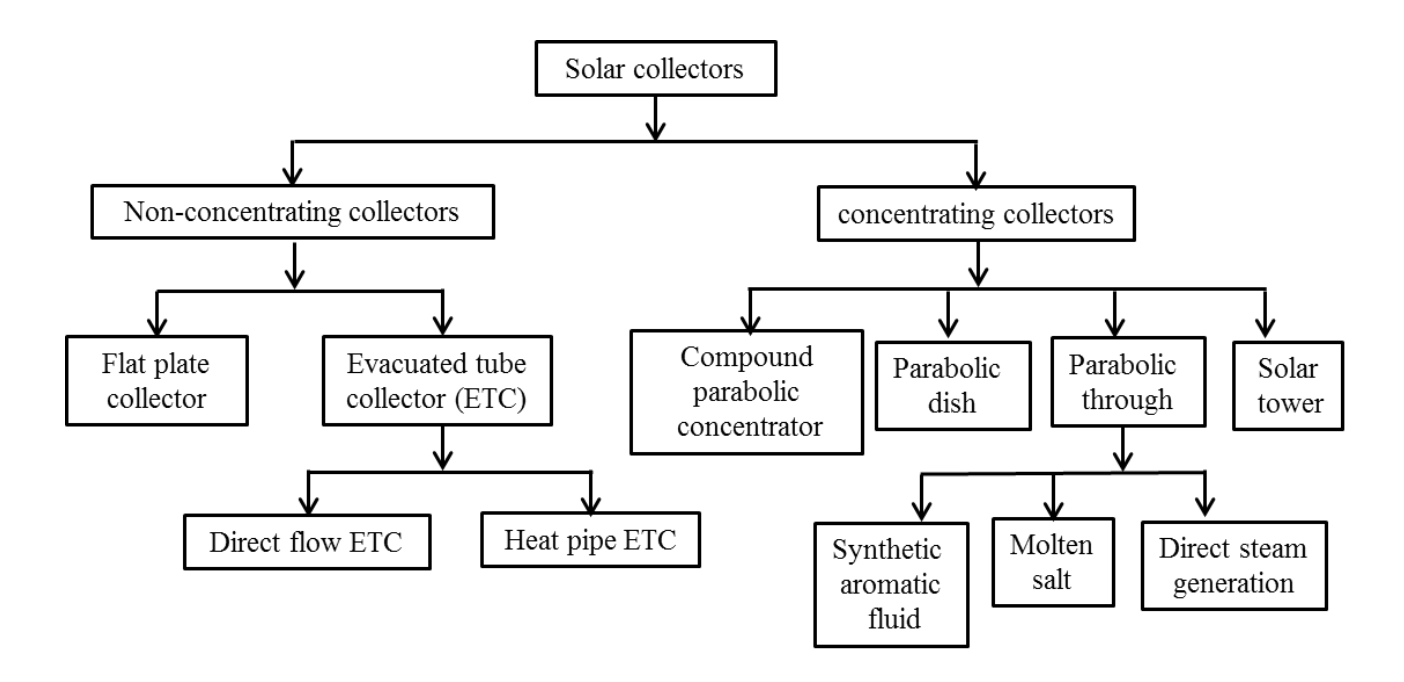


Figure 2.17 Different types of solar collectors

2.6.2Solar collector

Solar energy is converted into thermal energy using a special kind of heat exchanger known as a solar collector. Solar collectors can be classified into two general categories: (a) non-concentrating and (b) concentrating solar collectors.[74-76]

2.6.2.1 Non-concentrating type solar collectors

The collector area (the area that intercepts the solar radiation) is the same as the absorber area (the area that absorbs the radiation) [74]. Flat plate collectors (FPC) and evacuated tube collectors (ETC) are non-concentrating type collectors. These collectors are mainly designed for solar hot water and industrial process heat applications which require energy delivery at temperatures in the range of 60-250°C. These collectors use both diffuse and beam solar radiation and do not require tracking of the

sun. They are mechanically simpler than concentrating type solar collectors and require less maintenance [74].

2.6.2.1.1 Flat plate solar water collector

The schematic diagram of a typical flat-plate solar collector is shown in Figure 2 18. A flat-plate collector consists of (a) an absorber, (b) a transparent cover (c) a heat-transport fluid (water, air, etc.) (d) Housing or casing and (e) insulation. The absorber consists of a solar selective coating deposited on top of a thin absorber sheet of steel or copper. A low iron solar safety glass is used as a transparent cover. Solar radiation enters the collector through the transparent cover and reaches the absorber. The absorber converts the absorbed radiation into thermal energy. In the case of a flat-plate solar water collector, good thermal conductivity is required to transfer the collected heat from the absorber sheet to the absorber pipes. The housing ensures safety and protects the absorber and insulation from the environmental impacts. Generally, rock wool or mineral wool is used as an insulation material in order to reduce the thermal losses on the back side of the absorber [75]. The efficiency of standard liquid flat-plate collectors can be improved by reducing the optical and thermal losses. This can be achieved by (a) multiple glazing with anti-reflective glass, (b) filling a hermetically sealed flat plate collector with a noble gas or (c) evacuating a hermetically sealed flat plate collector. These improved flat plate collectors can be used for solar industrial process heat (SHIP) applications.

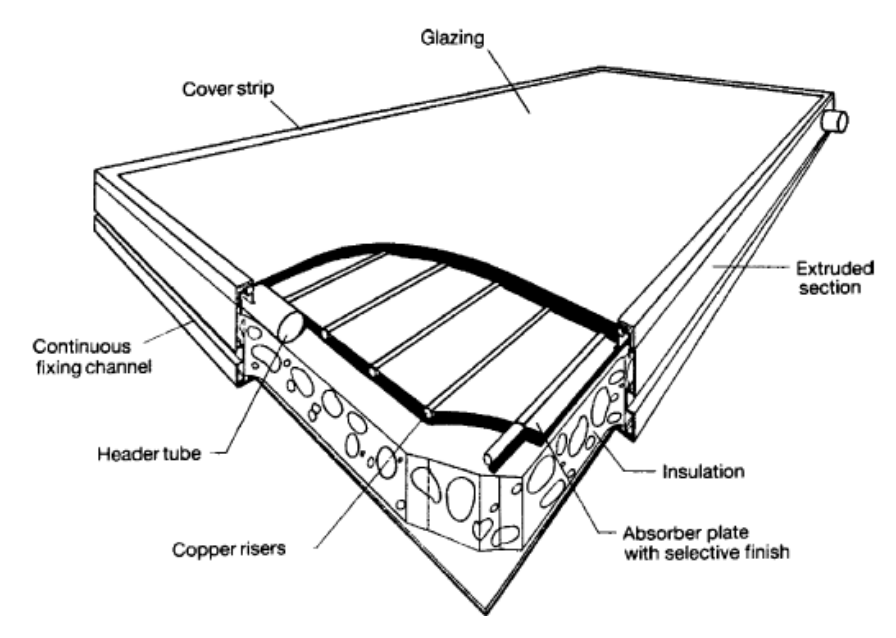


Figure 2.18 Schematic diagram of a flat-plate collector [75]

In recent years, flat plate collectors are being replaced by evacuated tube collectors since they offer certain advantages. Evacuated tube collectors (ETCs) have multiple evacuated glass tubes which heat up solar absorbers and ultimately the working fluid (water or an antifreeze – typically propylene glycol) for domestic hot water or space heating applications. The vacuum within the [75] evacuated tubes reduces convection and conduction heat losses, allowing them to reach considerably higher temperatures than most flat-plate collectors.

2.6.2.1.2 Evacuated tube collector

Figure 2.19 shows the schematic diagram of an evacuated tube collector. Each evacuated tube consists of two glass tubes made from extremely strong borosilicate glass with high chemical and thermal shock resistance. The outer tube is transparent allowing light rays to pass through with minimal reflection. The outer side of the inner tube is coated with a sputtered solar selective coating which exhibits excellent solar absorbance and low thermal emittance. The top ends of the two tubes are fused together and the air contained in the annular space between the two layers of glass is evacuated to eliminate conductive and convective heat loss. The top end of these parallel tubes is fitted to the inner storage tank. In the process of creating vacuum, a barium getter is inserted into the base of the outer glass tube. The inner glass tube is then inserted into the outer tube with the getter centering the inner glass tube. The glass tubes are heated to a high temperature and vacuum is created. The two glass tubes are then fused together at the open end. The barium getter also serves another purpose. When the glass tubes are heated, before the ends are fused together the barium getter also becomes very hot and a pure layer of barium is coated at the bottom of the tube which will look like a chrome plate on the inside of the outer glass tube. When the glass is fractured or broken, the shiny chrome changes to a milky color, thus, making it easy to identify the vacuum loss in the particular glass tube. The advantage of an evacuated tube collector when compared to a flatplate collector is that the constant profile of the round evacuated tubes is always perpendicular to the sun's rays. Therefore the energy absorbed is approximately constant over the course of a day. Evacuated tube collectors can be classified into two main groups (a) direct flow evacuated tube collectors and (b) heat pipe evacuated tube collectors [77-78].

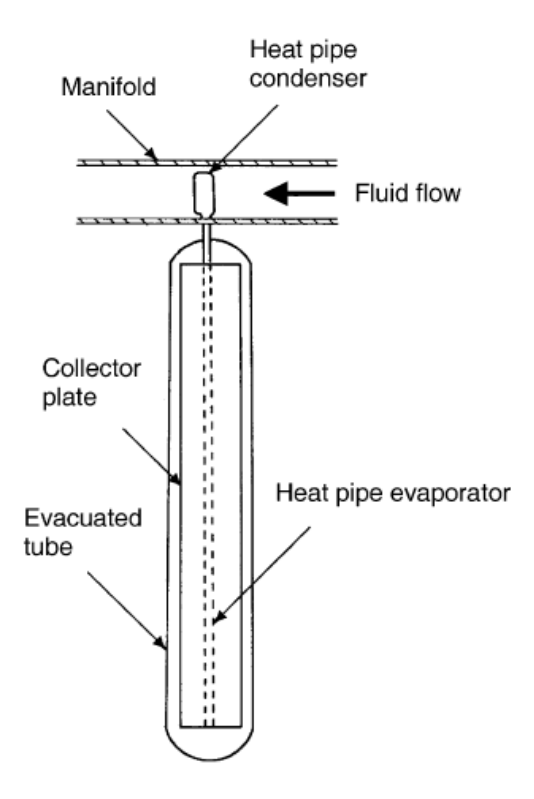


Figure 2.19Schematic diagram of an evacuated tube collector. [78]

2.6.2.1.3 Direct flow evacuated tube collector

In this type of collector, the whole interior of a glass tube is evacuated. The flat or curved absorber, as well as fluid inlet and fluid outlet pipes, are placed inside the evacuated tube. The absorber is coated with a spectrally selective coating. Single evacuated tubes often have diameters between 70 and 100 mm [77]. Direct flow evacuated tube collector has different configurations such as separate tubes for fluid inlet and outlet concentric inlet and outlet i.e., concentric pipe configuration in which the fluid inlet is copper and the outlet is glass and Sydney tube two glass tubes fused together and the space in between is evacuated.

2.6.2.1.4 Heat pipe evacuated tube collector

Figure 2.20 shows the schematic diagram of a heat-pipe evacuated tube collector. The heat pipe is hollow with low pressure inside. A heat pipe evacuated tube collector uses alcohol or water with some special additives in vacuum to absorb solar energy. Due to the vacuum, the alcohol or water will evaporate at a low temperature of 25°C to form vapor. This vapor rises up the collector tube to the heat exchanger where heat transfer to the solar fluid takes place. Subsequently, the vapor

condenses back to liquid and flows back down the collector tube. Therefore, heat pipe evacuated tubes are installed with a tilt of at least 25°. There are two types of heat pipe evacuated tube collector: (a) heat exchanger extends directly into the manifold (wet connection) and (b) heat exchanger connected to the manifold by a heat-conducting material (dry connection). In a dry connection collector, the condenser completely surrounds the collector tube. This provides good heat transfer between the tube and the heat exchanger and allows tubes to be replaced without the need to drain the solar fluid. In a wet connection collector, the tube is submerged in the heat transfer fluid. Therefore, if a tube needs to be replaced then the system must be drained. The major difference between the heat pipe and direct flow evacuated tube collector is that, in heat pipe ETC, the heat transfer fluid is not directly connected to the solar loop.[79]

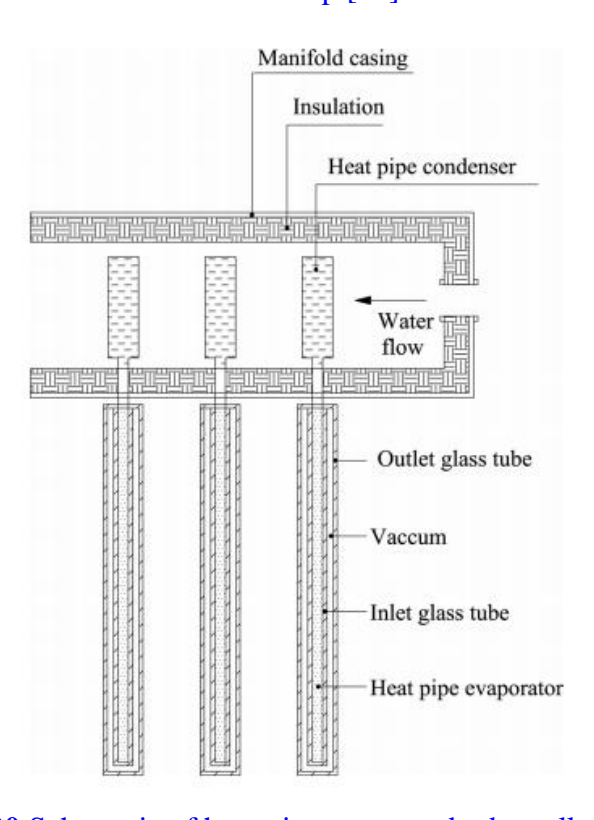


Figure 2.20 Schematic of heat pipe evacuated tube collector [79]

2.6.2.2 Concentrating type solar collectors

In the concentrating type solar collector, various types of mirrors, reflectors or concentrators are used to concentrate the solar energy and they provide higher temperatures (~ 400–1000°C) than non-concentrating type collectors. Compound parabolic concentrator (CPC), central receiver or solar tower, parabolic trough collector and parabolic dish collectors are concentrating type collectors and

are known as concentrated solar power (CSP) systems. The concentration ratio (i.e., ratio of the area of the aperture to the area of the receiver) varies from less than unity to high values of the order of 105. The concentrating type collectors are classified into three types: (a) non-imaging (b) line focusing and (c) point focusing collectors. Non-imaging collectors have a low concentration ratio; line focusing collectors have intermediate concentration ratio and point focusing collectors have high concentration ratio. The CPC collector is a non-imaging concentrating collector. Whereas, parabolic trough and central receiver are lines focusing and point focusing collectors respectively. These CSP systems are mainly used for solar thermal power generation.

2.6.2.2.1 Compound parabolic concentrator (CPC)

CPC collector uses a compound parabolic concentrator (non-imaging type) to concentrate solar radiation on an absorber. [76] CPC collectors admit a greater amount of light and need less accurate tracking when compared to parabolic trough collector (PTC). Therefore, they bridge the gap between the low-temperature flat-plate collectors (T < 80°C) and the high-temperature focusing concentrators (T> 400°C). For solar thermal power generation, it is desirable to deliver energy at temperatures higher than those of evacuated tube (non-concentrated) and CPC collectors. A concentrating type collector can be used for high temperature applications such as to produce steam for thermal power generation. Solar thermal power systems are also known as concentrating solar power systems use concentrated solar radiation as a high-temperature energy source to produce electricity using the thermal route. Direct solar radiation can be concentrated and collected by a range of CSP technologies to provide medium to high-temperature heat.

2.6.2.2.2 Central receiver (or) solar tower

A circular array of heliostats (large individually tracking mirrors) is used to concentrate sunlight on to a central receiver mounted on the top of a tower. A heat-transfer medium in the central receiver absorbs the highly concentrated radiation reflected by the heliostats and converts it into thermal energy which is subsequently used for the generation of superheated steam for turbine operation. [76]

2.6.2.2.3 Parabolic dish collector

A parabolic dish-shaped reflector is used to concentrate sunlight on to a receiver located at the focal point of the dish. The concentrated beam radiation is absorbed into the receiver to heat a fluid or gas (air) to approximately 750°C. This fluid or gas is then used to generate electricity through a small piston or Stirling engine or a micro turbine, attached to the receiver.

2.6.2.2.4 Parabolic trough collector

Parabolic trough systems use trough-shaped mirror reflectors to concentrate sunlight on to the receiver tubes through which a thermal transfer fluid is heated to roughly 400°C and then used to produce superheated steam. The heat is then used to operate a conventional power cycle, for example, through a steam turbine or a Stirling engine [77-82]. The primary components of a trough system are:

- ❖ Parabolic trough concentrator: The parabolic trough concentrator reflects direct solar radiation onto a receiver located at the parabola's focal point. The reflective surface, often 17 silver or aluminum films is deposited on some type of rigid support. Currently, the most commonly used support structures are metallic, glass or plastic tubes.
- ❖ Absorber tube: The absorber tube is one of the most important components of a trough system. The absorber tube is made of two concentric tubes that lie along the parabolic trough's focal point. The outer tube (made of glass) is separated from the inner tube (made of metal) by a vacuum layer. This reduces heat loss and increases overall efficiency. A working fluid is circulated through inner tube and absorbs solar radiation energy as heat.
- ❖ Working fluid: The working fluid varies depending on the trough technology. For lower temperature applications (less than 200°C), demineralized water with an ethylene-glycol mixture is used as the working fluid. For higher temperatures, (above 200° C 450° C) synthetic aromatic oil is often used as the working fluid. Direct steam generation (DSG) in parabolic trough collectors eliminates the use of heat exchangers and expensive heat transfer fluids. Therefore, it is a promising option to improve efficiency and reduce the operating costs of parabolic trough power plants. Newer technologies use molten salts as the working fluid.
- Solar tracking system: A parabolic trough solar power plant fields consist of a large, modular array of single-axis tracking parabolic trough solar collectors. Many parallel rows of these solar collectors span across the solar field, usually aligned on a north-south horizontal axis.

❖ Support structure: The entire parabolic trough system is supported by a rigid metallic support structure. The structure supports the mirrors and receivers and maintains their optical alignment. It allows the collector to rotate so that the mirrors and receivers can track the sun. Generally, the support structures are made from galvanized steel or extruded aluminum. Improving the properties of the solar selective coating on the receiver and increasing the solar field operating temperature above 400°C can improve the efficiency of a parabolic trough solar power plant and reduce the cost of solar electricity. In order to achieve this, new efficient spectrally selective coatings are needed which have high absorbance in the wavelength range of ∼0.3-2.5 m and low emittance in the infrared region, at higher operating temperatures (both in air and vacuum).

2.6.3 Various materials used in solar thermal power plants

Metals with high thermal conductivity, such as copper or aluminum, cannot be used for this application because of their poor mechanical properties at high operating temperatures and high pressures are required for solar thermal power application, hence steels are commonly used. Carbon and low-alloyed stainless steels have better thermal conductivity than high alloyed austenitic stainless steel, and they are cheaper but these steels have lower corrosion resistance than austenitic stainless steel. Carbon steel ASTM 335 grade P22 has been used in DISS facility in Plata forma Solar de Almeria(PSA) in Spain, with direct steam generation (DSG) with water as heat transfer fluid (HTF), and corrosion problems were observed due to erosion and cavitation produced by a biphasic flow. Now, in this technology, producers are using AISI 316 austenitic stainless steel to guarantee mechanical robustness against high operating pressures and radial temperature gradients produced by a biphasic flow. Receiver thickness increases dependently on the maximum operative pressure (above 100 bar), and it leads to a thicker tube (>4.5 mm) that directly reflects into an effective cost increase of the technology [83-84]. When synthetic oil and organics such as biphenyl/diphenyl oxide systems are used as HTF, austenitic AISI 321L stainless steel is the usual option due to its lower hydrogen permeation in comparison with other austenitic stainless steel. Hydrogen diffusion is the major drawback of this technology because of HTF thermal degradation, and high hydrogen partial pressures are achieved in vacuum annulus. Typical wall thickness employed is 2 mm. Molten salt receiver tubes commonly use a mixture of NaNO₃ (60 wt. %), KNO₃ (40 wt. %) salts (solar salt) or a mixture of NaNO3 (7 wt. %), KNO3 (53 wt. %), NaNO2 (40 wt. %) salts [84]. There are several reports in the literature on corrosion issues of these molten salts with metallic alloys, and it was found that the nickel alloys with 15-20% chromium content performed the

best corrosion resistance, whereas iron alloys with low or almost zero nickel content showed poor corrosion resistance at high temperatures. Hence, AISI 321 stainless steels are commonly used in molten salt receiver tubes.

2.6.4 Thermionic fluids properties and various degradation mechanisms

Fused salts have a high degree of importance in chemical and thermal industry. Many types of fused salts are used as heat paths in the heat treatment of metals and alloys. Fused salts are also used in the nuclear industry as well as the thermal storage applications as a heat transfer mediums such as in concentrated solar power plants. For applications where pumps, pipes, and heat exchanges are in contact with the molten salts, the need to study the corrosion induced by these fused heat transfer fluids began. Solar salt is a heat transfer fluid used in solar- thermal industry. It has acquired its distinctive name because of its use in concentrated solar power plants as a heat transfer medium in the form of a fused liquid salt. It is also known commercially as (HITEC). The chemical composition of solar salt is 53 wt. % potassium nitrate (KNO₃), 40 wt. % sodium nitrite (NaNO₂), and 7 wt. % sodium nitrate (NaNO₃) [84]. The attractive thermal properties of solar salt make it a candidate for many heat transport applications such as the heat transfer medium in concentrated solar power (CSP). The ternary solar salt melts at 142°C. This low melting point allows liquidation and circulation of the heat transfer fluid with minimum solar energy. In addition, solar salt has a high thermal conductivity, high heat transfer coefficient, high heat capacity, high thermal stability, low cost, and low vapor pressure (Coastal chemical). Those properties provide efficiency in the extraction and transport of solar thermal energy. However, the extent of corrosion that solar salt may induce on the structural material is not fully investigated for an alloy or metal in contact with a fused salt, the degree of attack can progress by two mechanisms. First, the metal or its reaction products can be soluble in the salt. If so, a continuous dissolution occurs with a linear loss of dimensions with time. Secondly, the metal can be oxidized by the fused salt. Then, corrosion products that are insoluble form, and become a barrier against further oxidation of the base metal, known as passivation effect. Therefore, the degree of strength of an alloy system to resist corrosion induced by a fused salt is estimated by the ability to form dense, well bonded, and insoluble corrosion products with slow growth kinetics of the corrosion layers. According to Sequeira et al,[85] the degree of corrosivity of a fused salt can be estimated. Salts that contain high concentrations of oxidizing agents are corrosive to metals and alloys. The oxidizing nature of molten nitrite and nitrate salts are known to be high due to oxidizing species such as NO₂ and NO₃ Slusser et al., [86] In addition, air can play

a major role in accelerating oxidation in open systems. Despite being strong oxidizers, molten nitrites and nitrates are very good heat transfer fluids with very desirable thermal properties making them a subject for many corrosion studies. In corrosion related literature, fused nitrates corrosion effects have been studied with multiple types of structural materials including steels and stainless steels. Slusser et al [86] have carried out series of mass loss experiments to assess the corrosion resistance of many Fe- Ni- Cr and Cr- Ni alloys in equimolar sodium- potassium nitrates salt mixture that has a melting point of 220°C. Tests were done in the temperature range (~570°C -705°C) for a test period up to 122 days. Alloy 600 and HASTELLOY N exhibited low corrosion rates of 12 -13 mpy after 14 days. On the contrary, Ni alloy 200 and silicon enriched alloys such as NICROFER 3718 and 330 stainless steel have shown a high corrosion rate that reached 100 mpy. After the test period, the salt solution showed enrichment of chromium. Fernandez e t.al [87] have tested AISI 304,430 stainless steels and a low Cr alloy steel, T22 at 390°C for up to 2000 hours to measure their corrosion rates by gravimetric methods with saline salt mixture (60 wt. % NaNO₃ - 40 wt. % KNO₃) as a potential heat transfer fluid being used in solar- thermal power plants. It was concluded that T22 suffers a high weight gain in comparison to AISI 304 and AISI 430 stainless steels. The result is attributed to the low Cr content in T22 of 2.25 wt. % that led to the formation of porous surface oxide layers allowing the salt to penetrate and cause corrosion of the base alloy. A surface layer of Fe₂O₃ was identified as a corrosion product on top of the compact layer of Fe₃O₄. Bradshaw and Goods et.al [88] from Sandia National Laboratory have exposed coupons of 316 stainless steel to the molten salt mixture of (60 wt.% NaNO₃- 40 wt.% KNO₃) at test temperatures of 630°C and 650°C under a cover gas of oxygen in a sealed crucible. As per weight loss approach, 316 stainless steel was found to follow a parabolic growth kinetic up to 630°C. At 650°C, the kinetic changed to a linear behavior and it was attributed to the breakdown of the surface corrosion layers that were found to be temperature dependent at 630°C, it was found that magnetite has formed on top of a layer of iron-chromium spinel. While at 650°C, a thick layer of sodium ferrite in addition to spinel formation has been found to be in contact with the molten salt. Kruizenga et al [89] has analyzed the corrosion effects that 316 stainless steel was subjected to as a result of contacting molten nitrates salt mixture (89 wt. % KNO₃- 11 wt.% NaNO₃) that was contained in alumina vessel at a temperature range ~ 350°C – 750°C during a thermal stability experiment. Over an exposure period of about 2000 hours, 316 stainless steel was corroded in the form of pitting. Pits were found to primarily rich in potassium oxide and potassium chromates.

Chapter 3

3.0 Experimental

3.1 Materials

The as-received tubes of AISI 321 stainless steel having a dimension of 3900 mm x 72 mm x 2.8 mm (length x diameter x thickness) were used for the study. These tubes were seam welded by either laser beam welding (LBW) or metal inert gas welding (MIG) and had fixtures spot welded to its surface. These are used in a solar thermal power plant for the transfer of thermic fluid it contains 1.5 mg/kg chloride and A fixture containing Xenon capsules was spot welded on the surface of the tubes at a particular location as shown in Figure 3.2. Table 3.1 gives the composition of the AISI 321 SS tubes which complies with ASTM A 240/A 240M – 04a [90]. And Figure 3.1 shows the SEM microstructure of the AISI 321 stainless steel.

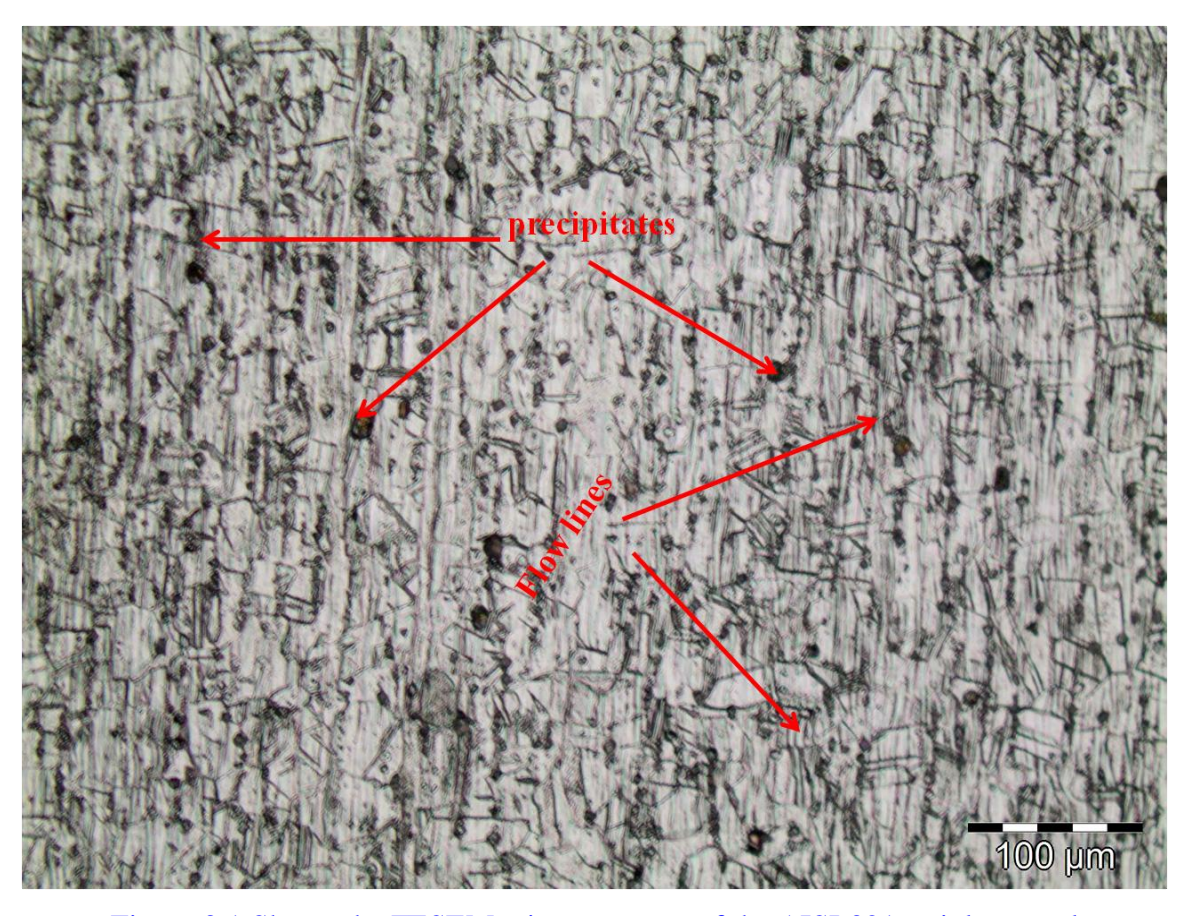


Figure 3.1 Shows the FESEM microstructure of the AISI 321 stainless steel

Material	С	Si	Mn	Cr	Ni	Ti	S	P
SS 321	0.04	0.74	0.95	17.33	9.02	0.32	0.005	0.024
ASTM A 240/A 240M – 04a	0.08 max	0.75 max	2.00 max	17.0– 19.0	9.0– 12.0	0.70 max	0.030 max	0.045 max

Table 3.1: Chemical compositions of base metal AISI 321 stainless steel (wt. %)

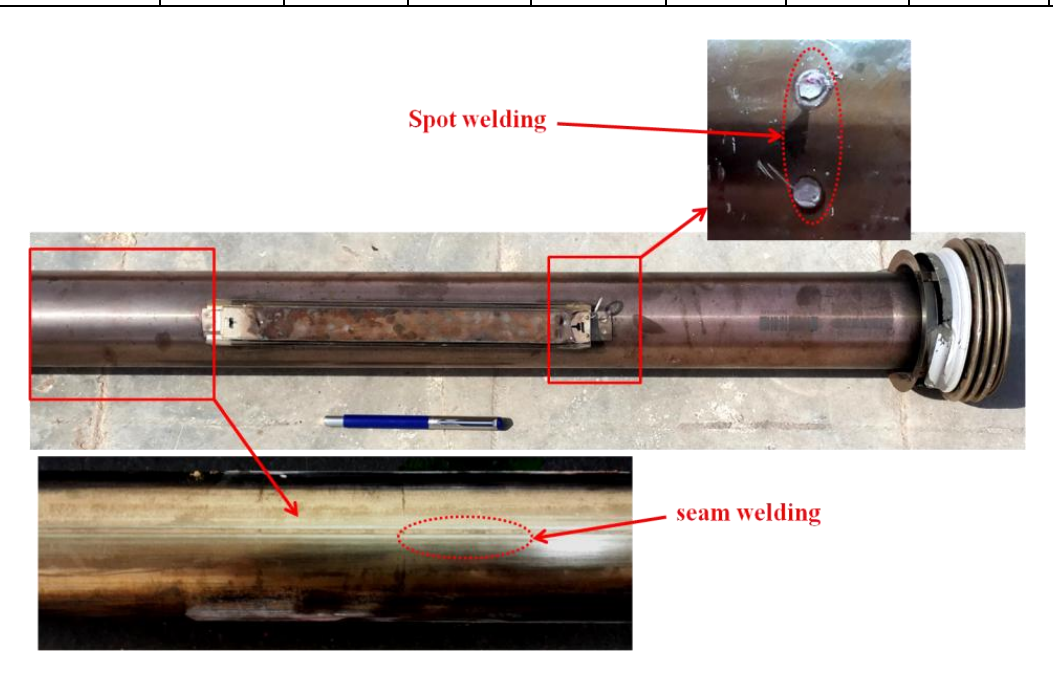


Figure 3.2 AISI 321 SS heat exchanger tube indicating the location of seam weld and spot weld.

3.2 Non-destructive evaluation

The AISI 321 SS heat exchanger tubes were subjected to the dye penetrant test (DPT) to find the presence of any surface defects such as weld defects and hairline cracks. Primarily, the test surface was cleaned to get rid of any impurities that could object the fluid from penetrating. After cleaning, the surface was dried and fluorescent penetrant PMC lumin check FPS-46B was applied. Figure 3.3(a) shows the fluorescent penetrant PMC lumin check FPS-46B and Figure 3.3(b) shows the welding on the tube. The penetrant was allowed to soak onto the defects for 10 min. Excess penetrant was then removed from the surface and a white developer PMC flaw check PD-31B has applied the sample which formed a semi-transparent coating on the surface. The developer draws the penetrant out from the defects onto the surface to form a visible indication.

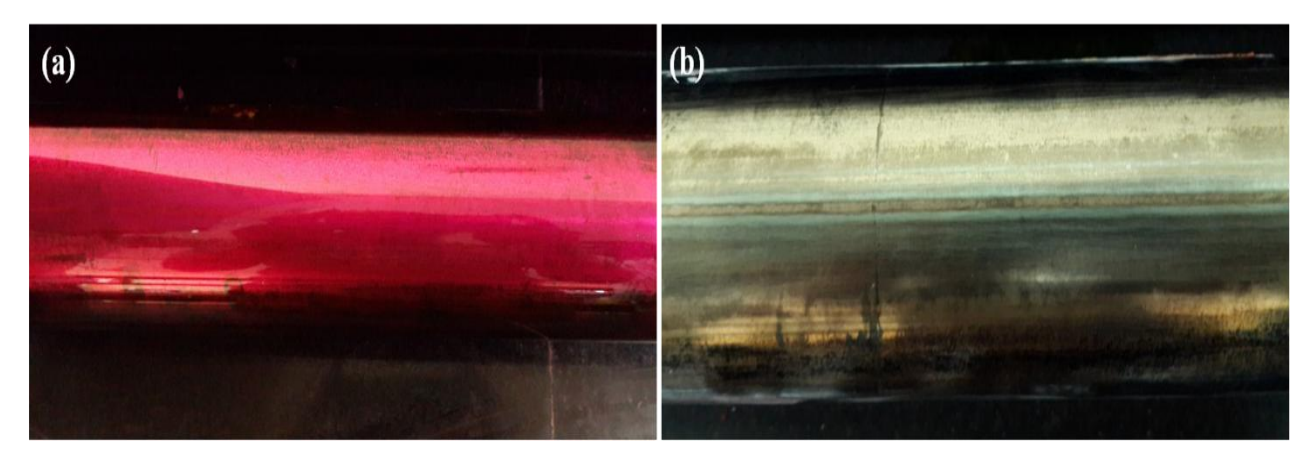


Figure 3.3 Dye penetrate test (DPT) images of AISI 321 stainless steel tubes.

3.3 Heat treatment

Annealing heat treatment was conducted on SS 321 tubes samples to remove residual stresses present in the material after welding operation, heat treated up to 1050°C and holding time 1h [91-92] followed by furnace cooling in a muffle furnace (Nabertherm LT 15).

3.4 Surface roughness measurement

The surface roughness was measured using optical surface profilometer (non-contact mode) on buffed and un-buffed surfaces of LBW, MIG weld and a base material of AISI 321 SS. The scan length and speed of scanning were 1 mm and $47\mu\text{m/s}$ respectively, and the resolution of surface roughness measurements was 0.2 nm, step height accuracy was less than 0.75 %.

3.5 Microstructural characterization

3.5.1 Sample preparation

The samples were mounted by using the cold-setting compound. The samples were prepared using metallographic techniques like polishing with SiC emery papers of grades 120, 240, 320, 600, 800, 1000, 1200, 1/0, 2/0, 3/0 and 4/0 for microstructure evaluation. This was followed by fine polishing with Grade - A Alumina (Al₂O₃) slurry 0.3 μ m diamond suspensions. The samples were then cleaned with water and ethanol and were finally etched using electrolytic etching in 10 % oxalic acid (current density as per ASTM standard A262 Practice C) [93]. To identify the σ and δ ferrite phase present in AISI 321 SS, the specimens were etched using 10 % KOH solution at a voltage of 2.5 V for a period of the 2-5 s [94].

3.5.2 Microstructural Evaluation

3.5.2.1 Optical Microscope (OM)

An optical microscope was used to determine the microstructural details like size, shape and distribution of various phases that include cracks and other defects in metals. Grain size and crack length was determined by image analysis (planimetric method ASTM E112 – 13). The differences in the microstructures of the LBW, MIG and the spot-welded regions of the tubes have been analyzed in this study.

3.5.2.2 Field Emission Scanning Electron Microscope (FESEM)

Field emission scanning electron microscopy (FESEM) was employed to investigate the topographical and elemental information at various magnifications, with high depth of field. When compared to conventional scanning electron microscopy (SEM), field emission SEM (FESEM) produces images with more clarity and less distortion with spatial resolution down to 1.5 nm. The FESEM micrographs were produced by raster scanning with a high-energy beam of electrons. The field emission scanning electron microscope (FESEM) in secondary electron mode with a voltage of 15 kV with attached electron dispersive spectroscopy (EDS) operating at 20 kV.

3.6 X-ray diffraction

X-ray diffractometer (Bruker Model No. D8) was used in the present study. The X-ray source of Cu $K\alpha$ ($\lambda = 1.5406$ Å) radiation operating at 40 kV/30 mA with a 0.02 step size and within the 2 θ range of 20–100°.

3.7 Buffing operation

Buffing is the process of obtaining optimum surface finish in metals, wood, and composites using a cloth wheel impregnated with cutting compounds. The cloth buff holds the compound, while the compound does the cutting. In the surface buffing operation two types of buffing motion is involved as follows:

- a) A Cutting motion which helps in removing the pits and a groove formed during cutting and polishing operations and gives a smooth finishing. The work piece moves against the direction of the rotating wheel under the action of high pressure.
- b) The polishing motion which involves the movement of the work piece in the direction of the rotating wheel under the action of low pressure and gives a shiny surface. Buffing operation majorly

depends on the pressure applied to the sample. If the pressure applied on the work piece is low, buffing does not occur on the sample and if the applied pressure is high, scratches appear on the surface of the samples followed by the wheel damage. In order to get the optimum surface finishing, the wheel speed should range from 3600- 7500 surface feet per minute (SFPM). The SFPM is given by equation 3.2,

$$SFPM = \frac{1}{4} * Diameter of the wheel *RPM of the motor----- (3.2)$$

The buffing process was carried out using 220, 240, 400, 600 and 1000 grit wheels and a buffing wheel at a fixed rotation speed of 3600 rpm to obtain a mirror finish on the work piece.

3.8 Mechanical Characterization Techniques

3.8.1 Hardness Testing

The micro hardness AISI 321 SS heat exchanger tubes for all un-buffed as well as buffed specimens was carried out using Omnitech-MVH-Sauto Micro Hardness tester to know the hardness variations of the base material and weld zone. The load applied on the samples was 500 gm and the dwell time was 10 sec. The micro hardness values recorded for each sample was recorded as an average of 12 measurements.

3.8.2 Residual Stress Measurement

All the surfaces were subjected to X-ray residual stress measurement with Cr-K α X-ray source with a wavelength of 2.289Å. (311) plane at a Bragg's angle of $2\theta = 147.6^{\circ}$ was considered for diffraction for SS samples. The Young's modulus and Poisson's' ratio used for stress calculations in SS samples were 1, 96,000 MPa and 0.28 respectively. Multi-exposure side inclination method was adopted for residual stress measurement after calibrating the instrument with a stress-free powder sample. The residual stress was calculated using X-ray diffraction (XRD) $sin^2\psi$ technique.

Sample preparation

Sample preparation depends on the nature of the residual stresses to be determined. If the stresses produced are due to the surface treatments like machining, grinding, or buffing, the residual stress distribution is usually less than $500 \mu m$ on the sample surface. Therefore, the sample surface must be carefully protected from corrosion or any scale formation.

sin² wtechnique

Measuring the residual stresses through X-ray diffraction is based on Bragg's principle, which is given by the equation 3.3,

$$2dsin\theta = n\lambda - - - - - - - - - - 3.3$$

The $\sin^2\psi$ technique is one of the methods to determine residual stresses from XRD. The angle ψ is the orientation of the surface of the sample. It is the angle between the incident and diffracted bisector of the beam to the normal of the sample surface [95]. In the $\sin^2\psi$ technique, the lattice spacing is determined for multiple ψ tilts for a fixed peak position at a possible highest 20 angle. The linear fit of d vs $\sin^2\psi$ plot determines the sign (compressive or tensile) and the magnitude of the residual stresses. The primary advantage of the $\sin^2\psi$ technique is the minimum data acquisition time for establishing the linearity of d as a function of $\sin^2\psi$ on the sample of interest.

Stress determination

From Hooke's law, we know that (equation 3.4),

$$\sigma = E \varepsilon_{v} - - - - - - - - - - - - - - - - 3.4$$

Though a tensile force produces linear strains in an x-direction, it also produces strains in the transverse direction. if a state of plane stress exists, that is $\sigma_z = 0$, the stresses are biaxial, then the ratio of the longitudinal strain to transverse strain gives Poisson's ratio v;

$$\epsilon_x = \epsilon_y = -\vartheta \frac{\sigma_y}{E} - - - - - - - - - 3.5$$

If the X-ray measurement on the surface of the material is considered as $\sigma_z = 0$ then the resultant is given in equation 3.6,

$$\epsilon_{\varphi\psi} = \frac{1+\vartheta}{E(\sigma_1 cos^2 \varphi + \sigma_2 sin^2 \varphi)} sin^2 \psi - \frac{\vartheta}{E(\sigma_1 + \sigma_2)} - - - - 3.6$$

If we consider the strains in terms of inter-planar spacing and use the strains to evaluate the stresses, then it can be shown that (equation 3.7)

$$\sigma_{\varphi} = \frac{E}{(1+\vartheta)} \sin^2 \psi \left(\frac{d_{\psi} - d_n}{d_n} \right) - - - - - 3.7$$

This equation allows us to calculate the stress in any chosen direction from the inter-planar spacing determined from two measurements, made in a plane normal to the surface and containing the direction of the stress to be measured.

3.9 Determination of stress corrosion cracking (SCC) susceptibility

SCC susceptibility of the tubes was evaluated using boiling $MgCl_2$ test which was done as per ASTM standard G36-94. In this test, 56.6 gm of magnesium chloride hexahydride was immersed in 45 ml of distilled water. 15 ml of this solution was added with 600 gm of magnesium chloride hexahydrate. The mixture was taken into an Erlenmeyer flask and was heated to $155 \pm 1^{\circ}C$ on a hot plate. The temperature was maintained constant using a thermometer. A condenser was placed on top of the flask, which condenses the mixture with the help of water flowing through it. After the completion of this test, the specimens were washed under water and were cleaned using acetone. The specimens were then characterized by using optical microscopy and FESEM. Figure 3.4 shows the boiling Magnesium chloride test setup.

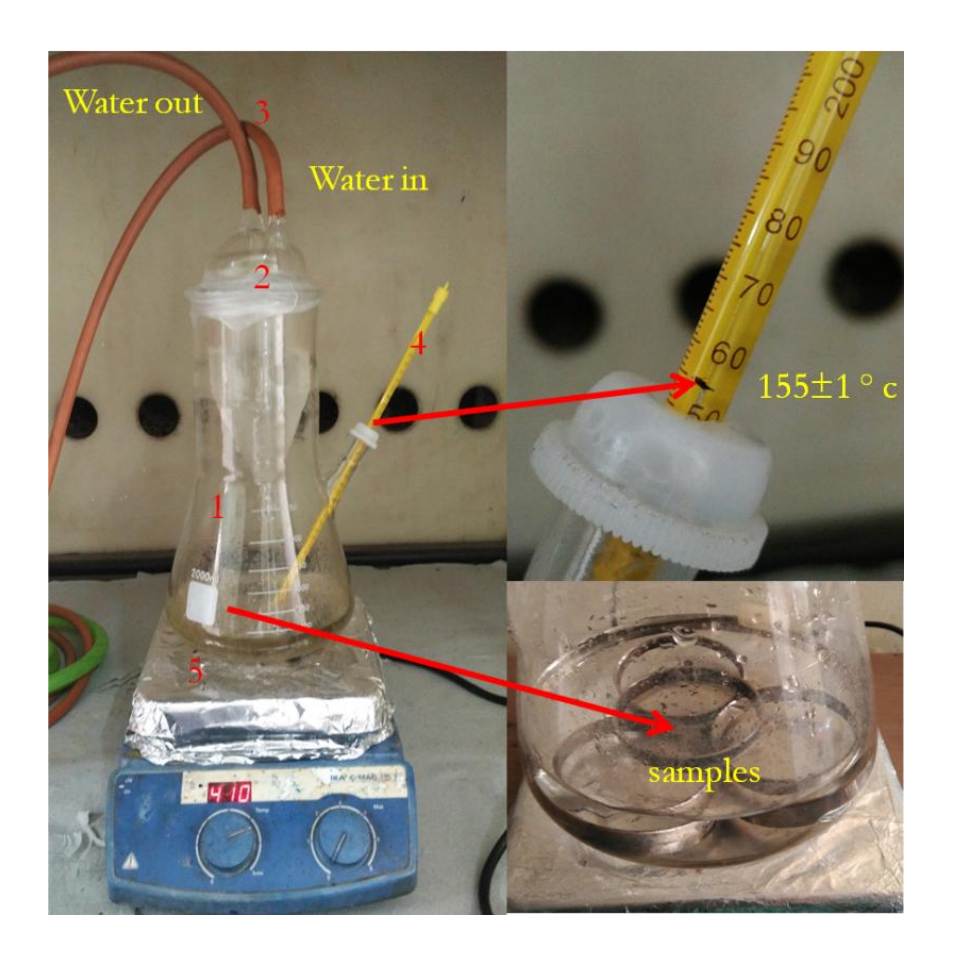


Figure 3.4 Boiling magnesium chloride test setup [ASTM G36-94] for evaluating SCC resistance of metals and alloys in a boiling MgCl₂ solution, (1) Erlenmeyer flask, (2) condenser, (3) water inlet and outlet, (4) thermometer, (5) heater.

CHAPTER 4

4.0 RESULTS AND DISCUSSION

4.1 PART-I: Failure analysis of AISI 321 stainless steel (SS) welded tubes in solar thermal power plant

The present study investigated the failure of a number of welded stainless steel AISI 321 tubes used for transportation of hot thermic fluid it contains 1.5 mg/kg chloride (~ 400°C) from the parabolic heat collectors to the heat exchangers in solar thermal power plants. The tubes were seam welded using either LASER beam welding (LBW) or metal inert gas welding (MIG), together with spot welds at selected locations on the surface. The failure of the tubes led to the leakage of hot thermic fluid while in service. The root cause of such failure should be understood in order to control such instances in future. Hence a detailed failure analysis has been carried out and reported in this chapter.

4.1.1 Visual Examination and Dye Penetrant Testing

The results of the dye penetrant test did not show the presence of any macro cracks on the surface of LBW and MIG samples during a visual examination. However, thermic fluid stains were observed near the weld regions of seam and spot welds. Dye penetration test was conducted to check for the presence of cracks on the surface of the tubes especially at the weld regions. As shown in Figure 4.4, cracks were observed both on the outer surface and inner surface of the tubes near the spot welded region, whereas no cracks were observed near the seam welds. Figure 4.2 (a) shows the actual plant AISI 321 SS tube the entire tube was encased in a glass sealing and vacuum was maintained within the sealing. (b) Shows the schematic of AISI 321 stainless steel tube heat exchanger and different weld locations, Figure 4.3 showed the location of the spot weld region and Figure 4.1 shows the schematic of the solar thermal power plant.

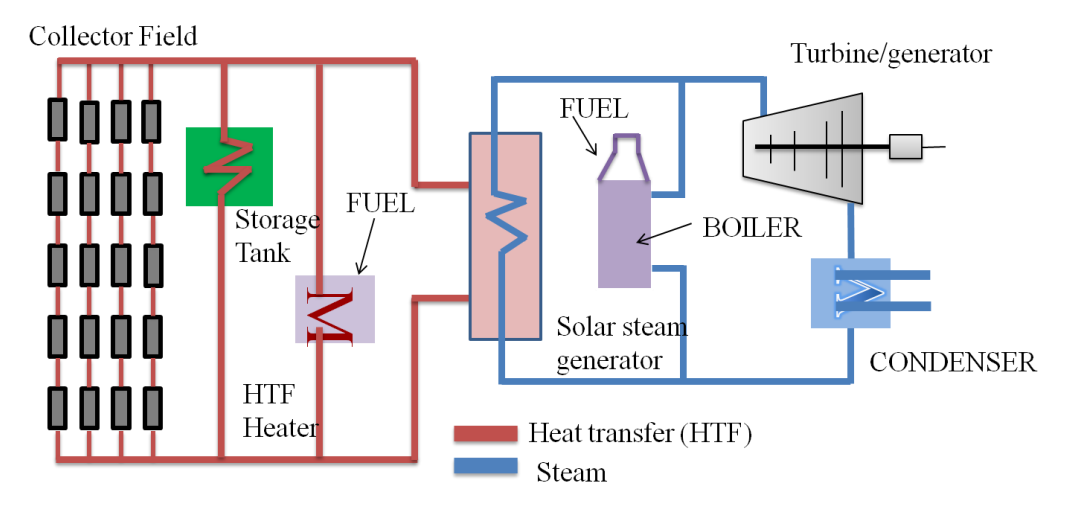


Figure 4.1 shows the schematic of solar thermal power plant

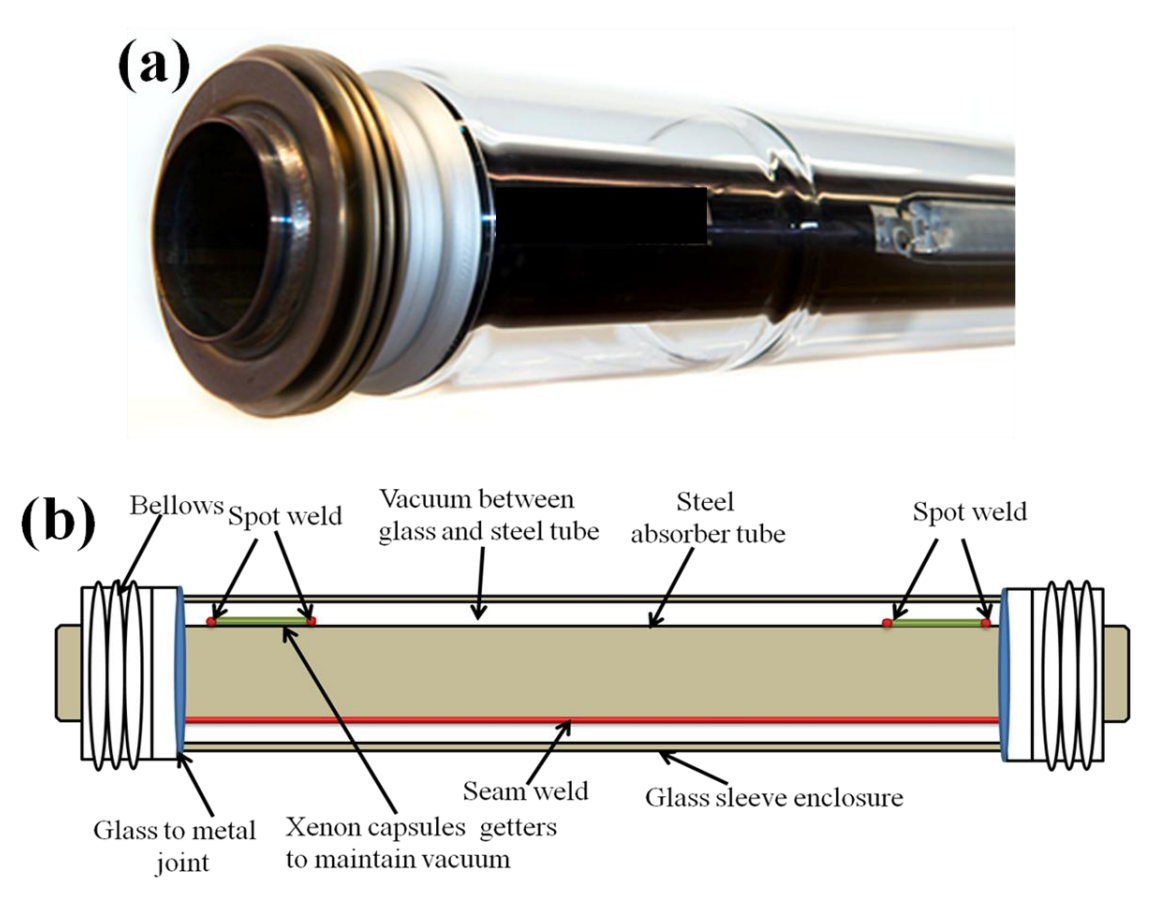


Figure 4.2 (a) shows the actual plant AISI 321 SS tube (b) shows the schematic of AISI 321 stainless steel tube heat exchanger

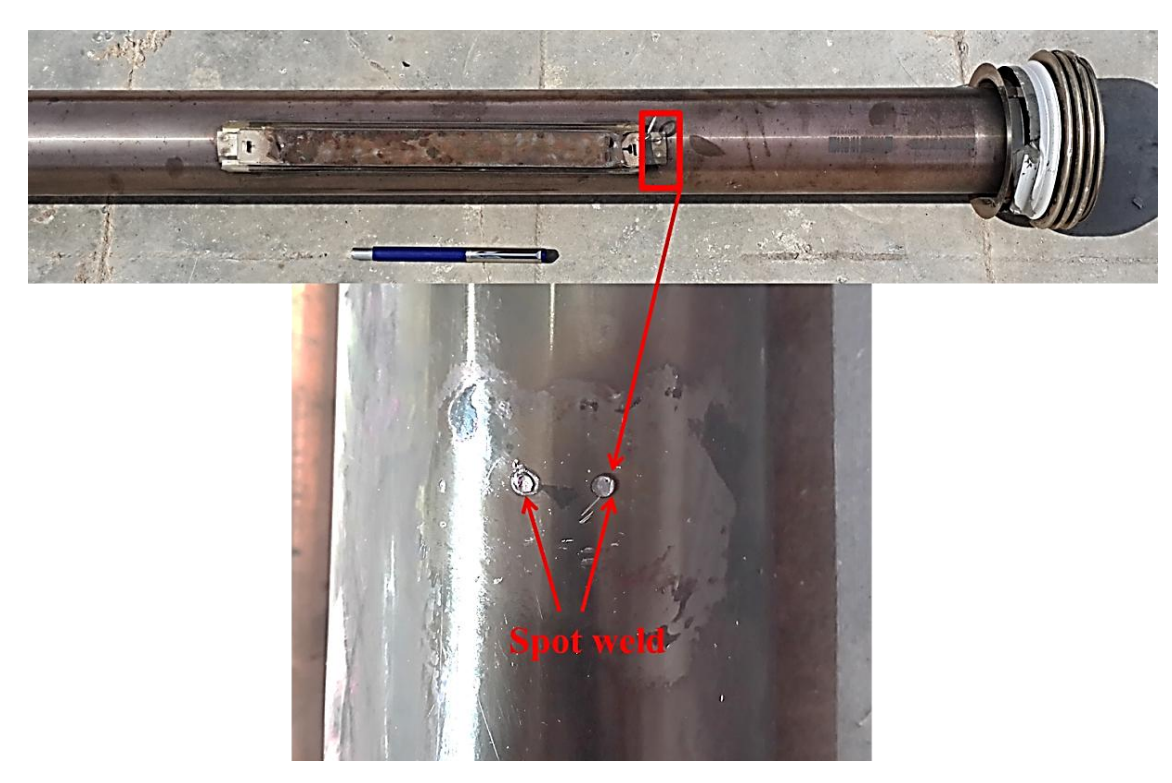


Figure 4.3 shows the heat exchanger tube and location of the spot weld

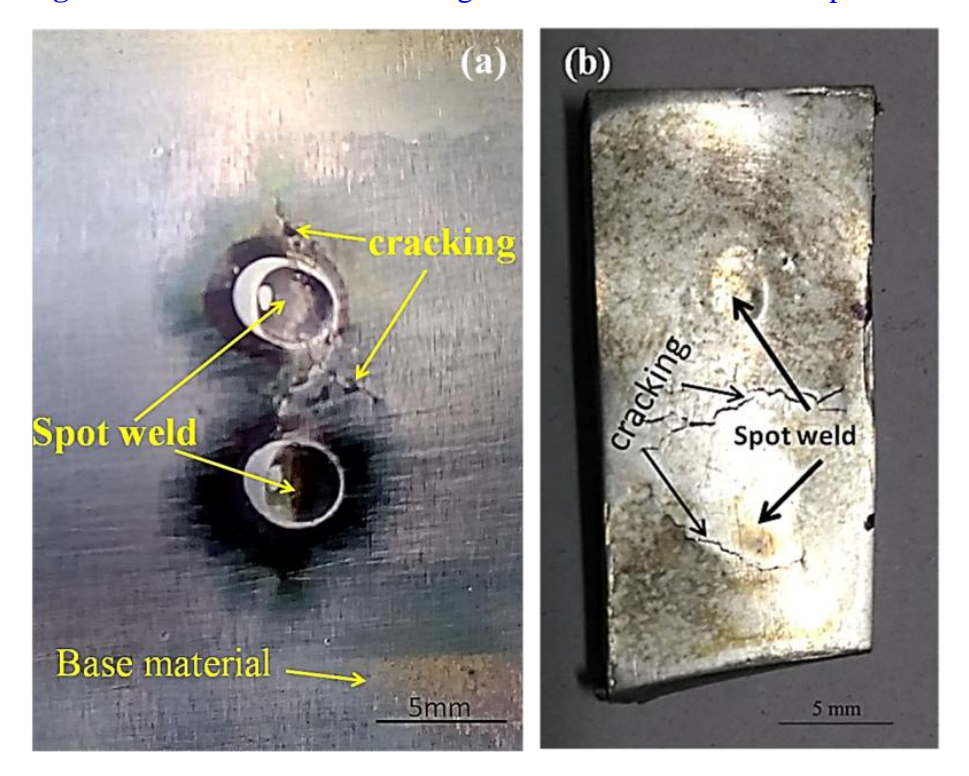


Figure 4.4 (a) Shows the cracks on the outer surface of the tube near the spot weld and (b) shows the cracks detected on the inner surface of the tube near the spot weld by dye penetration test.

4.1.2 X-ray diffraction of all welded AISI 321 SS tubes

The X-ray diffraction spectra of the weld samples LBW, MIG weld and spot weld, are shown in Figure 4.5. Austenitic (γ) peaks were identified JCPDF (00-047-1405) together with Ti₂N peaks at (112) and (224) planes were determined from JCPDF data (00-023-1455), δ ferrite peaks at (110) and (211) planes were determined from JCPDS data (00-035-1375). The X-ray diffraction spectra collected from the welded samples in each case encompasses the fusion zone, heat affected zone and the base metal and the results are shown in Figure 4.5. The X-ray spectra of the individual regions could not be scanned in the present study. Micro-XRD studies would be carried out in future for determination of X-ray spectra from individual regions. The aim of the XRD experiments was to identify the several precipitates present in the material.

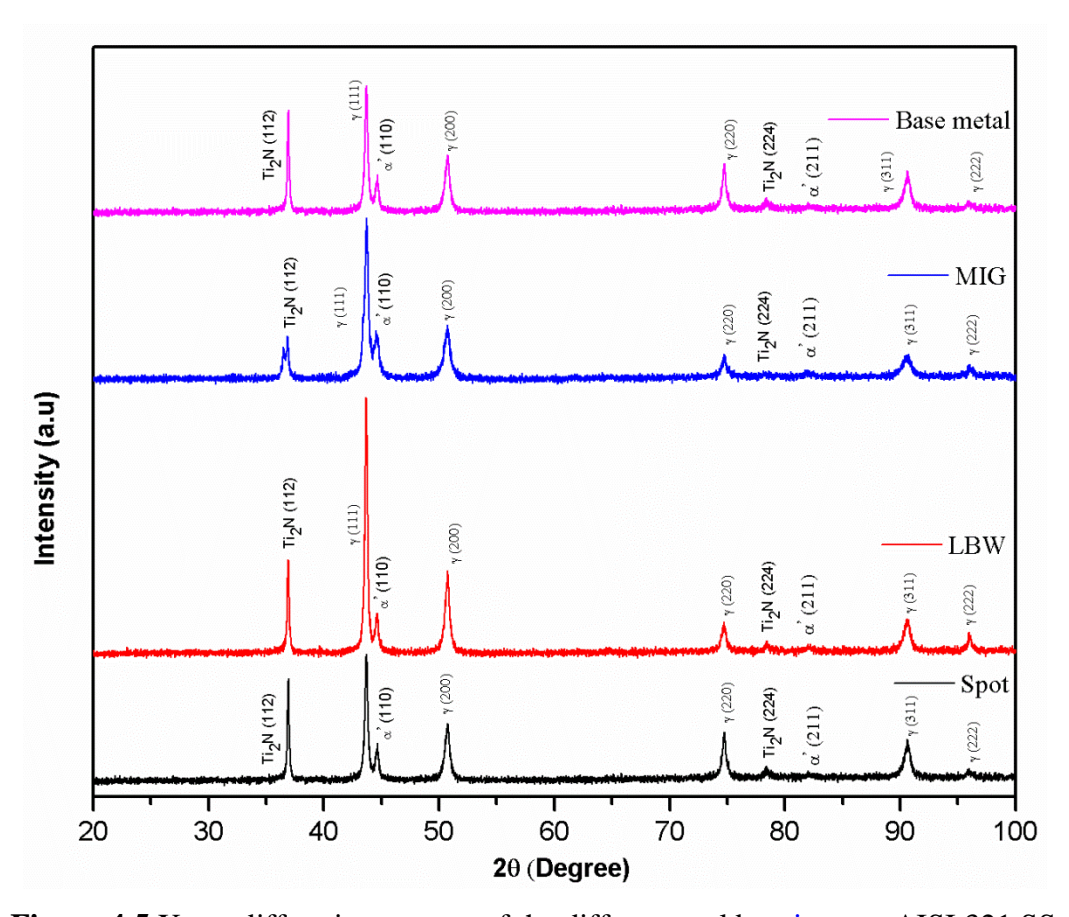


Figure 4.5 X-ray diffraction spectra of the different weld regions on AISI 321 SS

4.1.3 Micro hardness measurement

The hardness profile measured across the cross-section of the 321 SS tube is shown in Figure 4.6. The results indicated very high hardness near the inner surface of the LBW and in the outer surface near the spot welds. The high hardness in these regions was due to the high magnitude of tensile residual stresses due to welding. Very high heating and cooling rates involved in LBW were responsible for high residual stress levels on these welds. Lower heating input leads to slow cooling rates in MIG welds lead to a lower magnitude of hardness which also indicated that the residual stresses in the material were lower in this case. In case of spot welds (present on the external surface of the tubes) the constraint during welding was primarily responsible for high residual stresses. Due to the presence of constraints, the components were not free to expand or contract with ease and hence high magnitude of locked up tensile residual stresses were generated in the material resulting in high hardness values. The expected hardness values of these tubes are ~175-180 HV [96-97].

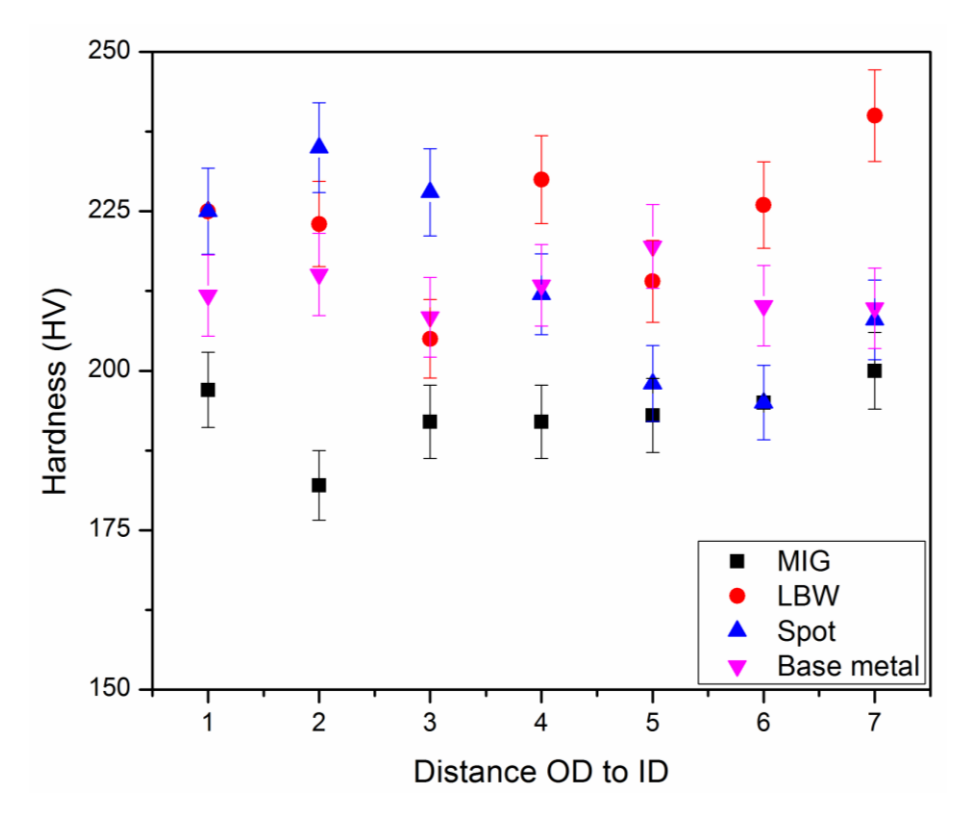


Figure 4.6 Micro hardness profiles of the differently welded AISI 321 SS tubes

4.1.4 Microstructural characterization of the base material of AISI 321 stainless steel

The microstructure of the as-received AISI 321 SS in the region far away from the weld can be seen in Figure 4.7. Polygonal grains of the austenitic matrix together with very fine precipitates were observed. The average grain size of the base material was $\sim 39 \pm 10 \, \mu m$. The grains were equiaxed in nature. Grain size was measured using the planimetric method ASTM E112 – 13 by using optical microscopy software (Olympus). The precipitates were identified to be Ti(C, N), Ti₂N, δ -ferrite, and σ respectively. The particle size range is ~ 2 to 3 μm was measured by FESEM and composition was determined by Energy dispersive spectrometry (EDS) analysis.

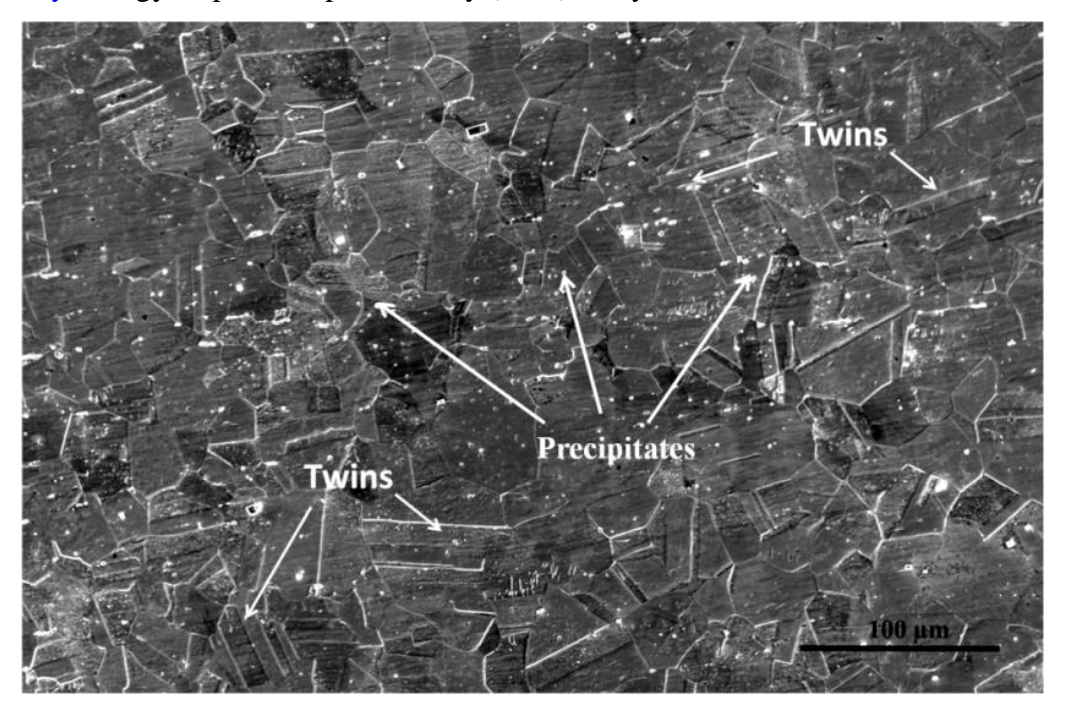


Figure 4.7 FESEM micrograph of the AISI 321 stainless steel base material

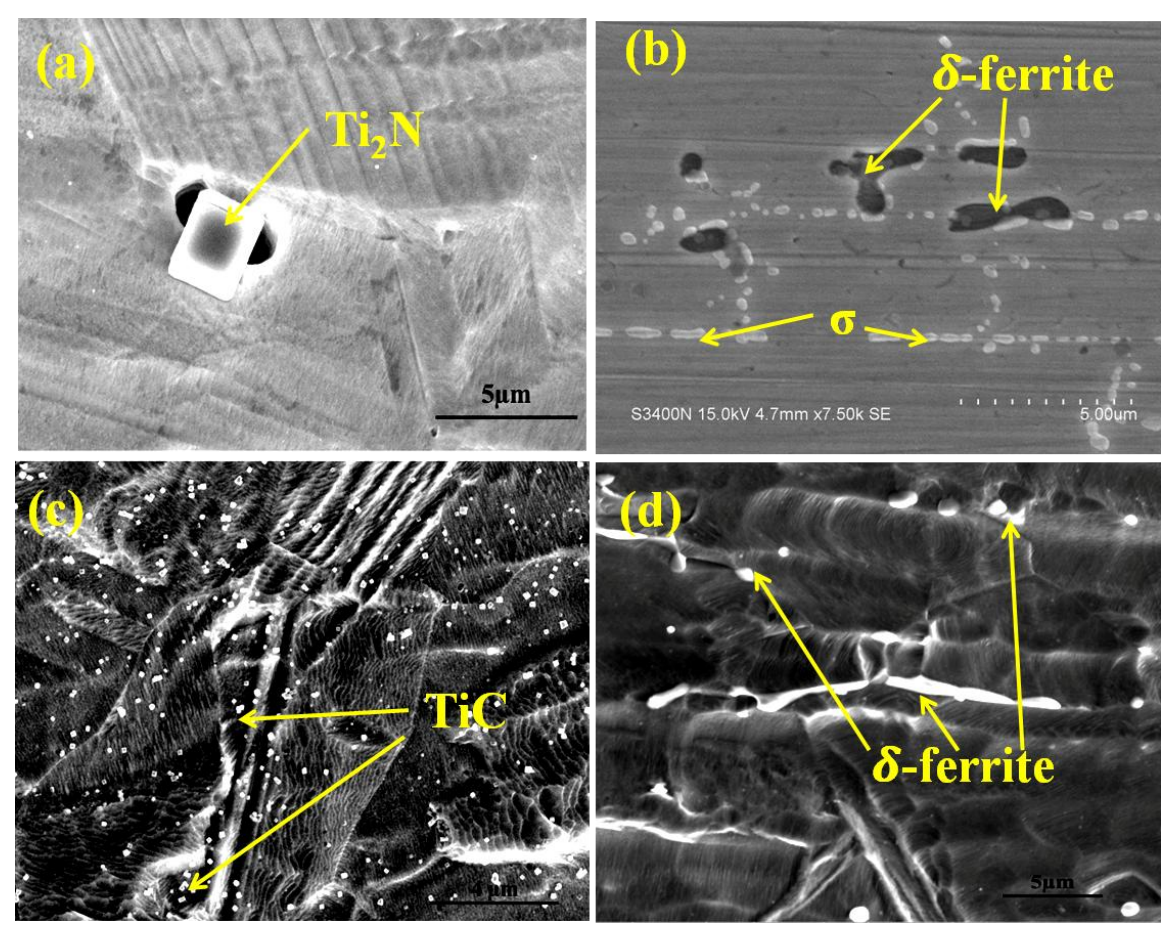


Figure 4.8 FESEM microstructure of AISI 321 SS tube showing different precipitates at different regions, (a) Ti₂N, (b) σ and δ-ferrite (10N KOH solution), (c) Ti (C, N), and (d) δ-ferrite

Figure 4.8(a) shows Ti_2N and Figure 4.5 (c) shows the TiC. The Ti_2N precipitates were rectangular ~ 5 μ m to 7 μ m in size, whereas the Ti (C, N) precipitates were much finer ~2-3 μ m and both precipitates were rectangular in shape and were randomly distributed in austenite matrix.

When compared with LBW weld region micrographs the MIG weld region showed a high volume fraction of δ -ferrite content. The δ -ferrite volume fraction in LBW region was ~0.58%. where as in MIG weld region showed ~3.39%.

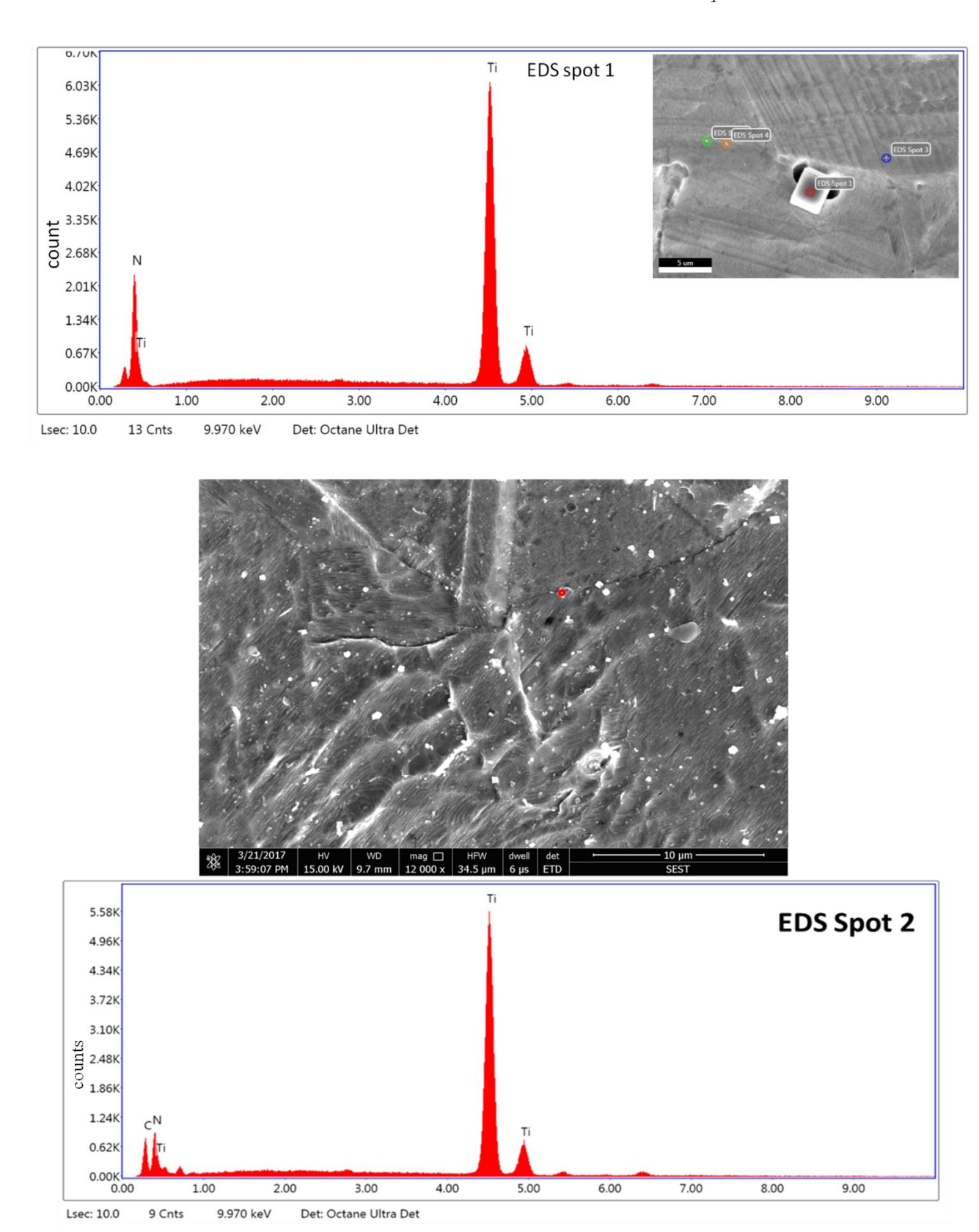


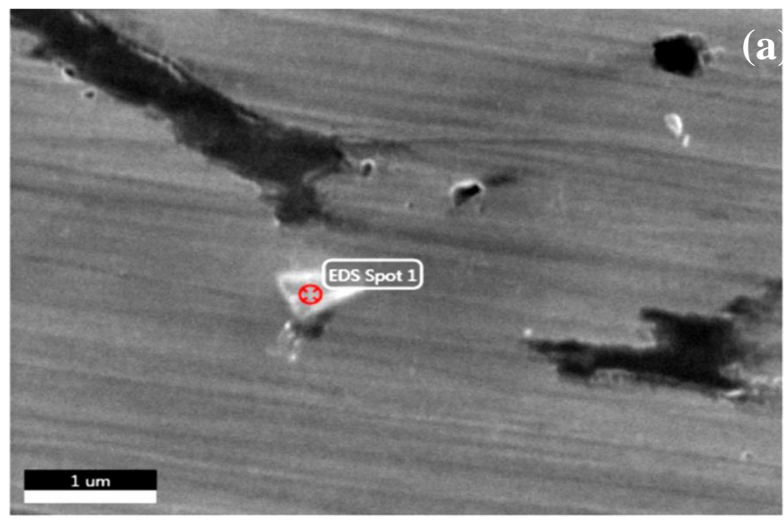
Figure 4.9 EDS spectra of Ti₂N (EDS spot 1) and Ti (C, N) (EDS spot 2)

The composition as obtained from EDS was Ti_2N : 73-Ti, 27-N, and Ti (C, N): 82.9-Ti, 7.4-N, and 9.7-C. The EDS spectra of the Ti-rich precipitates are shown in Figure 4.9. Micrograph in Figure 4.8(d) shows the δ -ferrite in the austenite matrix. The δ -ferrite was needle-like structures and was present at the flow lines and grain boundaries.

The δ -ferrite and σ phase were present near the MIG welded tube at the interface of the fusion zone and the heat affected zone. Figure 4.8(b) shows the σ phase (bright) and δ -ferrite (dark phase). 10N KOH [94] was used for revealing the δ -ferrite and σ phase that was oriented along the interface of the MIG weld. The σ phase was rich in Cr and Mo. Table 4.1 represented the chemical composition of the σ phase and δ -ferrite obtained from EDS. Figure 4.10 and Figure 4.11 shows the FESEM electron image and EDS spectrum of sigma (σ) and delta (δ)-ferrite respectively.

Table 4.1 The chemical composition of σ phase and δ -ferrite obtained from EDS

Elements (wt %)	Cr	Si	Mo	Ni	Fe	Mn
σphase	20.03	0.44	0.36	6.88	70.61	1.68
δ –ferrite	25.88	0.18	0.16	5.34	67.75	0.69



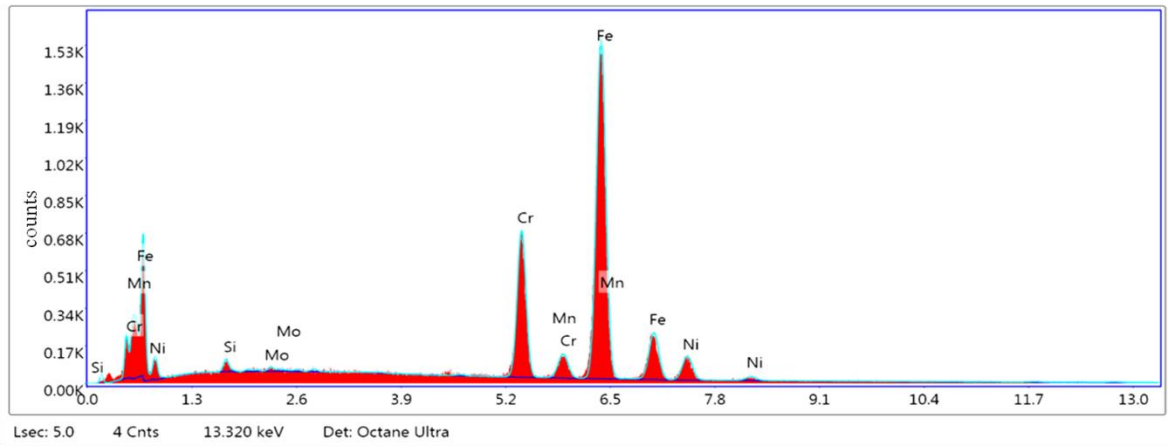
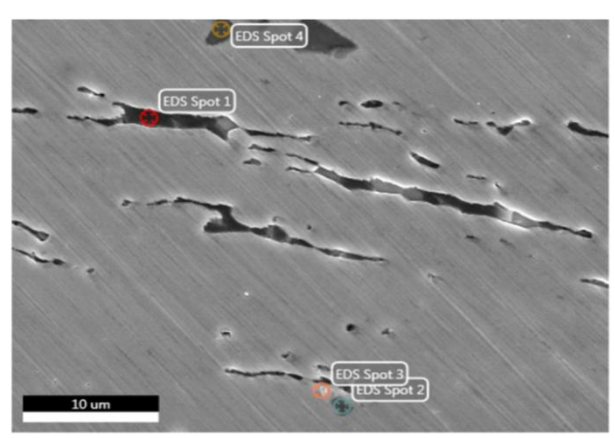


Figure 4.10 FESEM electron image and EDS spectrum of sigma (σ)



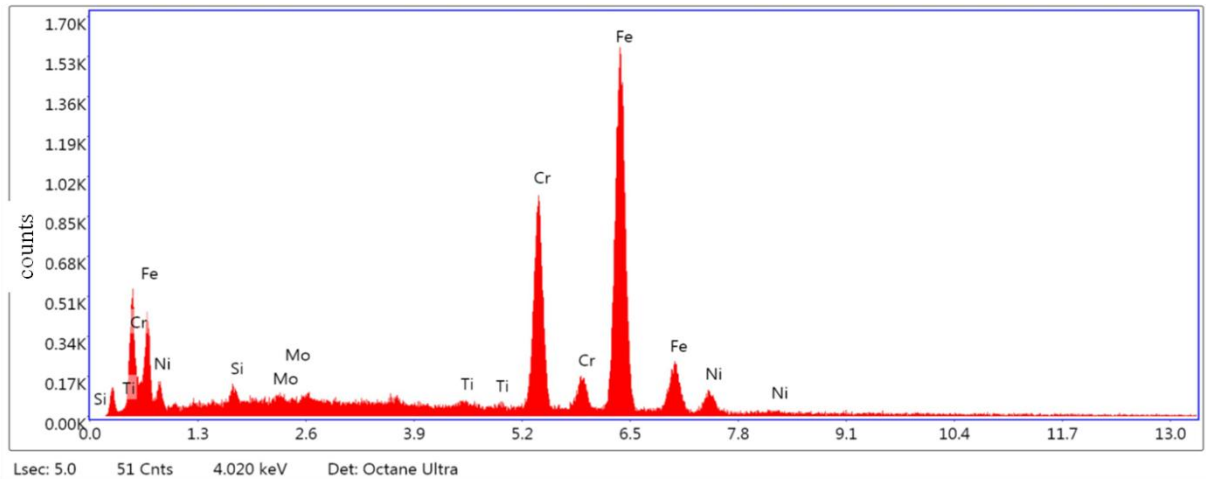


Figure 4.11 Electron image and EDS spectrum of delta (δ -ferrite)

4.1.5 Microstructural characterization of the differently welded region of AISI 321SS tubes 4.1.5.1 Spot welded region of the tubes

The microstructural characterization of the spot welded region provided showed stress corrosion cracking in this region of the AISI 321 SS tubes. Figure 4.12 shows the cross-sectional view of the tube in the region near the spot weld with the presence of a number of cracks. The spot welded region can be seen as a dark patch near the outer surface of the tube. Cracks were initiated from the inner surface of the tube and extended towards the outer surface. Throughout the thickness of the tube, cracks were formed near the spot welded region which led to leakage of the thermic fluid. Figure 4.12 shows the cracks were heavily branched and transgranular in nature. And the magnified view was shown in Figure 4.13

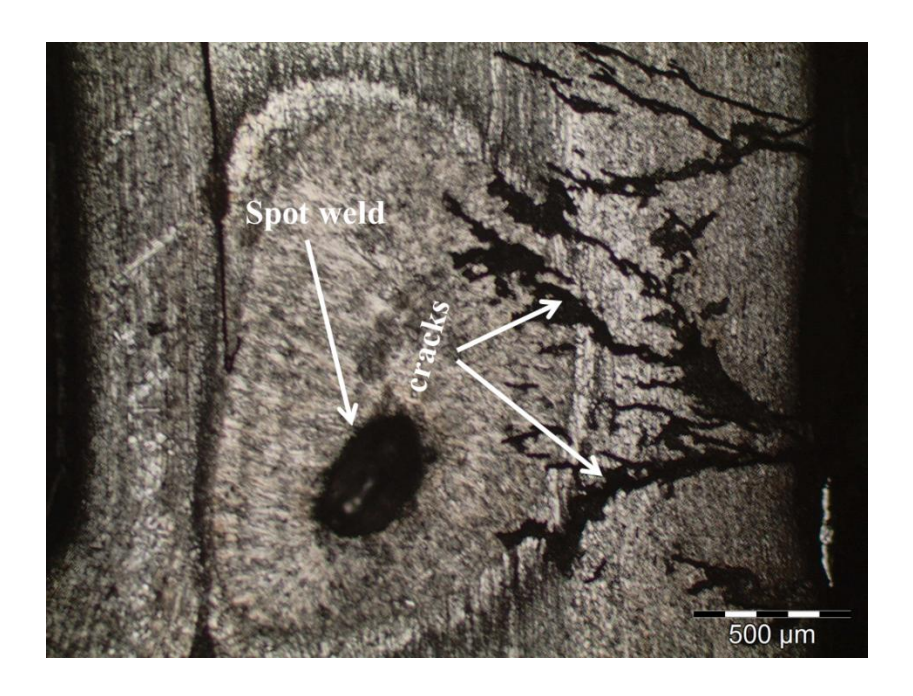


Figure 4.12 The optical micrographs of cracks in the spot welded region of AISI 321 SS tube The atmospheric chloride cannot be the cause of SCC due to the following reason:

The entire tube was encased in a glass sealing and vacuum was maintained within the sealing. The picture of the as-received tubes with the glass sealing is shown below and has been included in the thesis Fig. 4.2(a). The schematic of the structure of the pipe has also been included. Hence the outer surface of the tube was not in contact with the atmosphere.

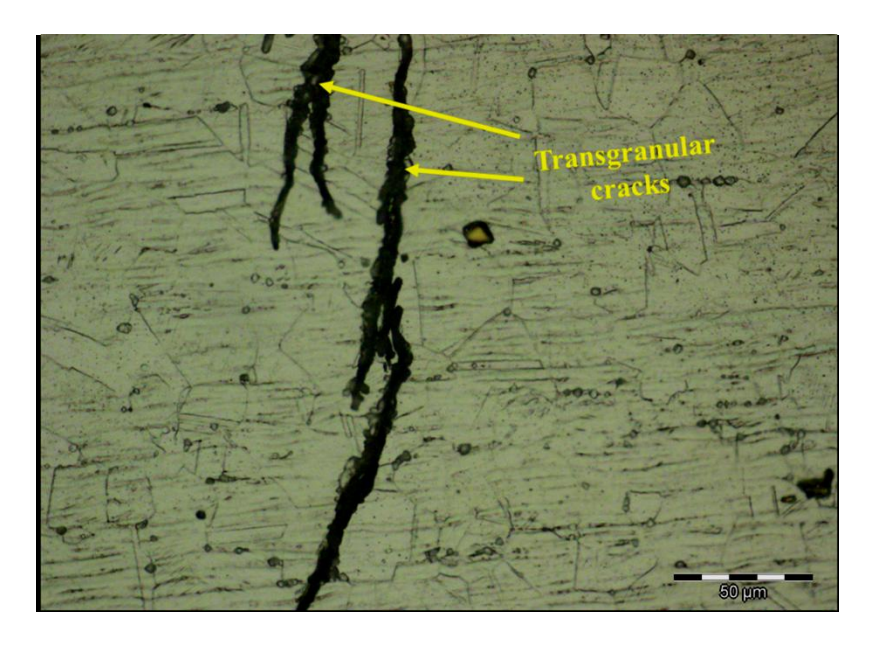


Figure 4.13 The magnified view of the cracked region

The magnified view of the cracked region is shown in Figure 4.13. Extensive cracking was observed and the cracks were transgranular in nature. Crack branching and transgranular cracking are characteristic features of chloride-induced stress corrosion cracking (SCC) of austenitic stainless steel in chloride environment [96-100]. The cracks were found to initiate in the inner side of the tube and propagate till the outer surface of the tube leading to the leakage of the thermic fluid (Figure 4.13). The cause of the failure has been established to be chloride-induced stress corrosion cracking based on the following: a) Transgranular nature of cracking and extensive crack branching were evident in the cross section of the 321 SS near the spot weld both of which are the characteristic features of chloride induced SCC, b) chloride level in the thermic fluid and its temperature were above the critical level for chloride induced SCC of austenitic stainless steel, c) the residual stress present in the tubes were above the threshold level as confirmed from SCC tests (ASTM G36) [9-11,22,73,101-102].

4.1.5.2 Laser beam welded tubes

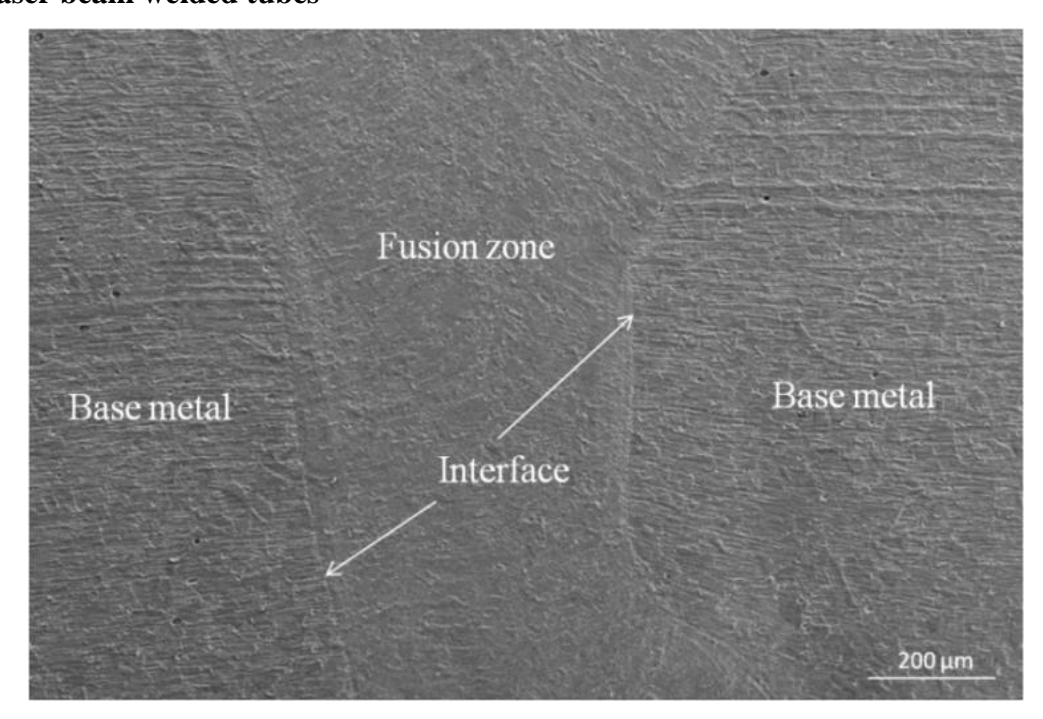


Figure 4.14 FESEM micrograph of Laser beam weld (LBW)

The cross-section of the laser beam welded (LBW) region of the tube of AISI 321 SS is shown in Figure 4.14. Figure 4.15 shows the interface of the fusion zone and base material of laser beam welded AISI 321SS tube. The interface as seen in the micrograph is after etching and hence the

region of attack around the interface is 1 μm thick of the weld fusion zone and the base material as shown in Figure 4.16.

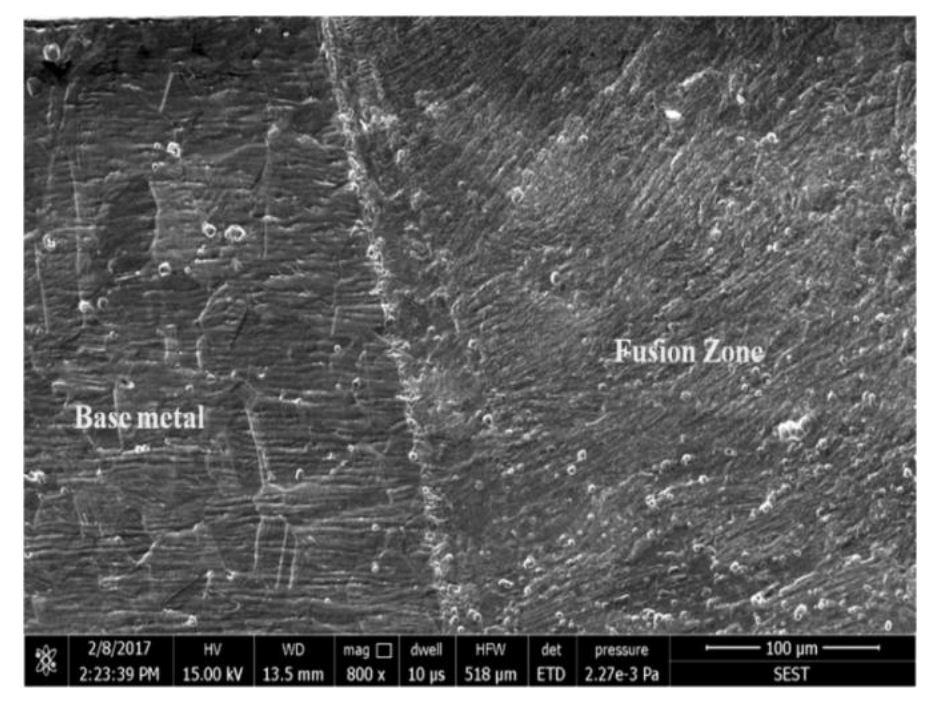


Figure 4.15 FESEM micrograph of the interface of the fusion zone and base metal of laser beam weld

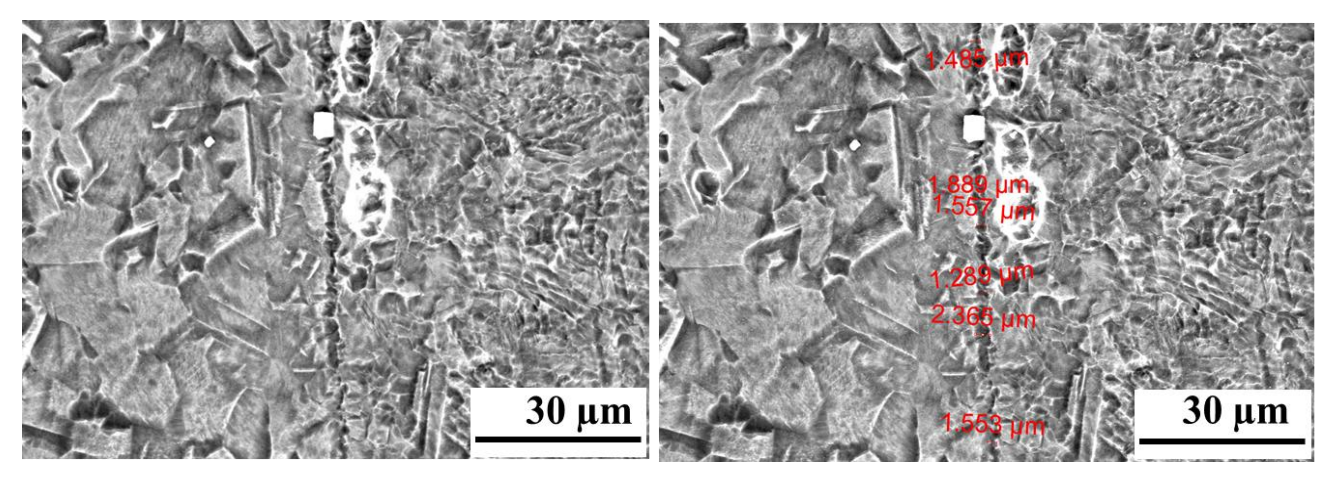


Figure 4.16 FESEM micrograph of LBW 321 SS tube showing the interface of fusion zone and base material

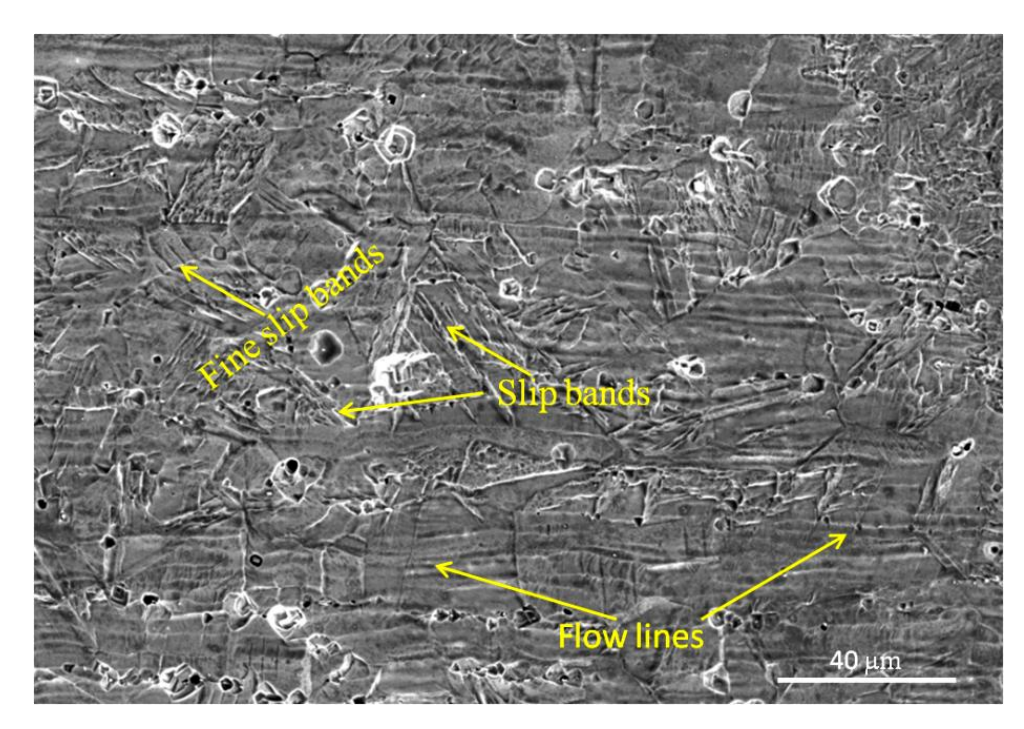


Figure 4.17 FESEM micrograph of LBW 321 SS tube showing slip bands and flow lines in the base material region away from the weld zone

Figure 4.17 shows the FESEM image of the base metal region away from laser beam welded (LBW) region in AISI 321 SS tube showing austenitic grains together with Ti₂N precipitates. The presence of flow lines indicated the presence of strain in the material prior to welding. Slip bands were also detected in the austenitic matrix indicating the presence of plastic strain which can be attributed to the high cooling rate and the presence of constraint, during laser beam welding resulted in thermal shock in austenitic stainless steel components. The formation of slip lines is primarily the result of strain causing flow lines as it also extended in the base metal region. The strain resulting from laser welding would be localized near the narrow fusion zone.

4.1.5.3 Metal inert gas welded tubes

Figure 4.18 (a) shows the FESEM micrographs of base material near the MIG weld fusion zone which shows equiaxed austenitic grains along with annealing twins. Fusion zone grain represented a cellular morphology which is shown in Figure 4.18 (b). The average grain size in the base material of MIG weld samples was found to be $\sim 30 \pm 10 \ \mu m$.

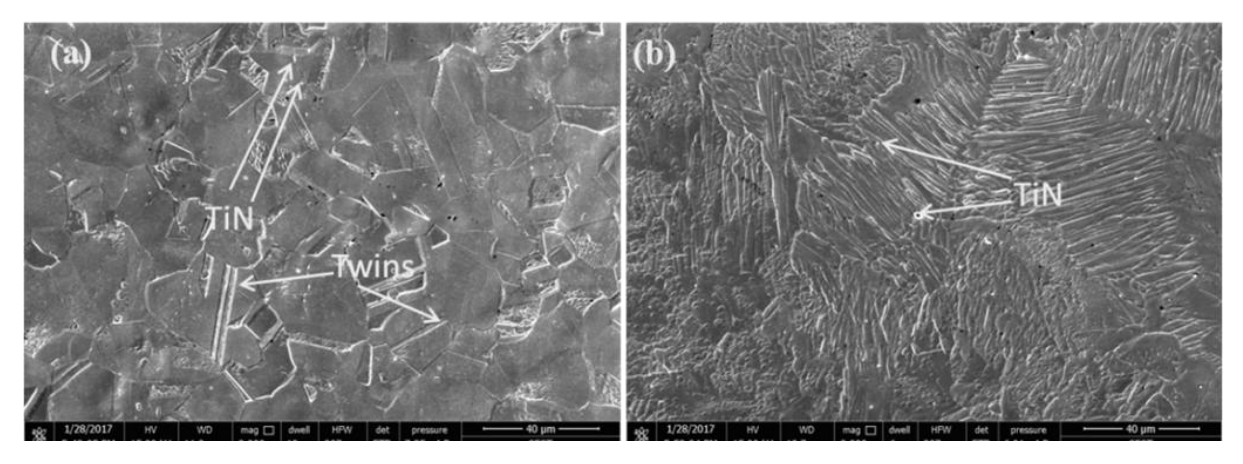


Figure 4.18 FESEM micrographs of the different regions of MIG welded AISI 321 stainless steel (a) polygonal grains in the base metal (b) dendritic structure in the fusion zone

Figure 4.19 shows the interface of the fusion zone and the base material of the MIG welded sample and Figure 4.19 (a) shows the interface between base metal and fusion zone with Ti_2N precipitates. Figure 4.19 (b) shows the presence of the σ phase and delta ferrite (δ) in the MIG welded region. The σ phase forms a network near the interface of the welds which is a major issue during welding of stainless steels. δ -ferrite will be transformed to Cr rich σ phase at temperatures ranging from 450 °C to 850 °C which is detrimental to the integrity of austenitic stainless steel welds [103-104]. The formation of ferrite in the weldment can be controlled by selecting a filler metal with the appropriate chromium and nickel equivalent

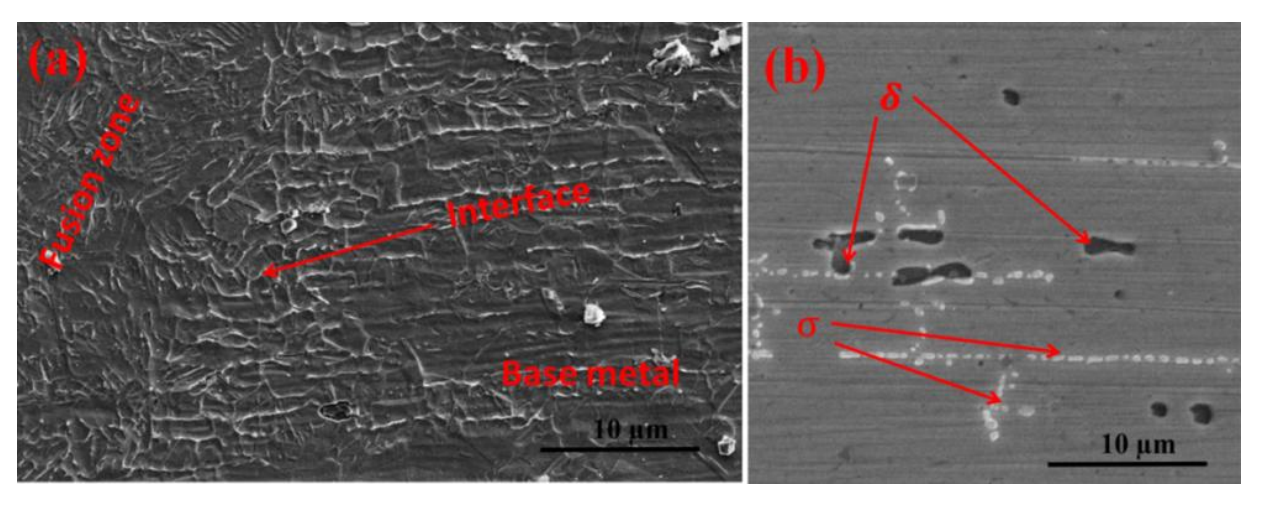


Figure 4.19 FESEM cross sectional micrographs of a) MIG welded AISI 321 stainless steel tube near the weld interface and b) distribution of σ phase (etched using 10N KOH solution) and δ ferrite near the interface of fusion zone and base metal.

. Summary (Part I)

AISI 321 SS tubes failed during their service period after a short exposure (~ 2-3 h) to conditions leading to leakage of the thermic fluid have been analyzed. The seam welds were made either by a) laser beam welding (LBW) or by metal inert gas welding (MIG) together with spot welds on the surface. The root cause for the failure of these tubes was analyzed and the findings of the study are summarized below:

- 1. Failure of the tubes occurred due to chloride-induced SCC near the spot welds on the upper surface of the tubes. No SCC was observed near the MIG welds or Laser welds.
- 2. The MIG welded 321 SS weld tubes contained ~3.39% (volume fraction) of δ ferrite at the weld interfaces whereas it was ~0.58% for LBW.
- 3. Transgranularcracking with extensive crack branching was evident near the spot weld in each of the tubes.
- 4. The failure analysis was done on the AISI 321 heat exchanger tubes that underwent leakage. The analysis confirmed that the cause for this failure to be chloride induced cracking.
- 5. **Table 4.2** The grain size of the AISI 321 SS tubes

S. No	Material condition	Grain size
1	Base material	\sim 39 ± 10 μ m
2*	LBW	$\sim 43 \pm 10 \ \mu m$.
3*	MIIG	$\sim 30 \pm 10 \ \mu m$.
4*	spot weld	$\sim 20 \pm 10 \ \mu m$

^{*}The grain size was measured adjesent to the weld (~100µm)

4.2 PART-II: Stress corrosion cracking (SCC) susceptibility of LBW, MIG and base metal of AISI 321 SS tubes

The SCC susceptibility of AISI 321 SS welds were tested in boiling MgCl₂ environment. The test was done as per ASTM G36 at varying time intervals of 5 h, 10 h, and 72 h (without heat treated). And after post weld heat treatment for 5 h test was conducted. This was followed by the characterization of samples using optical microscopy and FESEM which was done to understand the nature and morphology of cracking.

4.2.1 Microstructural characterization of LBW specimen after MgCl₂ test for 5 h, 10 h, and 72h

The micrograph of the LBW specimen which was subjected to the boiling MgCl₂ test for 5 h is shown in Figure 4.20. The presence of primary and secondary cracks could be observed. Figure 4.20(a). Figure 4.20 (b) shows the FESEM surface micrograph of the polished and etched cross section of 5 h tested specimen shows the fusion zone and weld interface.

4.2.1.1 Micrographs of LBW region after MgCl₂ test for 5 h

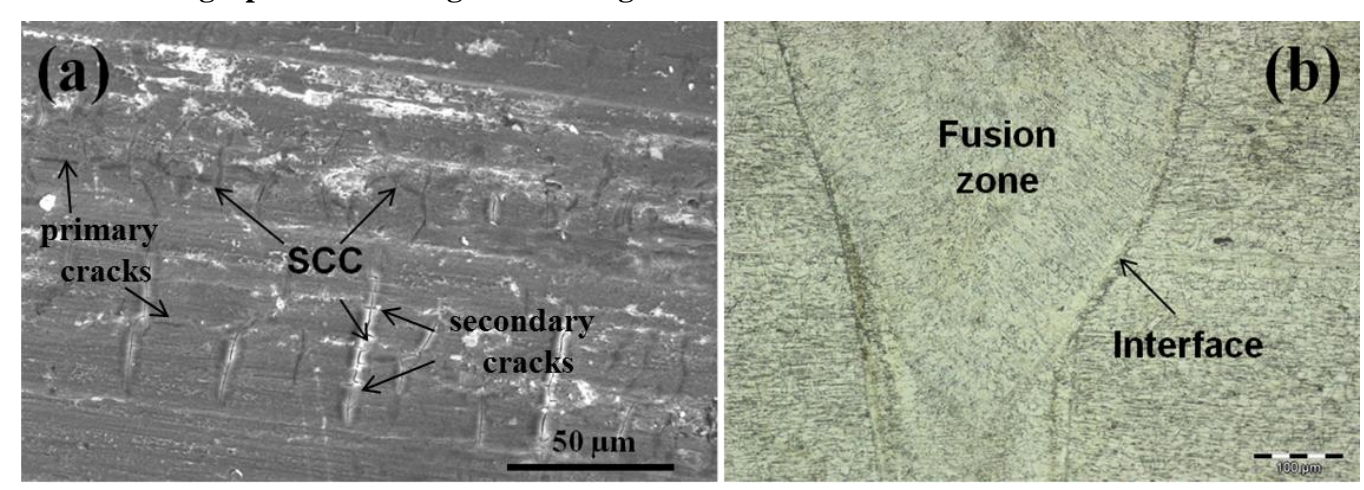


Figure 4.20 (a) FESEM micrographs of LBW welded tubes surface after boiling magnesium chloride test for 5h and (b) optical micrograph of cross section near LBW welded zone after 5h test

4.2.1.2 LBW specimen after MgCl₂ test for 10 h

Exposure of the LBW specimen to boiling MgCl₂ solution for 10 h resulted in higher crack length as shown in Figure 4.21. FESEM micrograph of LBW welded tube cross section has shown heavily branched SCC which is observed in Figure 4.21 (b). The cracks start from the surface.

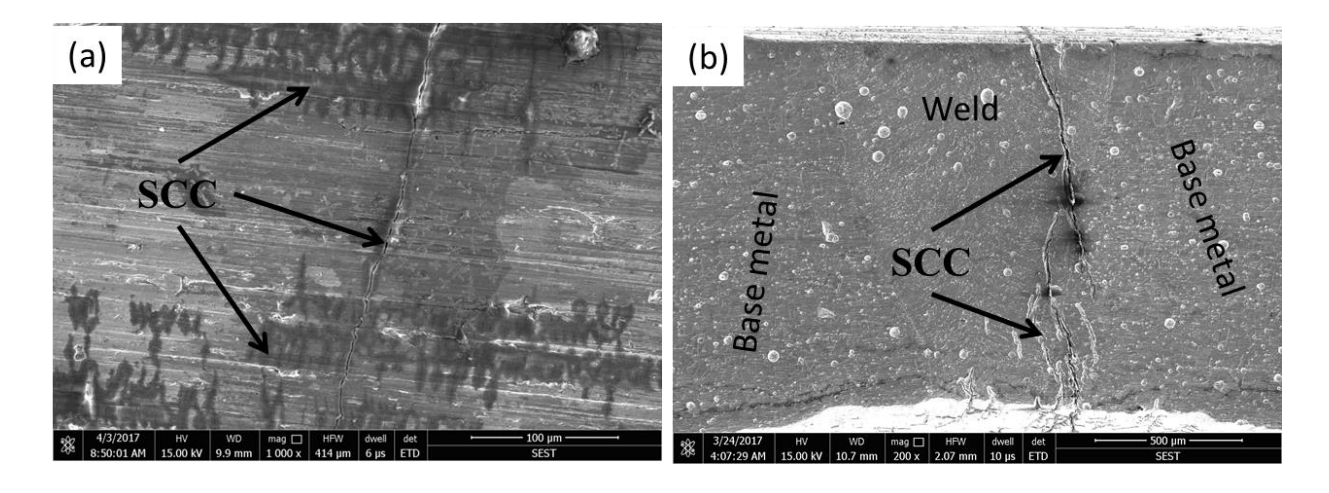


Figure 4.21 FESEM micrographs of LBW welded tubes after boiling magnesium chloride test for 10h; (a) surface and (b) cross section

Figure 4.21 (a) shows the FESEM micrograph of the LBW sample surface which shows the formation of primary and secondary cracks. The primary cracks were observed at higher magnification as shown in Figure 4.22 the cracks were larger and deeper in size.

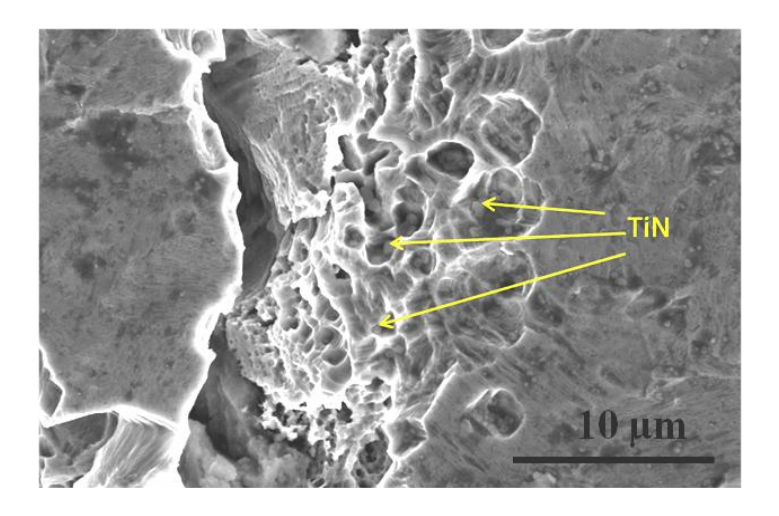


Figure 4.22 FESEM cross section micrographs of LBW weld sample after MgCl₂ test for 10 h 4.2.1.3 LBW specimen after MgCl₂ test for 72h

When the LBW specimen was exposed to boiling MgCl₂ for 72 h, the extensive crack formation was observed. It was observed that the crack density and crack propagation were directly proportional to the exposure time and residual stresses. Complete failure (split into two pieces) was observed after exposing the sample for 72 h. Optical micrographs of LBW weld after MgCl₂ test for 72 h are shown

in Figure 4.23.SCC was observed and crack width was increased after a prolonged exposure for 72 h test.

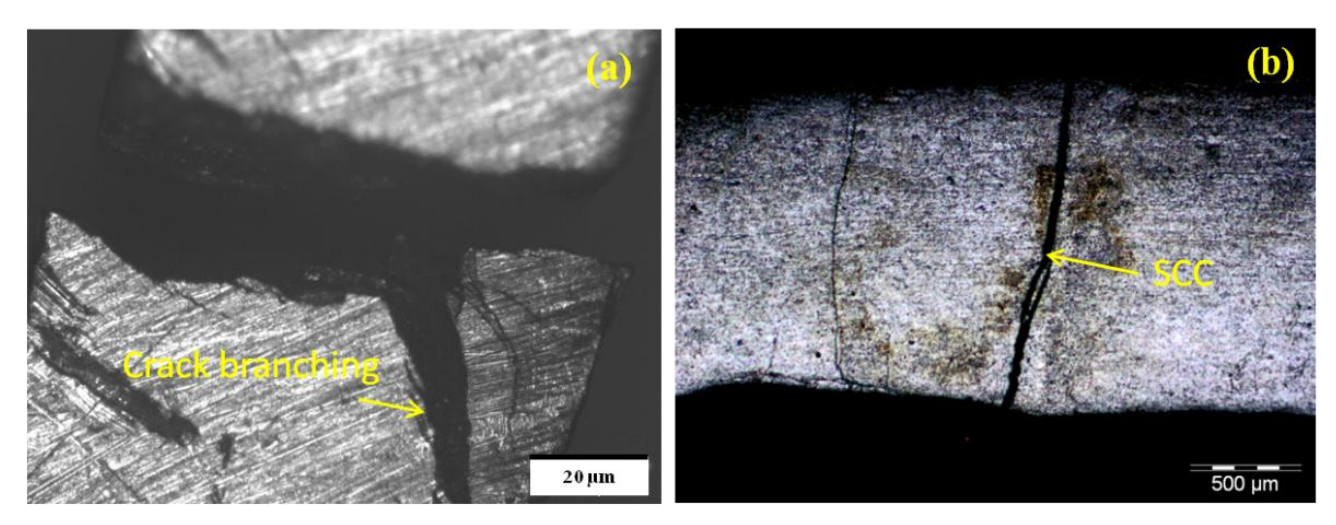


Figure 4.23 Optical micrographs of LBW weld after MgCl₂ test for 72 h. (a) surface and (b) cross section

4.2.2 Microstructural characterization of base material after $MgCl_2$ test for 5h, 10h, and 72h 4.2.2.1 Base material micrograph after $MgCl_2$ test for 5h

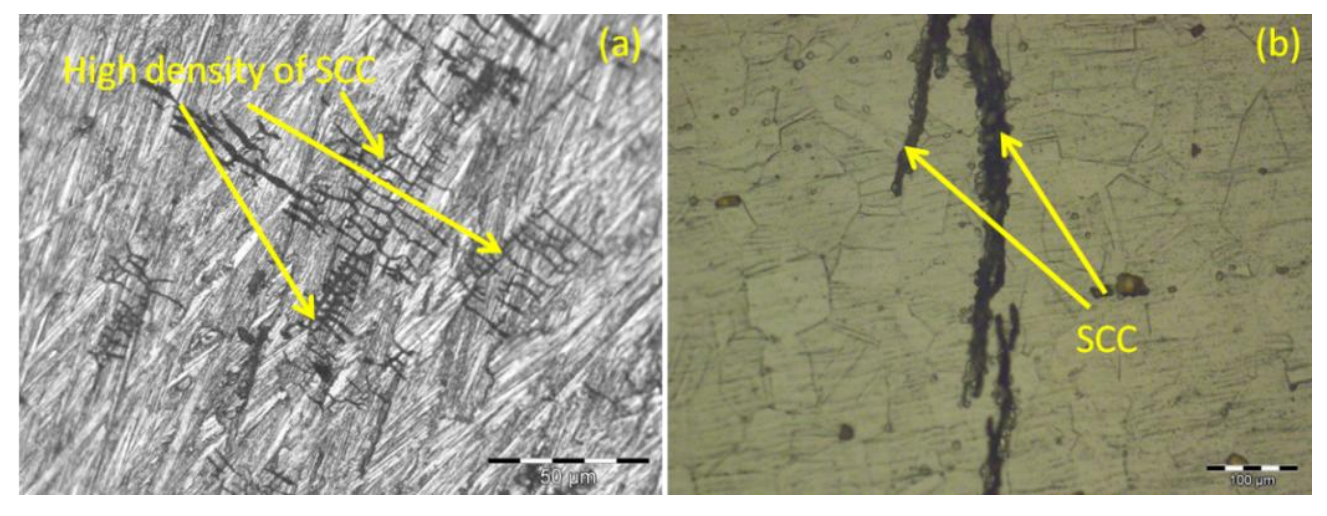


Figure 4.24 Optical micrographs of base material after boiling MgCl₂ test for 5h; (a) surface and (b) cross section

Figure 4.24 (a) and (b) shows micrographs of the base material after exposing it to boiling $MgCl_2$ solution after 5 h test, Figure 4.24 (a) shows SCC cracks with high density were formed. Group of crack with an average length of ~41 μ m on the surface of the base metal was observed after exposure

to test for 5 h. Figure 4.24 (b) shows the cross-sectional microstructure of base material after exposing the samples for 5 h.

4.2.2.2 Base material micrograph after MgCl₂ test for 10h

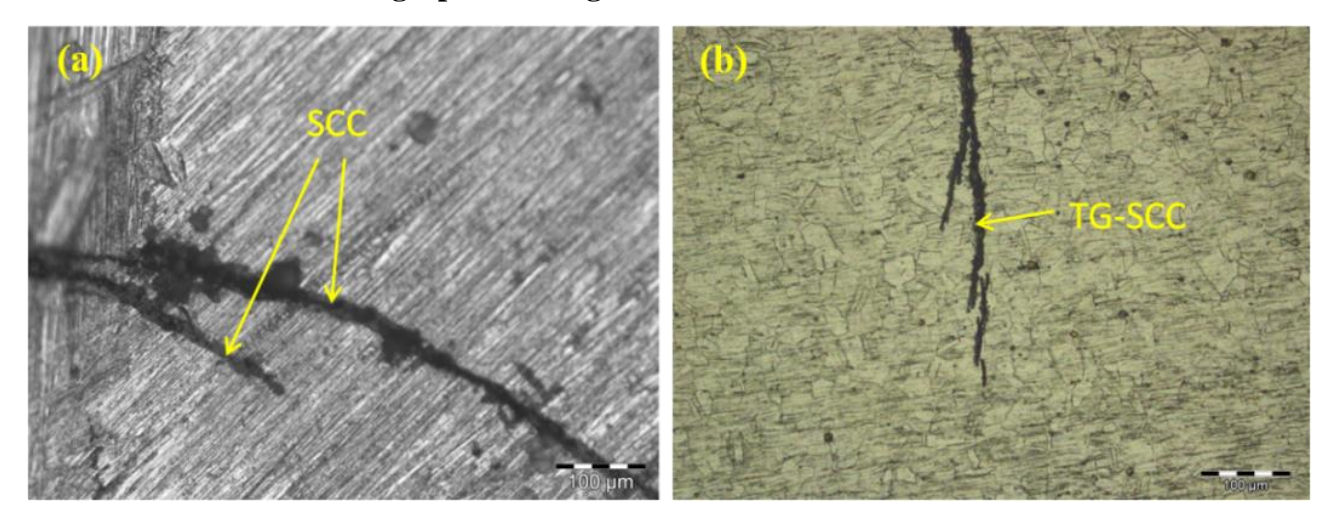


Figure 4.25 Optical micrographs of base material after boiling MgCl₂ test for 10h; (a) surface and (b) cross section

Figure 4.25 shows (a) surface and (b) cross-sectional optical micrograph of the base material after being exposed to boiling MgCl₂ solution for 10 h. The cracks were found to initiate on the surface and propagated into the bulk of the material.

4.2.2.3 Base material micrograph after MgCl₂ test for 72h

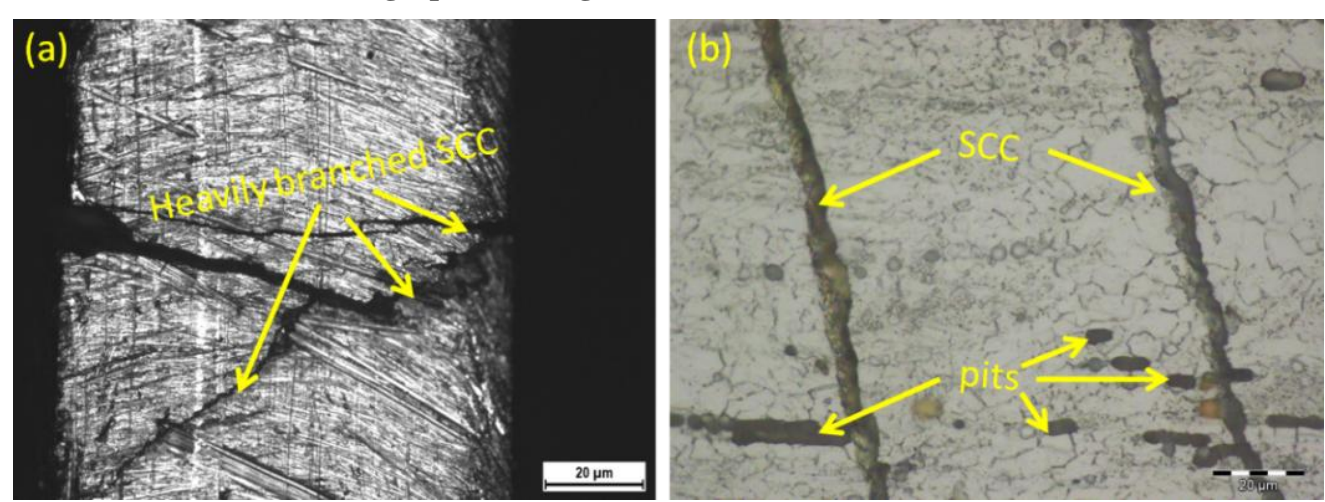


Figure 4.26 Optical micrographs of base material cross section after boiling MgCl₂ test for 72h Figure 4.26 shows the optical micrographs of base material after being exposed to boiling MgCl₂ solution for 72h. Figure 4.26 a) shows the sample which had undergone failure by SCC. Figure 4.26 b) shows the SCC cracks and pit formation.

4.2.3 Micro structural characterization of MIG weld specimen after MgCl₂ test for 5 h, 10 h and72h

4.2.3.1 Micrographs of MIG welded region after MgCl₂ test for 5h

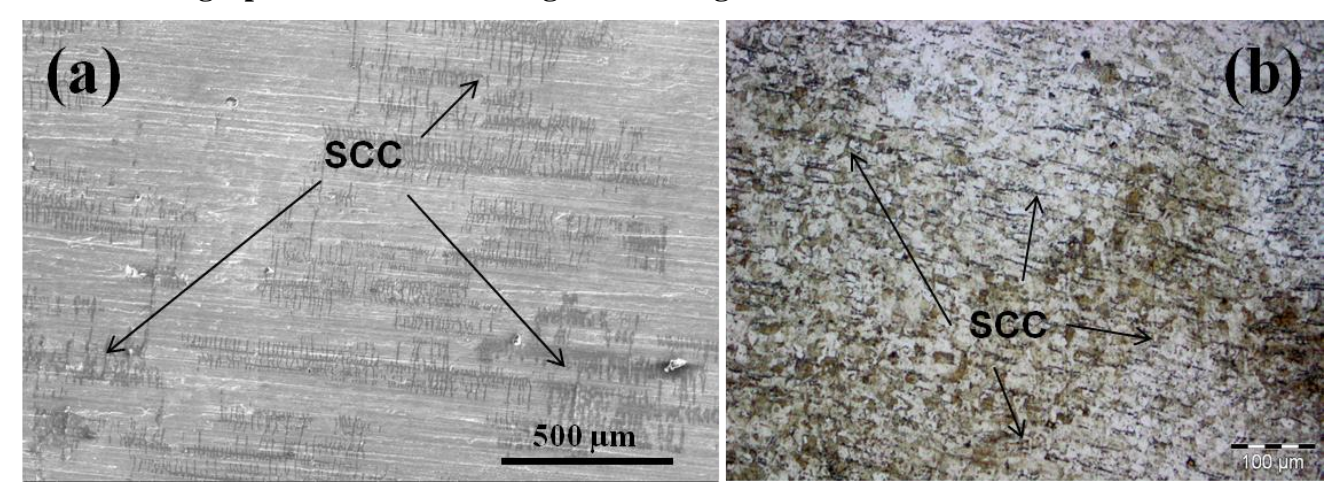


Figure 4.27 (a) FESEM micrographs of MIG welded tube surface and (b) optical micrograph of MIG welded tube cross section after exposing it to MgCl₂ test for 5h

Figure 4.27 (a) shows the FESEM micrographs of MIG welded tube after 5h MgCl₂ test. From micrographs, cracks with minimum density were observed in MIG welded samples when compared to LBW and base material micrographs. Figure 4.27 (b) shows the interface of the MIG weld with small SCC cracks formation along the deformation lines in the material.

4.2.3.2 Micrographs of MIG weld samples after MgCl₂ test for 10h

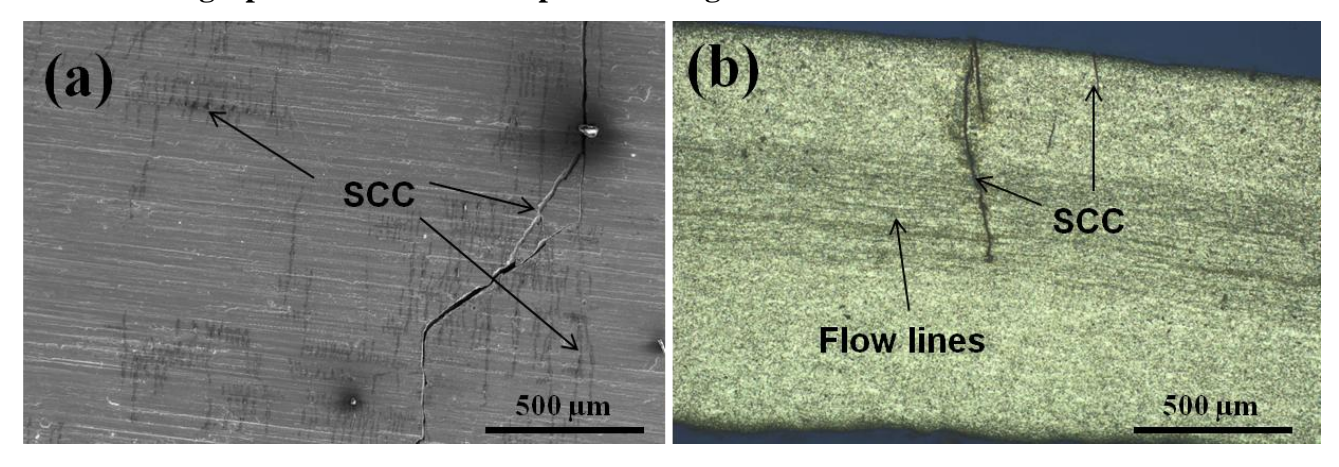


Figure 4.28 (a) FESEM micrographs of MIG welded tube surface and (b) optical micrograph of MIG welded tube cross section after boiling MgCl₂ test for 10h

Figure 4.28 shows the FESEM (a) and optical (b) micrographs of MIG welded tubes after exposing it to boiling MgCl₂ for 10 h. Samples of MIG welded tubes after polishing has shown low crack density and higher crack length when exposed for 10 h.

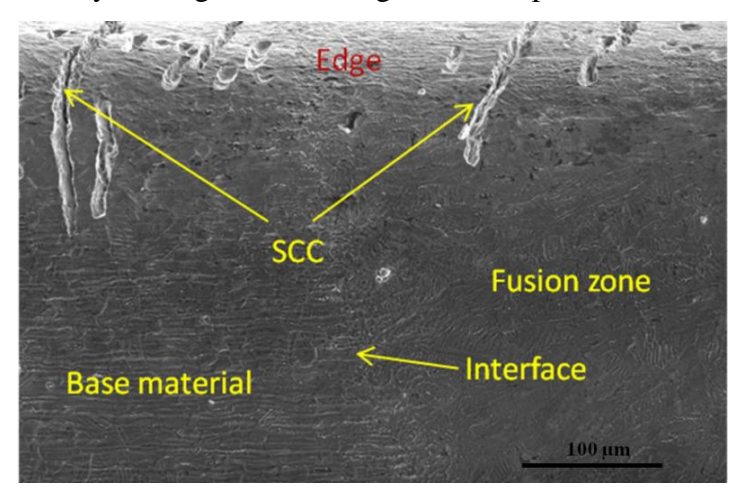


Figure 4.29 FESEM micrographs of MIG weld Cross section after MgCl₂ test for 10h Figure 4.29 shows the FESEM micrographs of MIG weld that revealed the presence of larger cracks originating from the surface and propagating into the bulk of the material. MIG welded samples have shown lower crack density when compared to LBW and spot welded samples.

4.2.3.3 Micrographs of MIG welded samples after MgCl₂ test for 72h

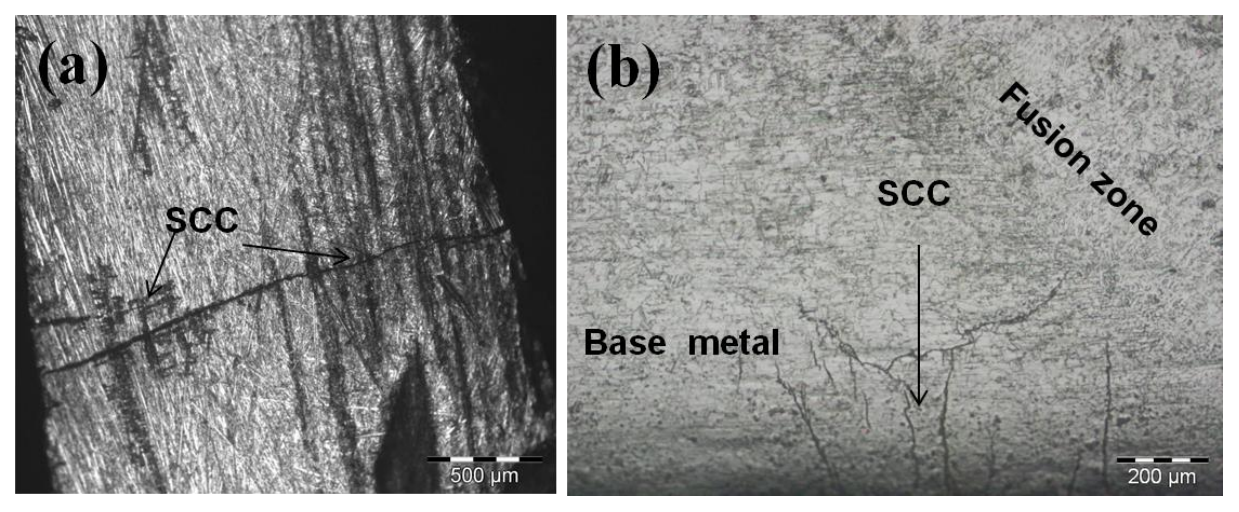


Figure 4.30 (a) and (b) are the optical micrograph of MIG weld cross section after MgCl₂ test for 72h.

The MIG welded samples (ring samples) were not completely break into two pieces even after prolonged exposure of 72 h. whereas, when compared with LBW, Base material and spot welded samples (ring samples) were completely broke into two pieces as shown in Figure 4.23 and Figure

4.26 and Figure 4.33 respectively. The crack density was higher in the MIG welded region and the HAZ zone of the specimen when compared with the base material micrographs. It was also observed that the carbides and the deformation lines were responsible for the crack formation. Optical micrograph of MIG welded samples after exposing to MgCl₂ solution for 72 h is shown in Figure 4.30.

4.2.4 Micro structural characterization of Spot welded region of the tubes after $MgCl_2$ test for 5 h, 10 h, and 72 h

4.2.4.1Spot welded region of the tubes after MgCl₂ test for 5 h

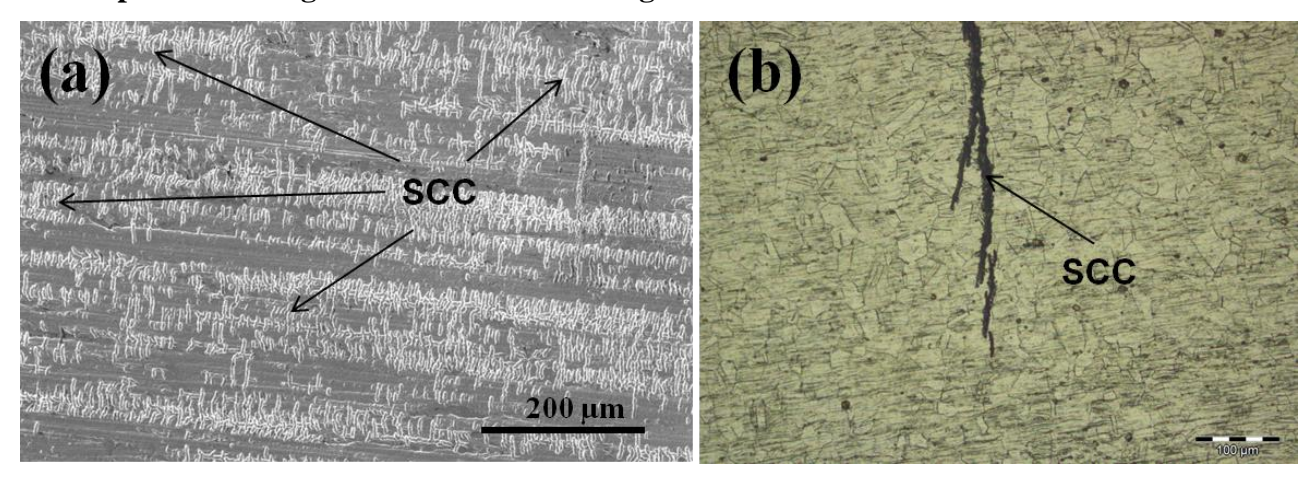


Figure 4.31 (a) FESEM micrograph of the spot welded region surface and (b) Optical micrograph spot welded region cross section of the tube after MgCl₂ test for 5 h

Figure 4.31 (a) and (b) represents the FESEM micrograph and optical micrograph of spot welded region of the tubes after $MgCl_2$ test for 5 h respectively. From the micrograph, it was observed that the surface had a high density of cracks. Wherein, the cross sectional optical micrograph of the same has shown transgranular SCC cracks.

4.2.4.2 Spot welded region of the tubes after MgCl₂ test for 10h

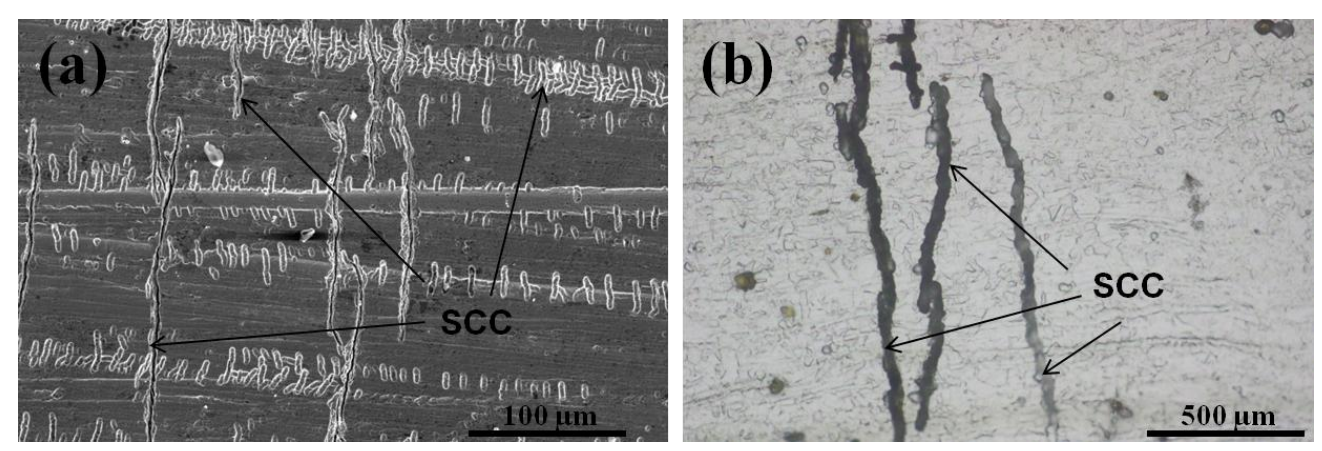


Figure 4.32 (a) FESEM micrograph of Spot welded region surface and (b) optical micrograph Spot welded region cross section of the tubes after MgCl₂ test for 10 h

Figure 4.32 (a) and (b) represents the FESEM micrograph and optical micrograph of spot welded region of the tubes after MgCl₂ test for 10 h respectively. In comparison to the sample treated for 5h, the smaller cracks in the 10 h treated sample coalesce to from larger cracks. These coalesced larger cracks were clearly evident from the optical micrograph as shown in Figure 4.29 (b).

4.2.4.3 Spot welded region of the tubes after MgCl₂ test for 72 h

Figure 4.33 shows the optical micrograph of spot welded region of the tubes after MgCl₂ test for 72 h. After exposure of the sample for 72 h, the crack has been propagated to a maximum extent which resulted in failure of the sample. The failure was caused due to the presence of high tensile residual stresses on the spot weld region. This failure can be correlated to the presence of chloride environment and residual stresses, under this condition the rate of crack propagation increases drastically. This failure of spot welded region was comparable with the LBW and base metal after undergoing identical experimental conditions.

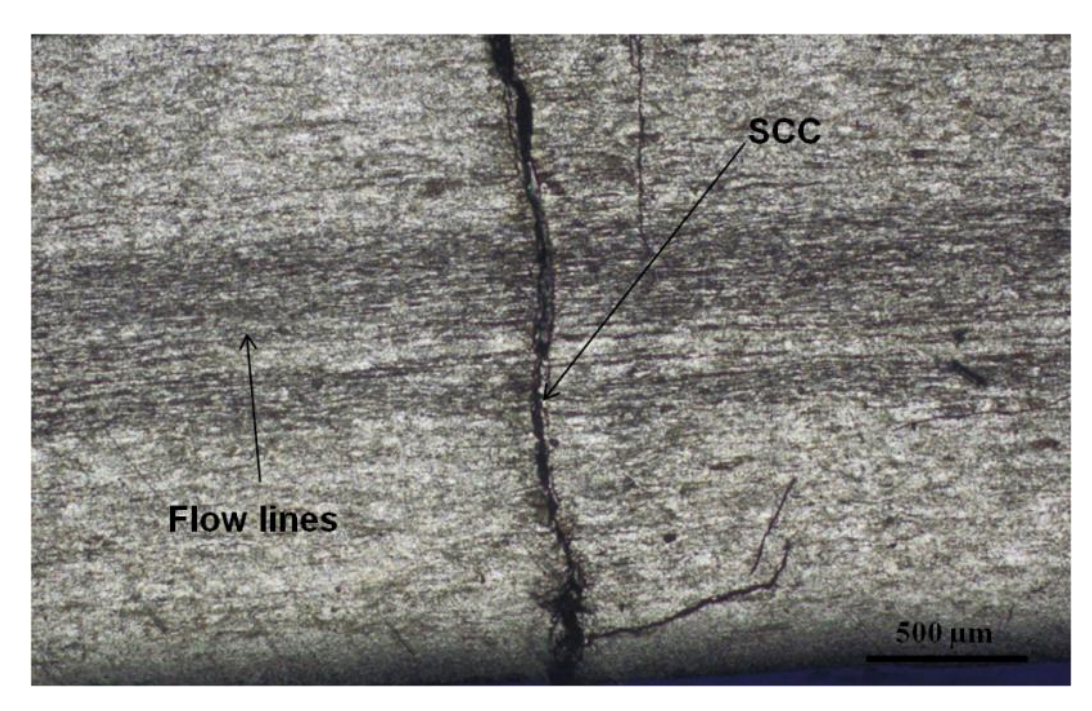


Figure 4.33 Optical micrograph spot welded region of the tubes after MgCl₂ test for 72 h

4.2.5 After post weld heat treatment micro structural characterization of LBW, MIG, base metal specimens after 5 h MgCl₂ test

Figure 4.34 shows the FESEM surface micrographs of a) LBW b) base metal and c) MIG after 5 h boiling MgCl₂ test, these samples were post weld treated. There was no SCC seen on surface as well as cross section micrographs shown in Figure 4.33 (d,e,f). Because of the post weld heat treatment residual stresses present in the material were relieved.

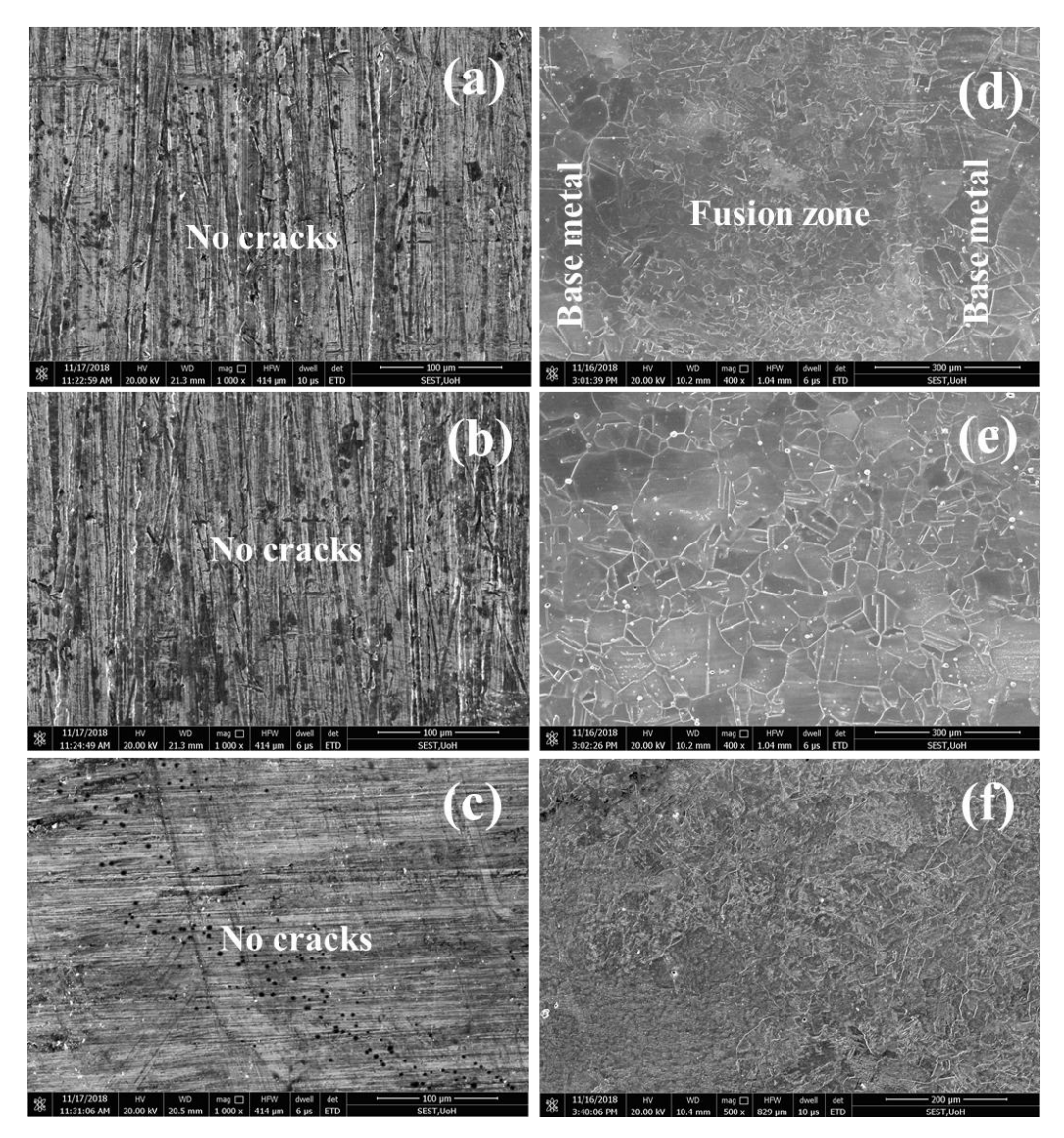


Figure 4.34 FESEM Surface micrographs of a) LBW, b) Base metal and c) MIG and (d, e, f) shows the cross sectional micrographs of LBW, Base metal and MIG respectively After 5 h MgCl₂ test

Summary of Part-II

The AISI 321 stainless steels (SS) tubes were subjected to SCC susceptibility test by using boiling MgCl₂ with varying time durations. All the welded and base metal samples were found to be susceptibile to SCC due to presence of high residual stresses in the material. The crack density and crack length were found to be higher in LBW and spot welded regions when compared to MIG welds. The crack length and crack density were increased with increase in exposure time. More over the post weld heat treated samples shows no crack formation after 5h boling MgCl₂ test. after post weld heat tretment residual stress present in the material is completely revolved. It is evident that the as resived weld tubes cantians tensile residual stress above the threshlod limeit.

4.3 PART-III: Surface engineering of welded tubes of AISI 321 SS for preventing chloride induced SCC

The outer and inner surface of AISI 321 tubes containing the LBW, spot weld, and MIG welds were subjected to buffing by using conventional buffing operation. After buffing, the samples were subjected to SCC test for different time durations. The buffed surface did not show SCC cracks on the outer surface as well as on the inner surface. The outer and inner surfaces of the 321 SS tube containing the welds (LBW, MIG, Spot welds) were also subjected to buffing operation. After buffing, the specimens were tested for SCC in boiling MgCl₂ for 5 h and 24 h. Microstructural characterization of the samples revealed that no cracks had been formed on the buffed surfaces of the welds on exposure to boiling MgCl₂. The detailed results and discussion are given below.

4.3.1 X-ray diffraction

The X-ray diffraction patterns of LBW, MIG welded, and base material in buffed and un-buffed conditions is shown in Figure 4.34. The phases present in 321 SS in different conditions were matched and confirmed from Joint Committee on Powder Diffraction Standards (JCPDS) data. Standard austenitic peaks of (111), (200), (220), (311) and (222) diffraction were detected in each case. Delta ferrite peaks (110) and (211) were found to be present in the base material, MIG welded and LBW samples in un-buffed condition. However, the samples in the buffed condition had shown the presence of only austenite phase. The peak broadening was analyzed in each case by determining the full width at half maximum (FWHM) as given in Table 4.3. Peak broadening can arise due to a) grain refinement and/or b) the presence of plastic strain in the matrix. Figure 4.35 shows that the XRD spectra of buffed surfaces (LBW, MIG welded and base material) were much sharper when compared to the XRD spectra of un-buffed surfaces. Both the peak broadening phenomena and the presence of delta ferrite in 321 SS in un-buffed condition confirmed the presence of plastic strain in the matrix. The buffed surfaces, on the other hand, have reduced plastic strain on the surface when compared to the surfaces in un-buffed condition; results are tabulated in table 4.3. The reason being that buffing technique involves polishing on the surface of the steel with a fine abrasive wheel which removed the highly strained layer on the surface without inducing additional strain in the matrix. Additionally, buffing imparted compressive stresses on the surface of the steel together with a reduction of surface roughness which is beneficial in increasing the SCC resistance of the steel.

Table 4.3 FWHM in buffed and un-buffed 321 SS

Sample	FWHM un-buffed condition	FWHM in buffed condition
LBW	0.322	0.124
MIG	0.267	0.108
Base material	0.242	0.163

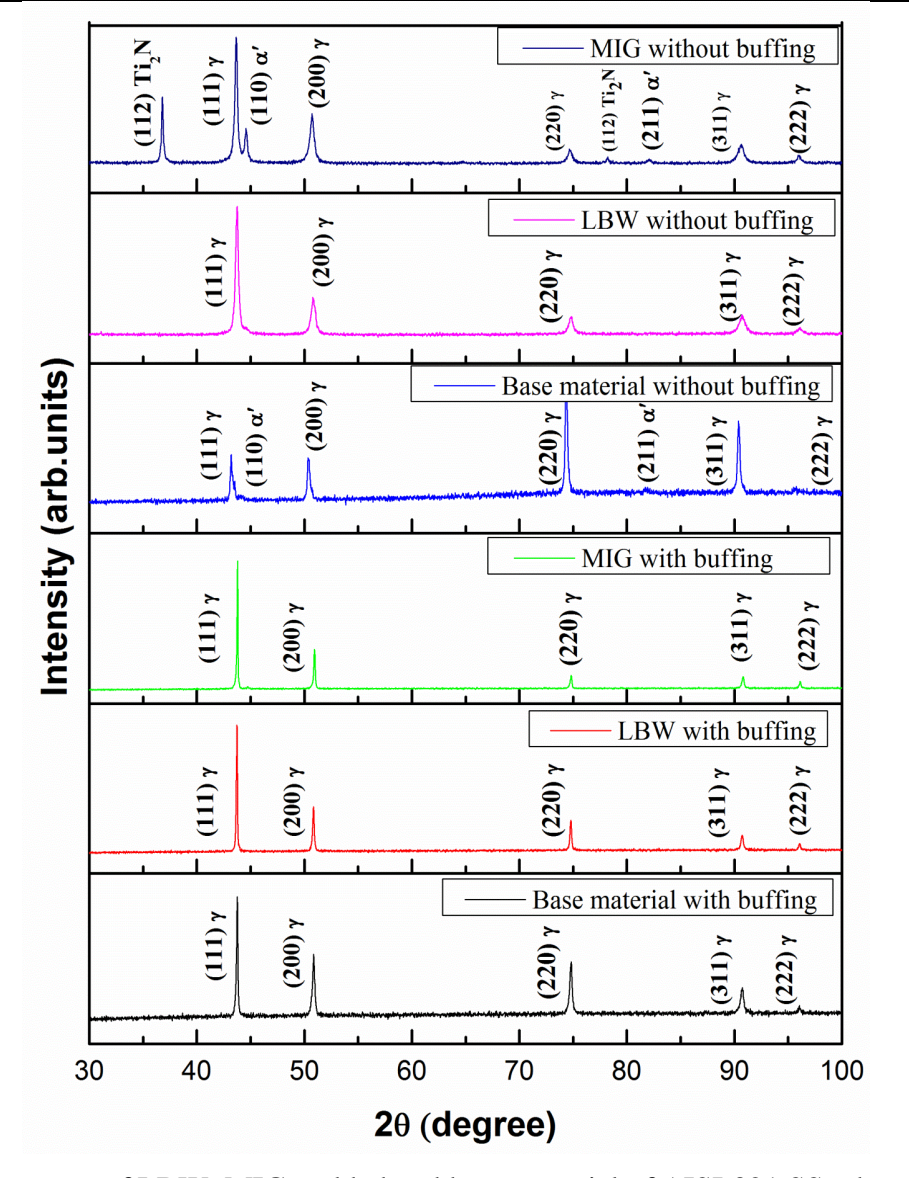


Figure 4.35 XRD pattern of LBW, MIG welded and base material of AISI 321 SS tubes in buffed and un-buffed condition.

4.3.2 Surface roughness

The surface roughness of LBW, MIG welded and base material was measured by using surface profilometer. The average surface roughness obtained in buffed and un-buffed condition on the weld specimens were tabulated in Table 4.5 and Table 4.5. As observed from Table 4.4, the surface roughness was reduced significantly as a result of buffing operation. The reduction of surface roughness reduces the depth of the troughs formed on the surface and hence prevents the accumulation of aggressive ions from the service environment in the troughs [105], which otherwise can enhance the phenomena of crack initiation.

Table 4.4 Average surface roughness of un-buffed surfaces of 321 SS for LBW, MIG welded and base material

Surface condition	Type of weld	Ra (µm)
	LBW	1.34
Without buffing	MIG welded	1.14
	Base material	1.74

Table 4.5 Average surface roughness of the buffed surfaces of 321 SS for LBW, MIG welded and base material

Surface condition	Type of weld	Ra (µm)
	LBW	0.77
With buffing	MIG welded	0.45
	Base material	0.94

4.3.3 Microhardness

The hardness profile was measured across the cross section of the 321 SS tube after buffing as shown in Figure 4.36. After buffing, the weld and base material samples have shown almost same hardness values with a tolerance of ~ 10 HV.

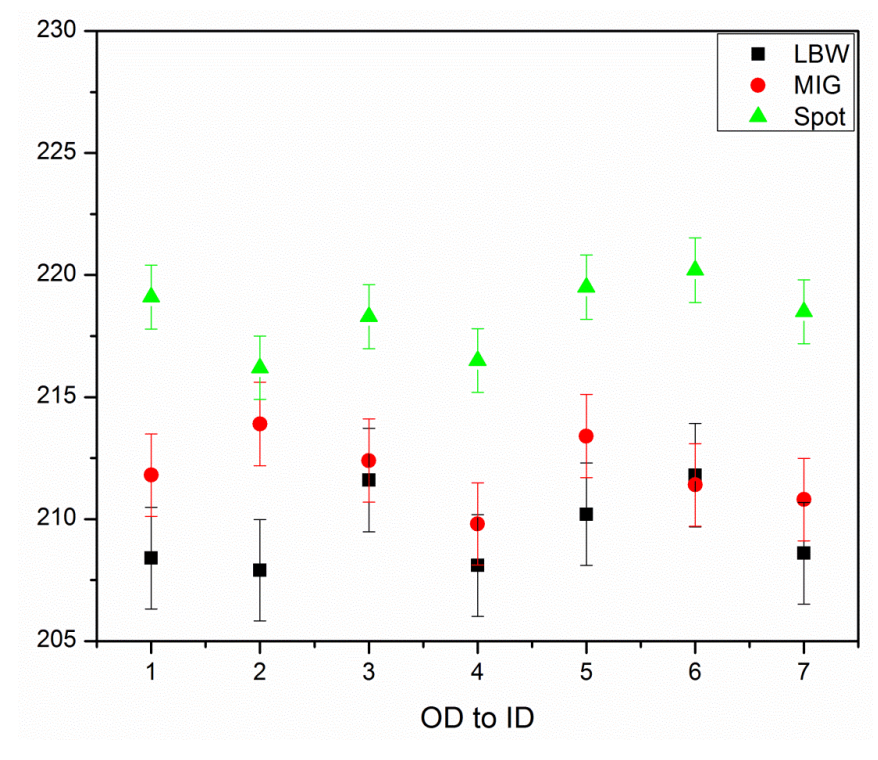


Figure 4.36 Hardness profiles of the different weld joints of AISI 321 SS tubes after a buffing operation

4.3.4 SCC susceptibility studies on LBW, MIG, spot weld and base metal of AISI 321 SS tubes after buffing

Extensive cracking has taken place in all the samples after exposing them to boiling MgCl₂ for 5 h, 10 h, and 72h. The occurrence of cracks indicated that the residual stress levels in the welds were above the threshold limit. It was found that the crack propagation was increased with increase in time when the samples were exposed for 5h and 10h. After exposing the samples to 72 h, the sample was found to be broken in the weld zone and base metal zone in both the spot weld and LBW specimens. No failure was observed in MIG welded samples. The cracking was transgranular in nature, which is a characteristic feature of chloride induced SCC in SS. However, the 321 SS tube has shown peculiar behavior with no signs of SCC in buffed condition when exposed to boiling MgCl₂. A comparison of the attack on the exposed surfaces of LBW, MIG, spot weld and base

material of the SS tubes in buffed and un-buffed condition after SCC tests are shown in Figure 4.37 (a-d), Figure 4.38 (a-d), Figure 4.39 (a-d) and Figure 4.340 (a-d) respectively. Microstructural characterization of the buffed surfaces of LBW, MIG welded and base material samples have shown no signs of cracking even after exposing them for 10 h in boiling MgCl₂. Whereas, the same sample had experienced severe SCC in a chloride environment in un-buffed condition. The SCC experiments were repeated to confirm the observations in case of MIG welded, LBW and the base material of 321 SS. Hence the study establishes that the SCC resistance of the surface of 321 SS welds in different condition increases as a result of buffing operation. The mechanism of increase of SCC resistance from the present study is as follows: Buffing operation a) induces compressive stresses on the surfaces, b) creates smoother surfaces and c) removes the highly strained surface by polishing without inducing any additional strain which hinders the phenomena of crack initiation. The presence of a strained microstructure also results in localized stress assisted dissolution leading to early crack initiation. SCC results from the synergistic effect of three factors, namely, (a) susceptible material (surface condition, microstructure), (b) aggressive environment and (c) presence of tensile stresses. Welds are associated with a high magnitude of tensile residual stresses together with a plastic strain on the surface. It is difficult to alter either the material condition or the service environment for components in an industrial application. However, if the tensile stresses present on the surfaces can be converted into compressive stresses SCC can be avoided to a large extent. The buffing operation had done this by converting the tensile stresses present on the surface of the component into compressive stresses together with a reduction in the surface roughness which results in increasing the resistance to SCC. A similar observation has been made by the authors in their previous study on the susceptibility of 304 L SS to SCC under different surface finished condition [9,22]. Moreover, buffing being a simple, portable and economic technique can be easily incorporated as the last stage of fabrication of industrial components.

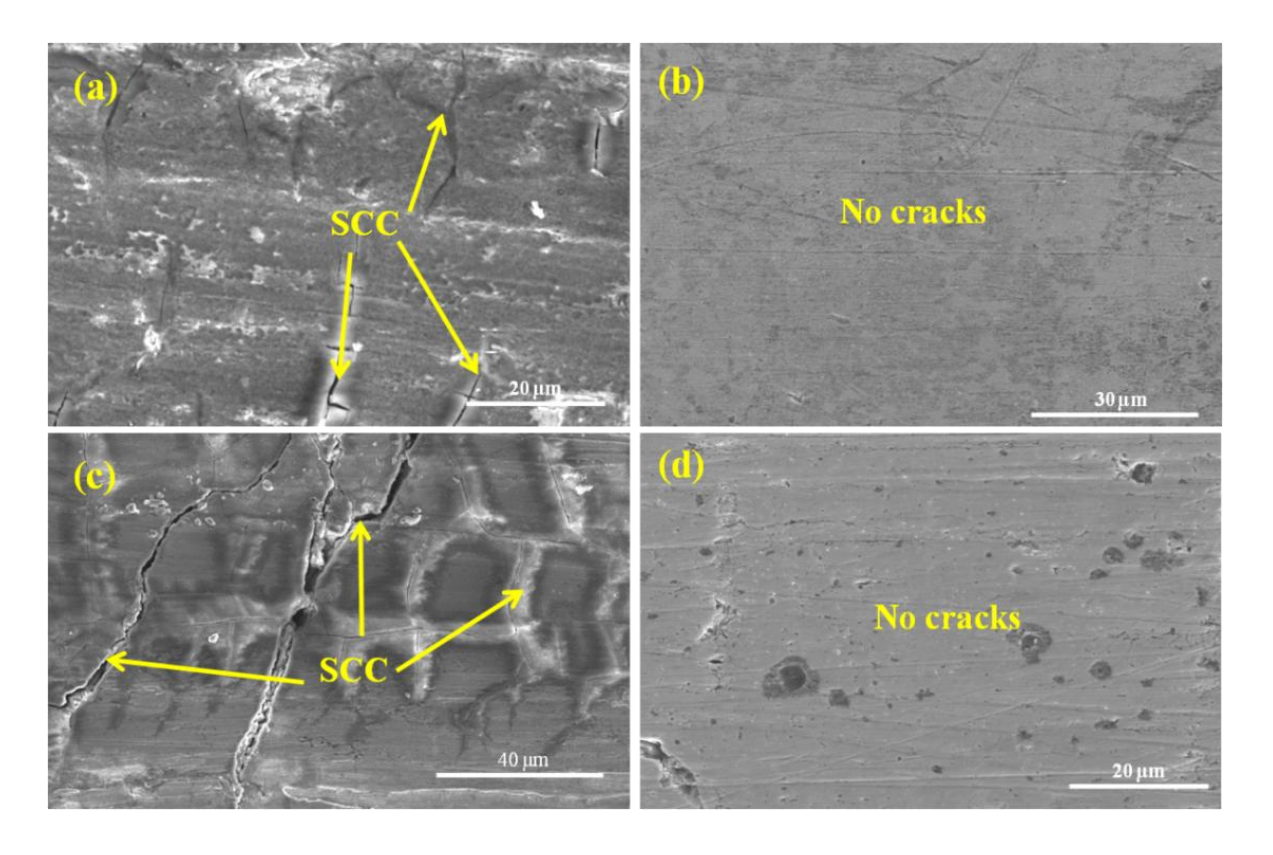


Figure 4.37 FESEM micrographs of the surface of LBW 321 SS in buffed and un-buffed condition after SCC tests (a) un-buffed; 5 h exposure (b) buffed; 5 h exposure, (c) un-buffed; 10 h exposure and (d) buffed; 10 h exposure

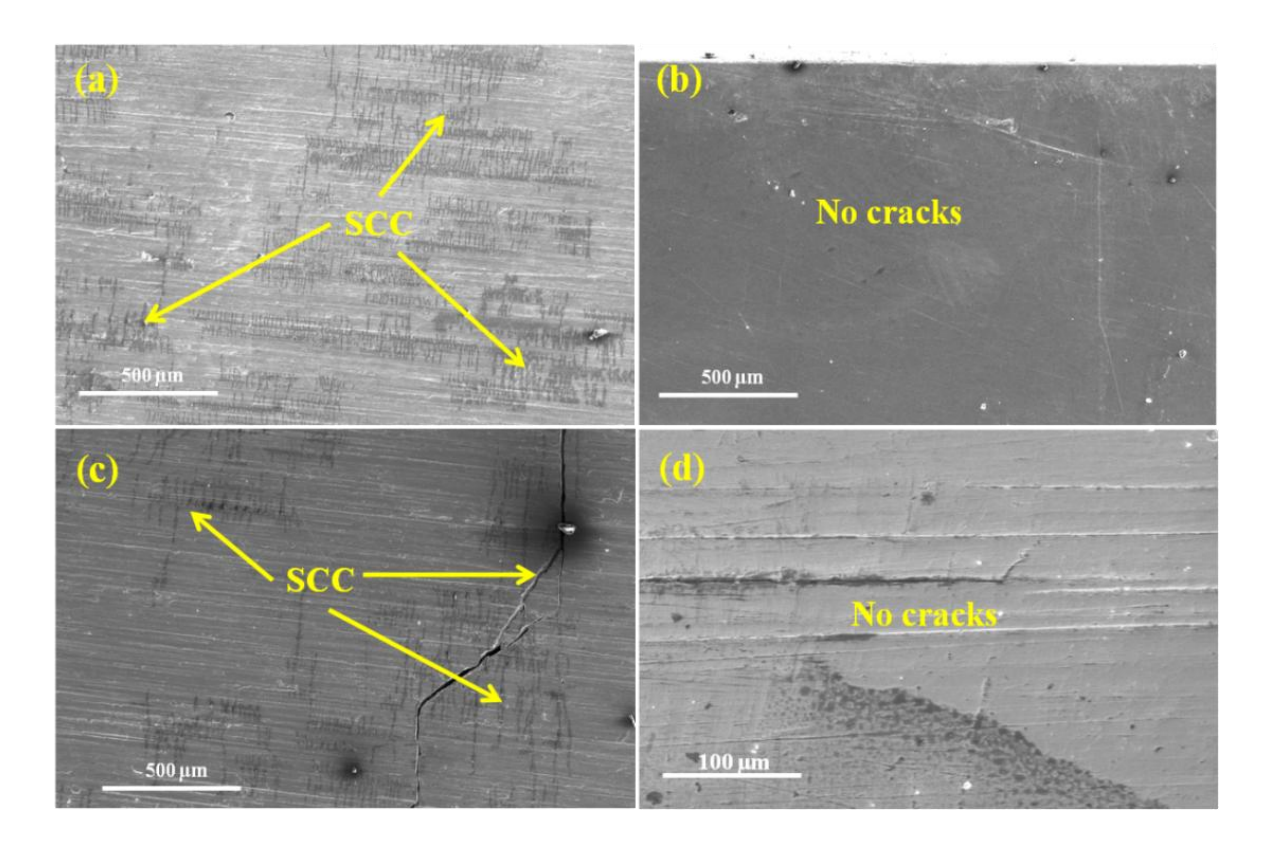


Figure 4.38 FESEM micrographs of the surface of MIG 321 SS in buffed and un-buffed condition after SCC tests (a) un-buffed; 5 h exposure (b) buffed; 5 h exposure, (c) un-buffed; 10 h exposure and (d) buffed; 10 h exposure

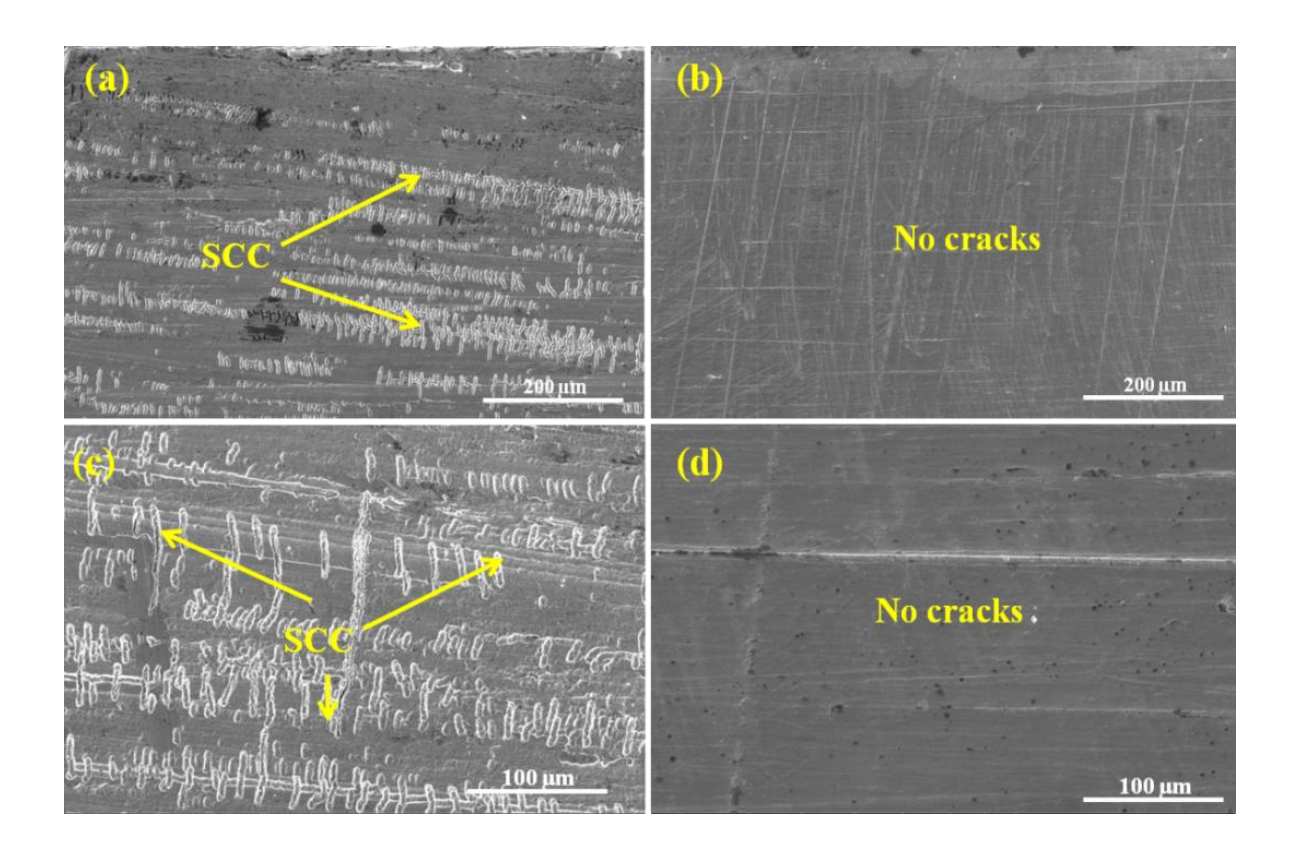


Figure 4.39 FESEM micrographs of the surface of spot weld 321 SS in buffed and un-buffed condition after SCC tests (a) un-buffed; 5 h exposure (b) buffed; 5 h exposure, (c) un-buffed; 10 h exposure and (d) buffed; 10 h exposure

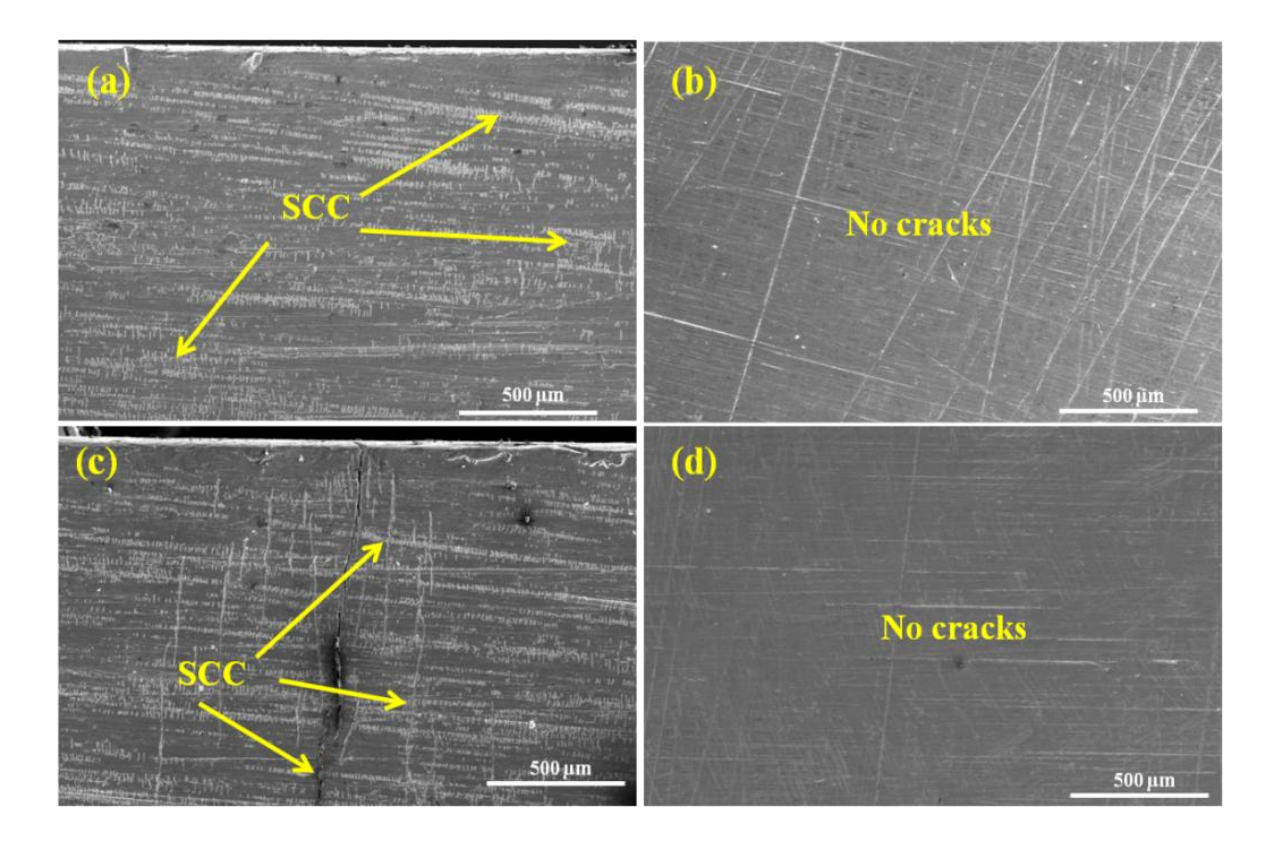


Figure 4.40 FESEM micrographs of the surface of the base material 321 SS in buffed and un-buffed condition after SCC tests (a) un-buffed; 5 h exposure (b) buffed; 5 h exposure, (c) un-buffed; 10 h exposure and (d) buffed; 10 h exposure

SUMMARY (PART-III)

The ring-shaped samples of AISI 321 SS tubes in buffed and un-buffed conditions were subjected to boiling MgCl₂ test for 5h and 10h. The results obtained are summarized below.

- 1. The unbuffed samples have exhibited high surface roughness and tensile residual stresses which resulted in SCC.
- 2. Whereas, samples in buffed condition have lower surface roughness. The buffing operation induced compressive residual stresses due to which the susceptibility to SCC was reduced.
- 3. After boiling MgCl₂ test, the buffed samples have shown no cracks on the surface but severe cracking was observed on the unbuffed samples.
- 4. Buffing being a simple, portable and economic method can be adopted by the industries even for existing components for eradication of chloride induced SCC.

4.4 PART-IV: Mechanistic understanding of the improvement in SCC resistance of buffed AISI 321 SS welded tubes

Figure 4.41 shows the classical three circle diagram for stress corrosion cracking (SCC) explaining the factors responsible for cracking. SCC is a phenomenon that occurs under the synergistic action of stress, environment, and susceptible material/ surface. Hence in order to prevent SCC, the stress in material and the material surface that is exposed to the corrosive environment need to be closely controlled. The stresses responsible for SCC are tensile in nature. Tensile residual stresses arise in the material due to different steps involved during component fabrication. Welding is one such stage during the component fabrication which invariably induces tensile residual stresses in the material that may cause premature failure of the component.

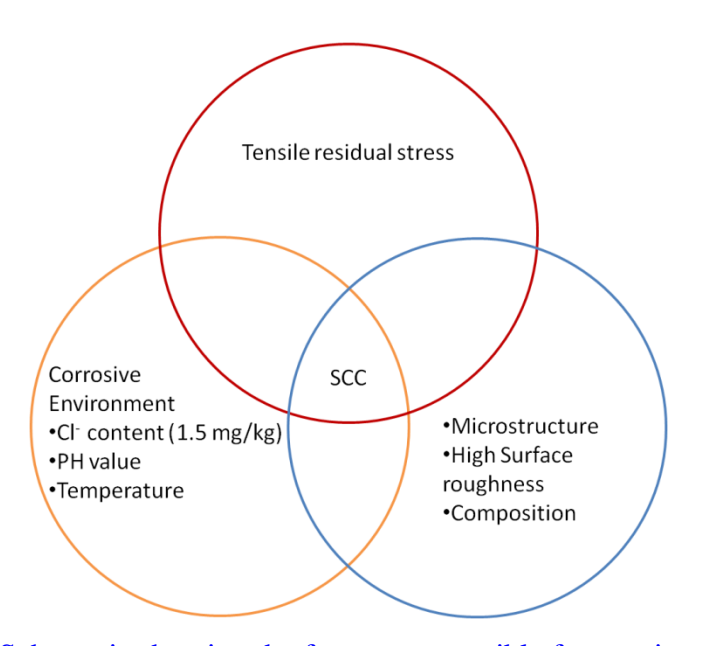


Figure 4.41 Schematic showing the factors responsible for causing SCC

Surface finishing is the final stage in the industrial fabrication process. General surface finishing techniques like machining, grinding, wire brushing, shot peening etc. are used during the manufacturing of components. Surface preparation operations can alter the susceptibility of steel to SCC and its resistance to the initiation and propagation of pitting. Surface finishing operations affect predominantly the surface layers of a component and stress-corrosion cracks initiate from the surfaces. Surface roughness also has a significant effect on stress-corrosion crack initiation [105]. Greater is the surface roughness, higher is the number of grooves. When this surface is exposed to an aggressive chloride environment, the chloride ions get accumulated in the grooves leading to SCC.

General surface finishing techniques like milling, turning, grinding etc. induce high magnitude of tensile residual stresses [72, 73] and high density of deformation bands which result in enhanced susceptibility to chloride environment.

Hence in order to prevent stress corrosion cracks, we need to have careful control over both the 'stress' and the 'material/surface' parameters. In some particular industrial application, the environment to which the material is exposed remains fixed. The schematic of the tensile residual stress converting into compressive residual stress is shown in Figure 4.42. The surface roughness of the samples is minimized which helps in reducing the susceptibility to SCC.

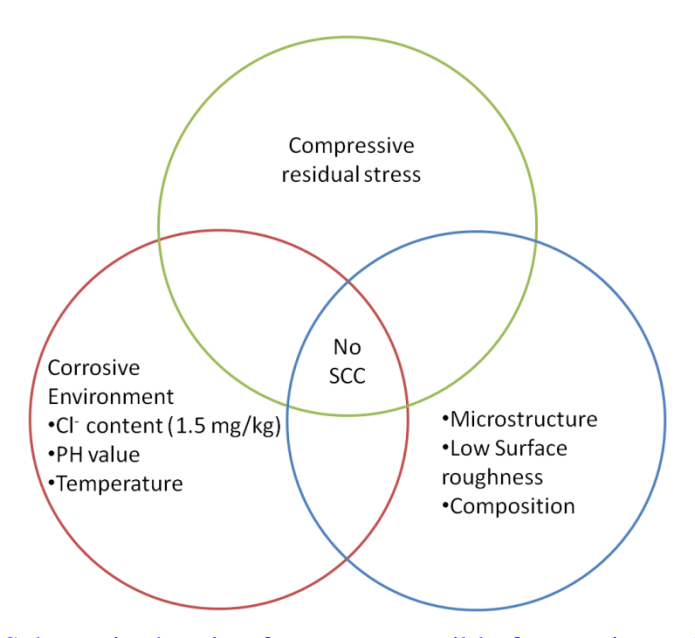


Figure 4.42 Schematic showing factors responsible for causing reducing SCC

Figure 4.42 shows the schematic of the buffing operation. It involves rotation of a grinding wheel with a particular velocity on the surface of the work piece. The wheel was also rastered over the surface thereby a) imparting compressive stresses and b) lower surface roughness. Table 4.6 shows that the residual stress present on the surface is compressive in nature. To compare other processes like Shot peening and laser peening also induce the compressive residual stresses but incorporate high plastic strain in the material and final surface roughness also high, Buffing is also low-cost operation. Buffing is a very common practice in industrial manufacturing units which is applied to achieve desired surface finish. Several assemblies and flexible attachments are used in industries for carrying out buffing of inner surface of the tubes having small diameters as show Figure 4.44.

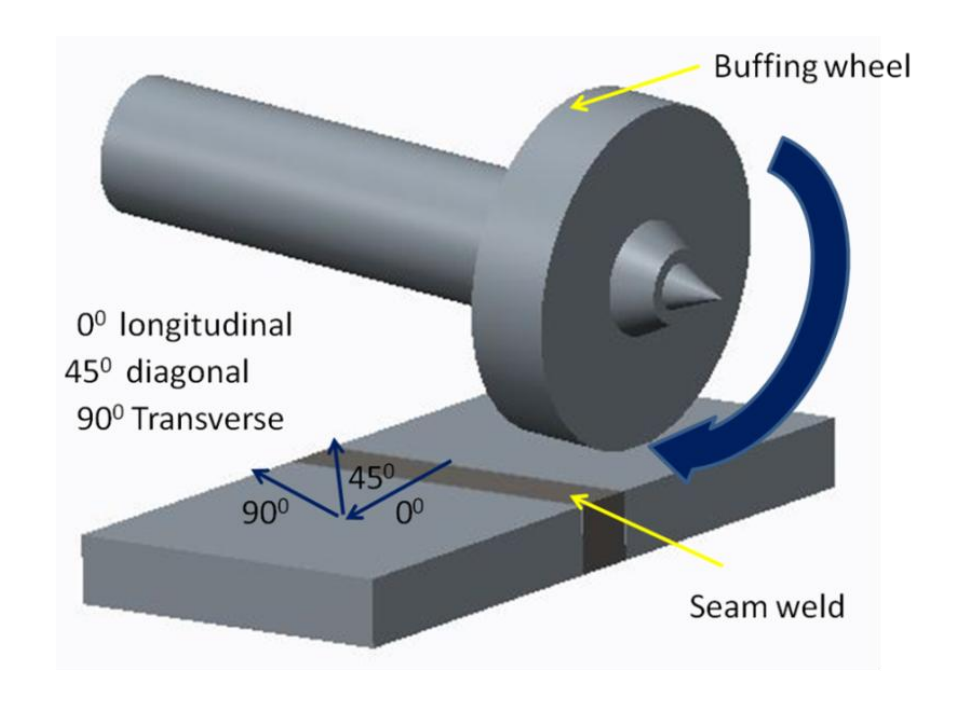


Figure 4.43 Schematic of the buffing operation

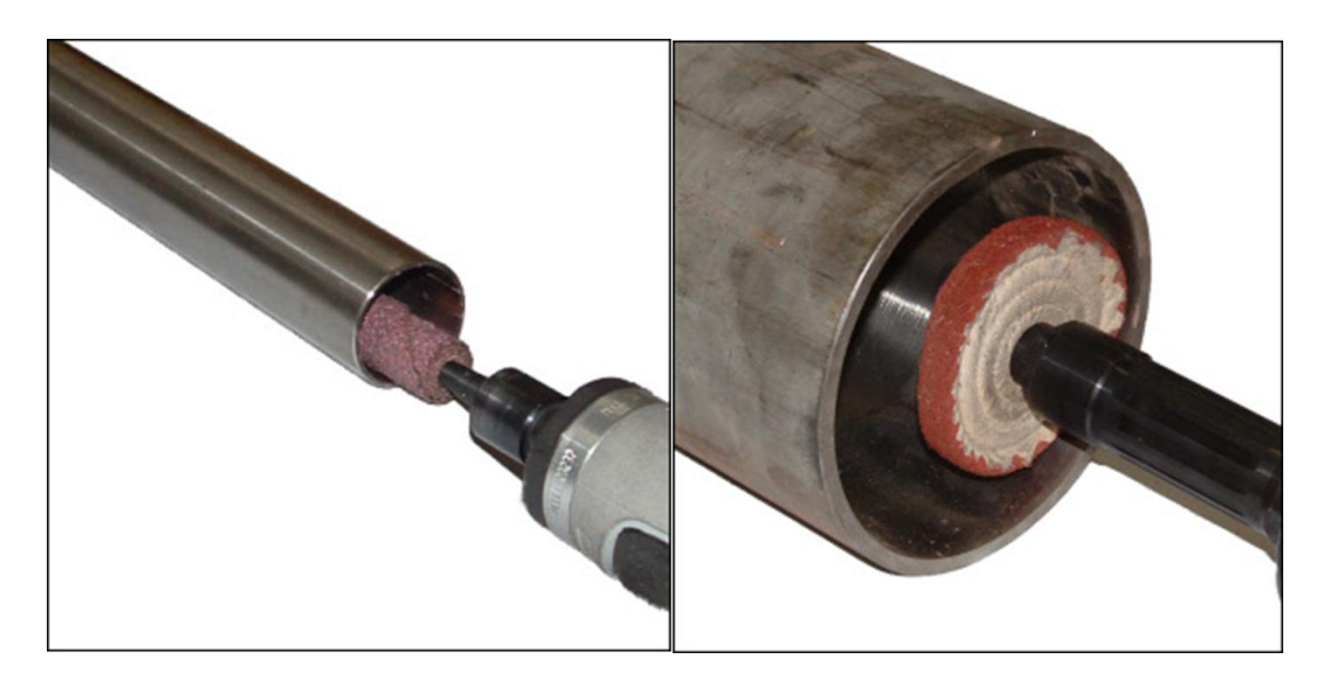


Figure 4.44 Schematic of the buffing operation for inner surface of the tube [106-107]

Table 4.6 Residual stress measurements on the surface of AISI 321 SS tube weld after buffing.

Sample ID and	Residual stresses along two directions (MPa)	
location	0 °	90°
1- LB weld	-287±16	-351±13
2- LB weld	-284±17	-342±6
1-Spot weld	-351±17	-433±24
2-spot weld	-382±23	-368±7
MIG weld	-348±15	-385±12
Base material	-239±23	-306±57

CHAPTER 5

5.0 CONCLUSIONS

The study involved root cause analysis of the failure of AISI 321 stainless steel used in solar thermal power plant. These failed tubes were seam welded using a) laser beam welding in one case and b) MIG welding in another case together with spot welding on the surface. The work involved characterization of the welded tubes to understand the root cause of the failure. The work was extended to find an effective and simple surface engineering method to prevent such failures in the future. The following are the conclusions made from the study presented in this thesis:

- a) Hairline cracks were detected by dye penetrant tests. These cracks led to the leakage of the thermic fluid from the tubes causing failure.
- b) The spot welded, laser beam welded and MIG welded tubes had tensile residual stresses (due to constrained weld geometry) beyond the threshold limit which led to extensive SCC on exposure to boiling MgCl₂. Appropriate post weld heat treatment is required to avoid such failures in the future.
- c) Laser beam welded; metal inert gas welded and the base material of AISI 321 SS in buffed condition did not undergo SCC. Hence buffing made AISI 321 SS welds resistant to chloride induced SCC.
- d) Buffing operation on the surface of 321 SS imparted a high magnitude of compressive residual stresses together with a reduction of surface roughness. The presence of compressive stresses on the surface together with reduced roughness prevented crack initiation on the buffed surfaces in the presence of chloride ions.

Scope of future work

- ➤ Long term sustainability of compressive residual stress induced due to buffing.
- > Cross –sectional analysis of the depth up to which compressive residual stresses are generated in the material due to buffing operation
- ➤ Comparison of Laser peening, shot peening techniques and buffing for mitigation of SCC

REFERENCES

- [1] S.M.E.S.M. Elsariti, and and Haftirman, Behaviour of stress corrosion cracking of austenitic stainless steels in sodium chloride solutions, Procedia Engineering 53 (2013) 650 654.
- [2] H. Shaikh, H.S. Khatak, P. Rodriguez, Stress corrosion crack growth behaviour of austenitic stainless steels in hot concentrated chloride solution, ICF10, Honolulu (USA), (2001).
- [3] L.-Z. Jin, The chloride stress-corrosion cracking behavior of stainless steels under different test methods, Journal of Materials Engineering and Performance 4(1) (1995) 734-739.
- [4] K.F. Wenqian Zhang, Yujin Hu,Siyang Wang,Xuelin Wang, Effect of machining-induced surface residual stress on initiation of stress corrosion cracking in 316 austenitic stainless steel, Corrosion Science 108 (2016) 173–184.
- [5] M.S. A. Contreras, A. Albiter, R. Galván, O. Vega, Assessment of stress corrosion cracking on pipeline steels weldments used in the petroleum industry by slow strain rate tests, Arc Welding, INTECH Open Access Publisher, Croatia, (2011), 127-150.
- [6] J.Ł.A.M.G. S. Topolska, Failure of austenitic stainless steel tubes during steam generator operation, Journal of Achievements in Materials and Manufacturing Engineering 55(2) (2012) 378-385.
- [7] K. El-Menshawy, M.M.A. Gad, A.A. El-Sayed, Effect of heat treatment and stabilizing elements on the localized corrosion behavior of some stainless steels, Proceedings of the 9 International Conference for Nuclear Sciences and Applications (13) (2008).
- [8] Y.F. Cheng, Stress corrosion cracking of pipelines, JohnWiley & Sons, Inc., Hoboken, New Jersey. (2013.
- [9] P.S. Kumar, S.G. Acharyya, S.V.R. Rao, K. Kapoor, Distinguishing effect of buffing vs. grinding, milling and turning operations on the chloride induced SCC susceptibility of 304L austenitic stainless steel, Materials Science, and Engineering: A, 687 (2017) 193-199.
- [10] Swati Ghosh, Vivekanand Kain, Microstructural changes in AISI 304L stainless steel due to surface machining: Effect on its susceptibility to chloride stress corrosion cracking, Journal of Nuclear Materials 403 (2010) 62–67.
- [11] Swati Ghosh, Vishav Preet Singh Rana, Vivekanand Kain, Vivek Mittal, S.K. Baveja, Role of residual stresses induced by industrial fabrication on stress corrosion cracking susceptibility of austenitic stainless steel, Materials and Design 32 (2011) 3823–3831.

- [12] V.S.R.A.T. Shoji, Stress corrosion cracking theory and practice, Woodhead Publishing Limited, Philadelphia, (2011).
- [13] Pardhu Yella, P. Venkateswarlu, Ramesh K. Buddu, D.V. Vidyasagar, K. Bhanu Sankara Rao, P. Prem Kiran, Koteswararao V. Rajulapati, Laser shock peening studies on SS316LN plate with various sacrificial layers, Applied Surface Science 435 (2018) 271–280.
- [14] O. Takakuwa, H. Soyama, Effect of residual stress on the corrosion behavior of austenitic stainless steel, Advances in Chemical Engineering and Science, 05 (2015) 62-71.
- [15] Kamal Mankari and Swati Ghosh Acharyya, Development of stress corrosion cracking resistant welds of 321 stainless steel in chloride environment by simple surface engineering, Applied Surface Science, 426, 2017, 944-950.
- [16] P. Peyre, X. Scherpereel, L. Berthe, C. Carboni, R. Fabbro, G. Beranger, C.Lemaitre, Surface modifications induced in 316L steel by laser peening and shot-peening. Influence on pitting corrosion resistance, Materials Science and Engineering: A, 280(2000) 294–302.
- [17] S. Bagherifard, R. Ghelichi, M. Guagliano, On the shot peening surface over age and its assessment by means of finite element simulation: a critical review and some original developments, Applied Surface Science, 259 (2012) 186–194.
- [18] K. Ding, L. Ye, Laser shock peening performance and process simulation, CRCPress, Cambridge England, (2006).
- [19] A.K. Gujba, M. Medraj, Laser peening process and its impact on materialsproperties in comparison with shot peening and ultrasonic impact peening, Materials, 7 (2013) 7925–7974.
- [20] M. Ramulu, S. Kunaporn, D. Arola, M. Hashish, J. Hopkins, Waterjet machining and peening of metals, Trans. ASME 122 (2000) 90–95.
- [21] E. Scheel, Jeremy & Hornbach, Doug & S. Prevey, Paul. Mitigation of stress corrosion cracking in nuclear weldments using low plasticity burnishing. Conference Paper (1. . 10.1115/ICONE16-48597),(2008).
- [22] Pandu Sunil kumar, Swati Ghosh Acharyya, S.V. Ramana Rao, Komal Kapoor, Surface buffing and its effect on chloride induced SCC of 304L austenitic stainless steel, International Conference on Advances in Metallurgy, Materials and Manufacturing, IOP Conf. Series: Materials Science and Engineering 314 (2018).

- [23] P.Marshall, "Austenitic stainless steels microstructure and mechanical properties", 1st Edition, 424.
- [24] Michael Mcguire, Stainless steels for design engineers ASM International Materials Park, Ohio 44073-0002, (2008).
- [25] J R Davis, Chapter 1 Introduction to Stainless Steels, Alloy Digest Sourcebook: Stainless Steels, ASM International, 1-6 (2000).
- [26] J. R. Davis Basic understanding of weld corrosion, corrosion of weldments ASM International (2006).
- [27] J. Swaminathan, R. Singh, M.K. Gunjan, B. Mahato, Sensitization induced stress corrosion failure of AISI 347 stainless steel fractionator furnace tubes, Engineering Failure Analysis 18(8) (2011) 2211-2221.
- [28] A Designers' Handbook Series No 9002, welding of stainless steels and other joining methods, Nickel Development Institute.
- [29] J. Charles, J.D. Mithieux, P.O. Santacreu, L. Peguet, The ferritic stainless steel family: the appropriate answer to nickel volatility, Metallurgical Research & Technology, 106 3 (2009) 124-139.
- [30] P Lacombe; B Baroux, Gérard Béranger, Louis Colombier, J Hochmann, Stainless steels, Les Ulis, France: Les Editions de Physique, (1993).
- [31] A.Rajasekhar, Heat treatment methods applied to aisi 431 martensitic stainless steels, International Journal of Scientific & Engineering Research, 6(4) (2015) 547-553.
- [32] H.S. Khatak, U Baldev Raj, Corrosion of austenitic stainless steels mechanism, mitigation and monitoring, Woodheapdub lishing limited Cambridge England, (2002).
- [33] Ramesh Singh, Chapter 6 Welding Corrosion-Resistant Alloys: Stainless Steel, Applied Welding Engineering (Second Edition) Processes, Codes, and Standards 2016, 239-262
- [34] A.J. Sedriks, Corrosion of Stainless Steels, John-Wiley and Sons, New York, USA, (1979).
- [35] Iris Alvarez-Armas Suzanne Degallaix-Moreuil, Duplex Stainless Steels, ISTE Ltd, and John Wiley & Sons, Inc, United States, (2009).
- [36] C.-O.A. Olsson, D. Landolt, Passive films on stainless steels chemistry, structure and growth, Electrochimica Acta 48 (2003) 1093-1104.
- [37] J.B. Lumsden, in Passivity of Metals, Eds. R.P. Frankenthal and J. Kruger, Corrosion Monograph Series, The Electrochemical Society, USA, (1978) 730-739.

- [38] A.J. Sedriks, Role of sulphide inclusions in pitting and crevice corrosion of stainless steels, International Metals Reviews, 28 (1983) 295-307.
- [39] T.SzauerJ.Jakobs, The pitting corrosion of low alloy and mild steels, Corrosion Science, 16, 12, (1976), 945-948
- [40] M. A. A. Tullmin and F. P. A. Robinson, Effect of Molybdenum Additions on the Corrosion Resistance of a 12% Chromium Steel, Corrosion -Houston Tx- 44(9):664-670 · September (1988).
- [41] U. Kamachi Mudali, R. K. Dayal, J. B. Gnanamoorthy, P. Rodriguez, Pitting Corrosion Studies on Nitrogen-Bearing Austenitic Stainless Steels, Materials Transactions, JIM/ 37, 10, (1996).
- [42] T. Sydberger, Werkstoffe and Korrosion, 32, 179,(1981).
- [43] U. Kamachi Mudali. R.K. Dayal, T.P.S. Gill, and J.B. Gnanamoorthy, Wcrkstoffe and Korrosion, 37, 637-643,(1986).
- [44] U. Kamachi Mudali, R.K. Dayal, J.B. Gnanamoorthy, and P. Rodriguez. Transactions of the IIM. SO, 37-47,(1997).
- [45] U. Kamachi Mudali, R.K. Dayal, J.B. Gnanamoorthy, and P. Rodriguez, Metallurgical Transactions A, 27 (1996), 2881-2887.
- [46] U. Kamachi Mudali, S. Ningshen, A.K. Tyagi, and R.K. Dayal, Materials Science Forum, 318-320 (1999), 495-502.
- [47] U. Kamachi Mudali and R.K. Dayal, J. Materials Science, 35 (2000), 1799-1803.
- [48] J. Stewart and D.E. Williams, Corrosion Science, 33 (1992), 457-474.
- [49] Kujanpaa, V.P., Suutala, N.J., Takala, T. and Moisio, T.J.I., Metal Construction,12 (1980) 282.
- [50] Veli Kujanpää, Thick-section laser and hybrid welding of austenitic stainless steels, 8th International Conference on Photonic Technologies LANE 2014 Physics, Procedia 56 (2014) 630 636.
- [51] Lippold, J. C.. Solidification behavior and cracking susceptibility of pulsed-laserwelds in austenitic stainless steels, Welding Journal, 73, 6 (1994) 129–139.
- [52] Kowaka, M. Metal corrosion damage and protection technology, (Chapter 6: Stress corrosion cracking of stainless steels), Allerton Press, (1990), 347-467.

- [53] Fang, Z., Wu, Y., Zhu, R., Cao, B. & Xiao, F.: Stress corrosion cracking of austenitic type 304 stainless steel in solutions of hydrochloric acid + sodium chloride at ambient temperature, Corrosion, 50,11, (1994),873 878.
- [54] Craig, B.D. & Lane, R.A.: Material failure part 1: Environmental assisted cracking, Amptiac, 9, 1, 9-16 & 17-25 (1988).
- [55] j. E. Truman, the influence of chloride content, ph and temperature of test solution on the occurrence of stress corrosion cracking with austenitic stainless steel, Corrosion Science,17, (1977),737 746.
- [56] Béla Leffler, STAINLESS stainless steels and their properties, http://www.outokumpu.com/files/group/hr/documents/stainless20.pdf.
- [57] K.V. Kasiviswanathan, N.G. Muralidharan, N. Raghu, R.K. Dayal and Hasan Shaikh, Corrosion related failures of austenitic stainless steel components, Corrosion of austenitic stainless steels, (2002) 314-339.
- [58] M.Vinoth Kumar, V.Balasubramanian, S.Rajakumar, ShajuK.Albert, Stress corrosion cracking behaviour of gas tungsten arc welded super austenitic stainless steel joints, Defense Technology, 11, 3, (2015), 282-291.
- [59] Raman Singh, Weld cracking in ferrous alloys, Wood head publishing limited, Cambridge, New Delhi,
- [60] A. M. El-Batahgy, Effect of Laser Welding Parameters on Fusion Zone Shape and Solidification Structure of Austenitic Stainless Steels, Materials Letters, 32,155-163.
- [61] K. Manonmani, N. Murugan, G. Buvanasekaran, Effects of process parameters on the bead geometry of laser beam butt welded stainless steel sheets, Int J Adv Manuf Technol (2007) 1125–1133.
- [62] C. Roepke and S. Liu, The effects of process, power level, heat input, and preheat on the macrostructure and microstructure of hybrid welds in HY-80 steel were investigated, supplement to the welding journal, august 2009.
- [63] Matsuda, TIG or MIG arc augmentented laser welding of thick mild steel plate. Joining and Materials 1 (1): (1988),38–41.
- [64] Steen, W. M., and Eboo, M.. Arc augmented laser welding. Metal Construction 11 (7): (1979),332–335.

- [65] Tadamalle, A.,P., Reddy, Y., P., Ramjee, E.Influence of laser welding process parameters on weld pool geometry and duty cycle, Advances in Production Engineering & Management 8 1, 52-58.
- [66] Girolamo Costanzaa, Andrea Silib, Maria Elisa Tataa, Weldability of austenitic stainless steel by metal arc welding with different shielding gas, Procedia strural integrty ,2 ,(2006) ,3508-3514.
- [67] Zhou, Kang & Cai, Lilong. (2014). On the development of nugget growth model for resistance spot welding. Journal of Applied Physics. 115. . 10.1063/1.4872247.
- [68] Nachimani Charde, Rajprasaad Rajkumar, Investigating spot weld growth on 304 austenitic stainless steel (2 Mm) sheets, Journal of Engineering Science and Technology, 8, 1, (2013) 69 76.
- [69] Shamsul Baharin Jamaludina, Mazlee Mohd Noor, Muhammad Rifki Ismail, Khairel Rafezi Ahmad, Kamarudin Hussin, Effect of Spot Welding Current and Cycles on the Mechanical Properties of Welded Galvanized Steel Sheets, Advanced Materials Research, 795 (2013), 87-90.
- [70] M. Somervuori, L.-S. Johansson, M. H. Heinonen, D. H. D. van Hoecke, N. Akdut, H. E. Hänninen, Characterisation and corrosion of spot welds of austenitic stainless steels, Materials and Corrosion, 55, 6, (2004).
- [71] Sourabh Babasaheb Shinde, Mr. S. R. Gavali, A study on residual stress of resistance spot weld, International Engineering Research Journal (IERJ), Special Issue, 85-87.
- [72] WenqianZhang, KeweiFang, YujinHu, SiyangWang, XuelinWang, Effect of machining-induced surface residual stress on initiation of stress corrosion cracking in 316 austenitic stainless steel, Corrosion Science, 108, (2016), 173-184.
- [73] S.G. Acharyya, A. Khandelwal, V. Kain, A. Kumar, I. Samajdar, Surface working of 304L stainless steel: Impact on microstructure, electrochemical behavior, and SCC resistance, Materials Characterization, 72, (2012), 68-76.
- [74] Shiva Gorjiana, Barat Ghobadiana, Solar Thermal Power Plants: Progress and Prospects in Iran, Energy Procedia, 75, (2015),533 539.

- [75] Nagarajan, Selvakumar & Barshilia, Harish & S. Rajam, K.. Review of sputter deposited mid- to high- temperature solar selective coatings for Flat Plate/Evacuated tube collectors and solar thermal power generation applications.,(2010).
- [75] Manuel J. Blanco, Lourdes Ramirez Santigosa, Advances in Concentrating Solar Thermal Research and Technology, Woodhead Publishing Series in Energy (2017).
- [76] Keith Lovegrove and Wes Stein, Concentrating solar power technology Principles, developments and applications, Woodhead Publishing Series in Energy: Number 21, (2012).
- [77] Soteris A. Kalogirou, Solar thermal collectors and applications, Progress in Energy and Combustion Science, 30, (2004), 231–295.
- [78] L.M. Ayompe, A. Duffy, S.J. McCormack, M. Conlon, Validated TRNSYS model for forced circulation solar water heating systems with flat plate and heat pipe evacuated tube collectors, Applied Thermal Engineering, 31, (2011), 1536-1542.
- [79] Farzad Jafarkazemi and Hossein Abdi, Evacuated tube solar heat pipe collector model and associated tests, Journal of Renewable and Sustainable Energy, 4, 2, (2012).
- [80] Sarada Kuravi, Jamie Trahan, D. Yogi Goswami, Muhammad M. Rahman, Elias K. Stefanakos, Thermal energy storage technologies and systems for concentrating solar power Plants, Progress in Energy and Combustion Science, 39,(2013),285-319.
- [81] Arun Kumar and S.K.Shukla, A Review on Thermal Energy Storage Unit for Solar Thermal Power Plant Application, Energy Procedia, 74, (2015),462 469.
- [82] I. Santos-Gonzáleza, M. Sandoval-Reyesa, O. García-Valladaresb, N. Ortegab, V.H. Gómez, Design and Evaluation of a Compound Parabolic Concentrator for Heat Generation of Thermal Processes, Energy Procedia, 57, (2014),2956 – 2965.
- [83] Erik Pihl, Duncan Kushnir, Björn Sandén, Filip Johnsson, Material constraints for concentrating solar thermal power, Energy, 44, (2012) ,944-954.
- [84] Stefano Passerini, Optical And Chemical Properties Of Molten Salt Mixtures For Use In High Temperature Power Systems, Master Of Science In Nuclear Science And Engineering At The Massachusetts Institute Of Technology.
- [85] Sequeira, C. A. C, High temperature corrosion in molten salts, Molten salt forum; v. 7, Switzerland, Trans Tech Publications LTD (2003).

- [86] Slusser, J. W., Titcomb, J. B., & Heffelfinger, M. T, Corrosion in molten nitrate-nitrite salts, Journal of metals, (1985) ,3724-27.
- [87] Fernández, A. A, Lasanta, M. M., & Pérez, F. F, Molten Salt Corrosion of Stainless Steels and Low-Cr Steel in CSP Plants, Oxidation Of Metals, 78 (5/6), (2012) 329-348.
- [88] Bradshaw, R. W. &Goods, S. H, Effect of Temperature on Corrosion of Type 316 SS by Molten NaNO3-KNO3.Retrived from: http://www.electrochem.org/dl/ma/197/pdfs/0209. Pdf.
- [89] Kruizenga, A., Stainless steels corrosion by molten nitrates: analysis and lessons learned. Sand 2011-6579. Sandia National Laboratories. Livermore, California, (2011)...
- [90] ASTM A 240/A 240M 04a, Standard Specification for Chromium and Chromium-Nickel Stainless Steel Plate, Sheet, and Strip for Pressure Vessels and for General Applications
- [91] L.E. Umoru, Effect of weld type and post weld heat treatment on the corrosion resistance of AISI 321 stainless steel in a tar sand digester, Emirates Journal for Engineering Research, 13,2, (2008),45-50
- [92] Tae-Hoon Nam, Eunsol An, Byung Jun Kim, Sunmi Shin, Won-Seok Ko, Nokeun Park, Namhyun Kang and Jong Bae Jeon, Effect of Post Weld Heat Treatment on the Microstructure and Mechanical Properties of a Submerged-Arc-Welded 304 Stainless Steel, Metals, (2018), 8, 26
- [93] ASTM A262-02a. Standard practices for detecting susceptibility to intergranular attack in austenitic stainless steels, (2002).
- [94] G.F.V. Voort, Metallography principles and practice, ASM International, United States of America, (2007).
- [95] Paul S. Prevéy, Lambda Research, Inc., X-ray diffraction residual stress techniques.
- [96] J.S. Corte, J.M.A. Rebello, M.C.L. Areiza, S.S.M. Tavares, M.D. Araujo, Failure analysis of AISI 321 tubes of heat exchanger, Engineering Failure Analysis ,6, (2015), 170-176.
- [97] H.M. Shalaby, Failure investigation of 321 stainless steel pipe to flange weld joint, Engineering Failure Analysis, 80, (2017), 290-298.
- [98] H.M. Shalaby, K. Ravindranath, N. Tanoli, B. Al-Wakaa, Failure of 321 stainless steel heater tube in heavy crude oil, Case Studies in Engineering Failure Analysis, 9,(2017), 1-8.
- [99] Y.Y. Chen, H.C. Shih, Y.M. Liou, L.H. Wang, and J.C. Oung, Y. Y. Chen, H. C. Shih, Y. M. Liou, L. H. Wang, J. C. Oung, Stress corrosion cracking of type 321 stainless steels under

- simulated petrochemical conditions containing thiosulfate and chloride, CORROSION,62,9, (2006),781-794.
- [100] R Parrott and H Pitts, Chloride stress corrosion cracking in austenitic stainless steel Assessing susceptibility and structural integrity, RR902Research Report, HSE Books, First published (2011),
- [101] Raffi Mohammed1, Srinivasa Rao, Madhusudhan Reddy G, Effect of Microstructure on Stress Corrosion Cracking Behaviour of High Nitrogen Stainless Steel Gas Tungsten Arc Welds, IOP Conf. Series: Materials Science and Engineering 330 (2018). ICRAMMCE 2017.
- [102] Weiwei Wu, Yanjun Guo, Haifeng Yu, Yiming Jiang, Jin Li, The Quantitative Effect of Mo and Cu on the Stress Corrosion Cracking and Pitting Corrosion Behavior of Ultra-Pure Ferritic Stainless Steels, International Journal of Electrochemical Science, 10 (2015) 10689 10702.
- [103] C.-C. Hsieh, W. Wu, Overview of Intermetallic Sigma (σ) Phase Precipitation in Stainless Steels, ISRN Metallurgy ,20,12 (2012) 1-16.
- [104] D.M.E. Villanueva, F.C.P. Junior, R.L. Plaut, A.F. Padilha, Comparative study on sigma phase precipitation of three types of stainless steels: austenitic, superferritic and duplex, Materials Science and Technology 22,9, (2013) 1098-1104.
- [105] T. Shoji, Z. Lu, Q. Peng, Factors affecting stress corrosion cracking (SCC) and fundamental mechanistic understanding of stainless steels, (2011) 245-272.
- [106] https://www.watersindustrial.com/ToolGuide-TubePolishingStainless.
- [107] http://www.jotunpolishing.com/